Anatomical Patterns, Kinematics, and Propulsive Strategies of Foot-Based Swimming Birds

Citation

Clifton, Glenna Talbot. 2017. Anatomical Patterns, Kinematics, and Propulsive Strategies of Foot-Based Swimming Birds. Doctoral dissertation, Harvard University, Graduate School of Arts & Sciences.

Permanent link

http://nrs.harvard.edu/urn-3:HUL.InstRepos:41142032

Terms of Use

Share Your Story

Anatomical patterns, kinematics, and propulsive strategies of foot-based swimming birds

Anatomical patterns, kinematics, and propulsive strategies of foot-based swimming birds

Abstract

Within the diversity of birds, numerous lineages have colonized aquatic environments. Birds that swim by paddling with their feet must generate propulsive forces underwater using legs originally adapted for walking. Despite this challenge, foot-propelled swimming has evolved independently in at least six avian lineages (including in cormorants, grebes, and loons) and to varying degrees of specialization. Understanding the extent of convergence among these groups reveals the functional demands of producing force underwater and the selective pressures that have shaped avian evolution. My dissertation focuses on examining anatomical, movement, and propulsive patterns underlying foot-based swimming in birds. In four chapters, I use comparative dissections, high-speed videography, and a new robotic technique to explore how paddling birds convergently adapt to a swimming lifestyle.

In the first chapter, I combine new qualitative dissection data with a review of historical studies on avian hindlimb myology to identify patterns in hindlimb muscle anatomy associated with swimming. I performed dissections of 36 hindlimb muscles in 35 specimens representing 8 bird species with varying degrees of swimming specialization. My findings show that birds specialized for diving streamline the body by integrating the proximal hindlimb into the skin covering the abdomen, allowing the attachments of several hindlimb muscles to shift distally along the leg. Diving birds also possess relatively enlarged ankle plantarflexors with loons demonstrating an extreme condition. Despite a similar lifestyle to loons, grebes reduce many distal limb muscles and instead possess long, calcified tendons.

To investigate a potential explanation for the anatomical divergence between grebes and loons observed in chapter one, I examine foot motion and force production during an impressive grebe mating behavior (Ch. 2)

and during underwater swimming by common loons (Ch. 3, 4).

Chapter two focuses on grebe "rushing," where breeding pairs run on water powered only by their legs. I spent a month filming wild rushing grebes in S. Oregon using high-speed cameras. My findings show that rushing grebes take up to 20 steps per second and their feet slap the water at 4 m/s. I reproduced water slaps in the lab using physical models of grebe feet, demonstrating that the slap alone contributes up to 30-55% of the required weight support and exerts forces approaching those associated with tendon calcification in birds.

In chapter three, I designed custom underwater camera cases to film wild loons in a rehabilitation pool. Loons are notoriously reclusive, precluding any previous, quantitative analysis of swimming. My high-speed footage shows that loons swim in a similar manner to grebes, synchronously paddling their feet lateral to the body and incorporating long-axis rotation at the knee. Loons use head-bobbing to increase visual acuity underwater and elicit tight but slow turns. To control turning, loons increase the speed of the outside foot, begin the power stroke of the outside foot before that of the inside foot, and bank the body away from the turn.

For my last, fourth, chapter, I design a novel bio-robotic approach to measure the fluid forces produced by wild swimming animals. I attached cadaveric loon feet to an industrial robot programmed to exactly replicate the swimming motions of a loon's foot (based on data from Ch. 3). A force sensor attached to the robot measured swimming forces throughout the propulsive stroke. This robotic approach provides the most accurate exploration to date of how foot-propelled birds produce hydrodynamic forces. I find that swimming loons power swimming by generating more lift than drag, challenging traditional paradigms of aquatic locomotion.

Contents

Listing of figures

Listing of tables

Acknowledgments

The path to my Ph.D. defense would not have been possible without the support and help of numerous people. These interactions have not only improved my research, but also helped shape me as a scientist, teacher, colleague, and friend.

First and foremost I would like to thank my advisor, Andrew Biewener, for his unparalleled support. I am grateful for Andy's encouragement through tough times and perceptive criticism that pushed our research to be more thorough, persuasive, and interesting. I admire Andy's sharp intellect and caring leadership, and am thankful for the years I was able to learn from his example.

My thesis committee has provided critical support and feedback throughout my Ph.D. research. I would like to thank George Lauder, John Hutchinson, Stephanie Pierce, Stacey Combes, and Scott Edwards for their insightful comments and encouragement.

The Biewener Lab has been a source of stimulating conversations, comfort, and fun. Allison Arnold-Rife, Maria de Boef Miara, Jennifer Carr, C. David Williams, Natalie Holt, Robert Kambic, and Nicolai Konow have patiently guided me through learning high-speed videography, 3D printing, electronics, inverse dynamics, dissection techniques, and many other skills central to my Ph.D. research. Carolyn Eng, Talia Moore, Kari Taylor-Burt, Brianna McHorse, and Phil Lai have been excellent graduate student partners-in-crime. I thank them for providing practical suggestions, lending many helping hands, and almost always agreeing to accompany me on trips to get ice cream. I would also like to thank Andrew Mountcastle, Nick Gravish, Shridar Ravi, James Crall, Callin Switzer, Jacob Peters, and Mary Salcedo for constant support and for reminding me that biomechanics is not always about vertebrates.

I am especially grateful to the staff members at the Concord Field Station who have routinely gone above and beyond to assist me, who create a warm and caring environment, and who always find the funniest white ele-

1

Introduction

1.1 Evolution of foot-propelled swimming in birds

Every animal must, at some point, move through its environment to find food, meet potential mates, or evade predators. Yet, different environments pose distinct movement challenges. Similar movement strategies for a given environment have evolved repeatedly but independently, illustrating convergent evolution. By understanding how disparate animals have convergently evolved traits to cope with the challenges of navigating in a similar ecological niche, we can appreciate the physical demands of an environment and the evolutionary pressures that have shaped the diversity of life.

Birds are unique in that most species possess multiple modes of locomotion, including some that can run, fly,

and swim. Despite this locomotive diversity, numerous taxa have evolved specializations for moving through a specific medium. Birds that swim must overcome ancestral adaptations for flight and contend with the constraints of an aquatic lifestyle.

From a broad perspective, birds have evolved two separate mechanisms for producing propulsive forces underwater. Some birds–such as penguins, auks, and dippers–use their wings to swim and therefore face tradeoffs with flight. Others rely on their feet for swimming–such as loons, grebes, cormorants, and ducks–and face tradeoffs with walking on land. These foot-based birds are especially helpful for understanding the physical challenges of swimming since foot-propulsion has evolved convergently numerous times and since extant species retain many levels of swimming specialization.

Numerous lineages of birds have evolved the ability to swim using their feet, with five groups independently reaching a high level of specialization and performance. Among extant birds, foot-propelled swimming can be found in Anseriformes (dabbling, diving and sea- ducks), Gruiformes (coots and moorhens), Podicipedidae (grebes), and seabirds (including loons, penguins, auks, cormorants, and pelicans) (Johnsgard, 1987; Prum et al., 2015; Figure 1.1). One extinct lineage from the Cretaceous, Hesperornithes, is also considered a foot-propelled swimmer (Hinić-Frlog and Motani, 2010; Zinoviev, 2011). Many of these foot-propelled birds paddle at the surface and retain the ability to walk on land. Yet, a few lineages have evolved a more specialized aquatic lifestyle that requires diving underwater to capture fish, including diving and seaducks (Aythyinae and Merginae), cormorants (Phalacrocoracidae), grebes (Podicipedidae), loons (Gaviidae), and, most likely, Hesperornithes (Hinić-Frlog and Motani, 2010; Zinoviev,
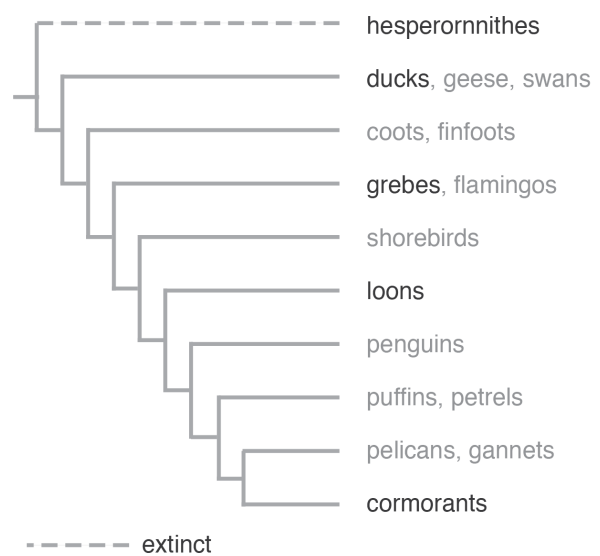
Figure 1.1: Phylogeny of foot-propelled swimming birds. Based on Prum et al., 2015, darker type represents a lineage including specialized divers. Dashed line depicts an extinct lineage.

2011). Most species within specialized foot-propelled birds struggle to stand or walk on land and some have even lost the ability to fly.

1.2 Adaptations for swimming

Living in an aquatic environment poses many challenges for birds. Birds evolved from land-dwelling dinosaurs (Xu et al., 2011), retaining or developing several features beneficial for flight and living on the ground. Yet, many of these features are not well suited for a life in the water. To contend with the demands of a swimming lifestyle, independent groups of foot-propelled swimming birds evolved a suite of anatomical and physiological adaptations.

Body shape: Whether walking, flying, or swimming, birds move through a fluid. Yet, water has a density approximately 800 times higher and a viscosity 50 times greater than air. The increased density of water exerts substantial drag forces on the body to resist forward motion, even at slow speeds (Vogel, 1983). Swimming while partially submerged at the water surface presents a further complication. As the body moves at the surface it generates surface, or "hull," waves that oppose forward motion. Both body drag and hull wave strength increase exponentially with speed and depend on body shape and size (Bush and Hu, 2006; Prange and Schmidt-Nielsen, 1970). Body shapes that may benefit flight or walking generate high drag forces in water. To streamline the body (Figure 1.2), specialized swimming birds have a narrow pelvis and shift the feet caudally by having a short femur and long tibiotarsus (Doube et al., 2012; Hinić-Frlog and Motani, 2010; Zeffer et al., 2003). However, these anatomical adaptations also result in terrestrial instability, representing a functional tradeoff between walking and swimming.

Buoyancy: Foot-propelled birds that dive underwater must also contend with a buoyant force that pushes the body towards the surface. This buoyancy and the counteracting gravity force are determined by body volume and density. Most birds possess hollow postcranial bones (O'Connor, 2009) and a multi-chambered air sac respiratory system (Sereno et al., 2008), which decrease body weight and maximize metabolic capacity to enable flight.

However, these features also increase buoyancy and oppose underwater diving. To reduce buoyancy many specialized swimming birds have dense bones with limited or no hollowness, called pachyostosis (Chinsamy et al., 1998; Gutzwiller et al., 2013; Ksepka et al., 2015). Additionally, cormorant feathers possess a special barbule structure that permits water absorption, reducing air retention to increase body density (Grémillet et al., 2005).

Respiration: Diving birds are unable to extract oxygen from water and so must return to the surface to breathe. But, large inhalations of air increase underwater buoyancy, and therefore exertion. The measured dive durations for some birds exceed their aerobic dive limit, or how long they can power swimming through oxygen-dependent metabolism (Halsey and Butler, 2006). To avoid hypoxia in critical tissues while diving, birds restrict blood flow to less important tissues (vasoconstriction) and reduce their heart

Mallard - dabbling duck

Double-crested cormorant

Western grebe

Common loon

25 cm   4 cm

Figure 1.2: Body and foot shape in foot-propelled swimming birds. Traced outlines of birds swimming underwater show body streamlining in specialized diving birds. Traced outlines of feet shown to scale courtesy of I. Marques. Video of mallard underwater swimming used for body outline courtesy of K. Taylor-Burt.

rate (bradycardia) (Butler, 2001; Butler, 2004). These physiological strategies extend how long diving birds can remain underwater.

Vision: Most foot-propelled diving birds hunt for fish guided by vision. Yet, the differing light and refractory conditions in water versus air place conflicting demands on the eyes. Water absorbs and scatters light, reducing brightness with depth. To preserve vision in the darkness, some diving birds possess large pupils (Levy and Sivak,

4

1980, Martin 2012). However, large pupil size reduces the in-focus depth of view in air, representing a tradeoff for diving birds. Additionally, light refraction in water bends light and requires adjustment of lens shape in order to maintain visual acuity. Although cormorants were previously thought to achieve high levels of visual acuity and binocular vision underwater (Katzir and Howland, 2003; Sivak et al., 1977; Strod et al., 2004), recent studies suggest that the visual capacity of cormorants does not exceed that of terrestrial close-range predators (Martin et al., 2008). However, visual adaptations in other foot-propelled diving birds have not been investigated and may present new findings.

1.3 STRATEGIES FOR GENERATING SWIMMING FORCES

The body of foot-propelled swimming birds has been convergently sculpted throughout evolution to adjust to an aquatic lifestyle. However, the most drastic adaptations derive from the demands on the hindlimb to generate propulsive forces.

Generating propulsive forces underwater is fundamentally different than on solid land. In fluids, molecule energy overpowers attractive forces allowing for the molecules to flow past each other and for the fluid to change shape. The force generated by pushing against a fluid results from displacing its molecules, thus fluid forces depend on the size, shape, orientation, and speed of the exerting object (Vogel, 1983). Therefore, as birds evolved from using their feet for walking to swimming, they faced new anatomical and movement constraints. An efficient foot-based swimmer should have relatively large feet in shapes that effectively produce propulsive forces. The speed and motion of paddling may differ from walking in order to generate forward thrust. Yet adaptations to improve swimming efficiency, such as a large foot size, may impede walking on solid ground, resulting in a functional tradeoff for the hindlimb.

Darwin asked in The Origin of Species, "What can be plainer than that the webbed feet of ducks and geese are formed for swimming?" As Darwin correctly identified, most foot-propelled swimming birds possess webbing between the toes to increase the surface area of the foot. Yet, within this generality, foot shape demonstrates

remarkable diversity. All Anseriformes and most seabirds (including loons) have three webbed digits, with a reduced, posterior hallux (Figure 1.2; Wilcox, 1952). Cormorants, pelicans, frigatebirds, and gannets are totipalmate with all four digits webbed (Johnsgard, 1987). Grebes and rails have lobate feet, where digits II-IV are lobed. It has been suggested that the asymmetrical lobes of grebe feet act as individual hydrofoils to produce lift (Johansson and Norberg, 2000).

However, underwater force production depends on both foot shape and motion. Swimming kinematics has been observed in several groups of foot-propelled birds but does not demonstrate a consistent convergent pattern. Dabbling ducks swim at the surface by paddling the feet underneath the body (Carr, 2008; Provini et al., 2012). Diving ducks, on the other foot, demonstrate a more lateral position of the hindlimbs (Ribak and Swallow, 2010). Cormorants paddle their feet underneath the body, but because the body simultaneously moves forward the feet do not move backward relative to still water (Ribak et al., 2004). With this motion, the triangular shape of cormorant feet has been proposed to function like a delta-wing to produce lift forces (Johansson and Norberg, 2003). Grebes paddle the feet lateral to the body in a caudal and dorsal arc that also does not travel backward relative to still water (Johansson and Norberg, 2001). Even with only a subset of foot-propelled swimming birds studied, there is no consistent kinematic strategy for swimming using the feet.

1.4 Summary

Foot-propelled swimming has independently evolved numerous times and to varying levels of specialization within birds. To contend with the challenges of an aquatic lifestyle, these foot-based birds have evolved a streamlined body shape with diving birds also possessing adaptations to increase body density, to control circulation and increase aerobic capacity, and to maintain vision underwater. Some groups demonstrate extreme morphological convergence. The extent of this convergence has even prompted a long-standing debate regarding the monophyly of grebes and loons (and sometimes Hesperornithes). Supporters focus on morphological data (Cracraft, 1982; Livezey, 2010; Livezey and Zusi, 2007; Mayr and Clark, 2003; Van Tuinen et al., 2001), with only recent

molecular data providing persuasive evidence of independence (Hackett et al., 2008; Prum et al., 2015; Sibley and Ahlquist, 1991; Storer, 1971). Although these groups represent independent lineages of foot-propelled swimming, what is the extent of functional convergence?

Variation in foot shape and swimming kinematics among foot-propelled swimming birds complicates the notion of convergence within these lineages. To understand the degree and implications of convergence requires direct comparisons across many groups of swimming birds. This thesis aims to explore aspects of convergence within foot-propelled swimming birds by examining hindlimb muscle anatomy, movement kinematics, and force production mechanisms in several lineages. In Chapter 1, I perform detailed dissections of the hindlimb muscles in seven groups of foot-based swimming birds varying in swimming specialization. Chapter 2 augments previous work on grebe swimming by analyzing a second extreme requirement of grebe hindlimbs, their use while running on water during a mating display called rushing. In Chapter 3, I provide the first kinematic analysis of swimming and maneuvering in loons. Lastly, Chapter 4 uses a new method of robotically replicating the foot motions of freely-swimming animals to definitively determine force production during loon swimming, representing the first direct measurement of foot-based swimming forces in birds. The findings of this work have implications for understanding the selective pressures underlying avian evolution and could inspire biomimetic designs.

1.5   REFERENCES

Bush, J. W. M. and Hu, D. L. (2006). WALKING ON WATER: Biolocomotion at the Interface. Annu. Rev. Fluid Mech. 38, 339-369.

Butler, P. J. (2001). Diving beyond the limits. News Physiol. Sci. 16, 222-7.

Butler, P. J. (2004). Metabolic regulation in diving birds and mammals. Respir. Physiol. Neurobiol. 141, 297-315.

Carr, J. A. (2008). Muscle function during swimming and running in aquatic, semi-aquatic and cursorial birds.

Chinsamy, A., Martin, L. D. and Dobson, P. (1998). Bone microstructure of the diving Hesperornis and the voltant Ichthyornis from the Niobrara Chalk of western Kansas. Cretac. Res. 19, 225-235.

Cracraft, J. (1982). Phylogenetic Relationships and Monophyly of Loons, Grebes, and Hesperornithiform birds, with comments on the early history of birds. Syst. Biol. 31, 35-56.

Doube, M., Yen, S. C. W., K?osowski, M. M., Farke, A. A., Hutchinson, J. R. and Shefelbine, S. J. (2012). Whole-bone scaling of the avian pelvic limb. J. Anat. 221, 21-29.

Grᴑmillet, D., Chauvin, C., Wilson, R. P., Le Maho, Y. and Wanless, S. (2005). Unusual feather structure allows partial plumage wettability in diving great cormorants Phalacrocorax carbo. J. Avian Biol. 36, 57-63.

Gutzwiller, S. C., Su, A. and Oᴑorn, P. M. (2013). Postcranial pneumaticity and bone structure in two clades of neognath birds. Anat. Rec. 296, 867-876.

Hackett, S. J., Kimball, R. T., Reddy, S., Bowie, R. C. K., Braun, E. L., Braun, M. J., Chojnowski, J. L., Cox, W. A., Han, K.-L., Harshman, J., et al. (2008). A phylogenomic study of birds reveals their evolutionary history. Science 320, 1763-8.

Halsey, L. G. and Butler, P. J. (2006). Optimal diving behaviour and respiratory gas exchange in birds. Respir. Physiol. Neurobiol. 154, 268-83.

Hinić-Frlog, S. and Motani, R. (2010). Relationship between osteology and aquatic locomotion in birds: determining modes of locomotion in extinct Ornithurae. J. Evol. Biol. 23, 372-85.

Johansson, L. C. and Norberg, U. M. (2000). Asymmetric toes aid underwater swimming. Nature 407, 582-3.

Johansson, L. and Norberg, U. M. (2001). Lift-based paddling in diving grebe. J. Exp. Biol. 204, 1687-96.

Johansson, L. and Norberg, R. (2003). Delta-wing function of webbed feet gives hydrodynamic lift for swimming propulsion in birds. Nature 424, 65-68.

Johnsgard, P. A. (1987). Diving Birds of North America. Lincoln, Nebraska: University of Nebraska Press.

Katzir, G. and Howland, H. C. (2003). Corneal power and underwater accommodation in great cormorants (Phalacrocorax carbo sinensis). J. Exp. Biol. 206, 833-41.

Ksepka, D. T., Werning, S., Sclafani, M. and Boles, Z. M. (2015). Bone histology in extant and fossil penguins (Aves: Sphenisciformes). J. Anat. 227, 611-630.

Livezey, B. C. (2010). Grebes and flamingos: standards of evidence, adjudication of disputes, and societal politics in avian systematics. Cladistics 27, 391-401.

Livezey, B. C. and Zusi, R. L. (2007). Higher-order phylogeny of modern birds (Theropoda, Aves: Neornithes) based on comparative anatomy. II. Analysis and discussion. Zool. J. Linn. Soc. 149, 1-95.

Martin, G. R., White, C. R. and Butler, P. J. (2008). Vision and the foraging technique of Great Cormorants Phalacrocorax carbo: Pursuit or close-quarter foraging? Ibis (Lond. 1859). 150, 485-494.

Mayr, G. and Clark, J. (2003). The deep divergences of neornithine birds: a phylogenetic analysis of morphological characters. Cladistics 19, 527-553.

Prange, H. D. and Schmidt-Nielsen, K. (1970). The metabolic cost of swimming in ducks. J. Exp. Biol. 53, 763-77.

Provini, P., Goupil, P., Hugel, V. and Abourachid, A. (2012). Walking, Paddling, Waddling: 3D Kinematics Anatidae Locomotion (Callonetta leucophrys). J. Exp. Zool. 317, 275-282.

Prum, R. O., Berv, J. S., Dornburg, A., Field, D. J., Townsend, J. P., Lemmon, E. M. and Lemmon, A. R. (2015). A comprehensive phylogeny of birds (Aves) using targeted next-generation DNA sequencing. Nature 526, 569-573.

Ribak, G. and Swallow, J. (2010). Drag-based "hovering" in ducks: the hydrodynamics and energetic cost of bottom feeding. PLoS One 5, 1-11.

Ribak, G., Weihs, D. and Arad, Z. (2004). How do cormorants counter buoyancy during submerged swimming? J. Exp. Biol. 207, 2101-2114.

Sibley, C. G. and Ahlquist, J. E. (1991). Phylogeny and Classification of Birds: A Study in Molecular Evolution. New Haven, CT: Yale University Press.

Sivak, J. G., Lincer, J. L. and Bobier, W. (1977). Amphibious visual optics of the eyes of the double-crested cormorant (Phalacrocorax auritus) and the brown pelican (Pelecanus occidentalis). Can. J. Zool. 55, 782-788.

Storer, R. W. (1971). Classification of Birds. In Avian Biology (ed. Farner, D. S.), King, J. R.), and Parkes, K. C.), pp. 1-20. New York, NY: Academic Press, Inc.

Strod, T., Arad, Z., Izhaki, I. and Katzir, G. (2004). Cormorants keep their power: visual resolution in a pursuit-diving bird under amphibious and turbid conditions. Curr. Biol. 14, R376-R377.

Van Tuinen, M., Butvill, D. B., Kirsch, J. a and Hedges, S. B. (2001). Convergence and divergence in the evolution of aquatic birds. Proc. Biol. Sci. 268, 1345-50.

Vogel, S. (1983). Life in moving fluids?: the physical biology of flow. Princeton University Press.

Wilcox, H. H. (1952). The Pelvic Musculature of the loon, gavia immer. Am. Midl. Nat. 48, 513-573.

Zeffer, A., Johansson, L. C. and Marmebro, Å. (2003). Functional correlation between habitat use and leg morphology in birds (Aves). Biol. J. Linn. Soc. 79, 461-484.

Zinoviev, A. V. (2011). Notes on the hindlimb myology and syndesmology of the Mesozoic toothed bird Hesperornis regalis (Aves: Hesperornithiformes). J. Syst. Palaeontol. 9, 65-84.

2

Comparative hindlimb myology of foot-propelled swimming birds

COAUTHORS: JENNIFER A. CARR, ANDREW A. BIEWENER

2.1   ABSTRACT

Several groups of birds have convergently evolved the ability to swim using their feet despite facing tradeoffs with walking. However, swimming relative to terrestrial performance varies across these groups. Highly specialized divers, such as loons and grebes, excel at swimming underwater but struggle to stand on land while species that

primarily swim at the water surface, such as mallards, retain the ability to move terrestrially. The identification of skeletal features associated with a swimming style and conserved across independent groups suggests that the hindlimb of foot-propelled swimming birds has adapted to suit the physical challenges of producing propulsive forces underwater. How do hindlimb muscles reflect swimming ability and mode? This paper presents the first comparative myology analysis of patterns associated with foot-based swimming. Our detailed dissections of 35 specimens representing eight species reveal anatomical trends in four independent lineages of extant swimming birds. We expand upon our dissections by compiling data from historical texts and provide a key to any outdated muscle nomenclature used in these sources. Our results show that specialized diving birds integrate the femur and proximal tibiotarsus into the skin covering the abdomen to streamline the body. Several hindlimb muscles exhibit dramatic anatomical variation. In diving birds, the *flexor cruris lateralis* (FCL) and *iliofibularis* (IF) reduce in size and shift distally along the tibiotarsus. The *femorotibialis medius* (FTM) extends along an expanded cnemial crest. The resulting increased moment arms of these muscles likely help stabilize the hip and knee while paddling. Additionally, distal ankle plantarflexors, including the *gastrocnemius* and digital flexors, are exceptionally large in diving birds in order to power foot propulsion. These patterns exist within distantly related lineages of specialized divers and, to a lesser extent, in surface swimmers. Together, our findings verify conserved muscular adaptations to a foot-propelled swimming lifestyle. The association of muscle anatomy with skeletal features and biomechanical movement demands can inform functional interpretation of fossil birds and reveal selective pressures underlying avian diversification.

2.2   INTRODUCTION

Although birds are often known for their flying abilities, several species are excellent swimmers. Swimming birds that paddle with their feet face trade-offs between moving on land and in the water. Despite this challenge, foot-propelled swimming has evolved convergently in birds, arising independently within distantly related lineages. As a result of transitioning to a life in the water, these birds possess a suite of physiological and anatomical character-

istics suitable for an aquatic environment. Previous research has focused on characterizing skeletal (Zeffer et al., 2003; Hinić-Frlog and Motani, 2010) and organ-level (Butler, 2004; Strod et al., 2004) adaptations for swimming; however, corresponding differences in muscle anatomy have never been studied. Comparing hindlimb myology across convergent lineages of foot-propelled swimming birds provides a unique opportunity to investigate how hindlimb muscles have adapted over evolutionary time to suit the physical demands of foot-propelled swimming.

The ability of birds to swim using their feet has evolved convergently in at least six avian lineages, but to varying degrees of specialization (Figure 2.1A). (1) The family Anatidae is one of the earliest diverging groups of extant birds and includes ducks, geese, and swans. All Anatidae species can swim. Most species are restricted to swimming at the surface, but some, particularly the diving ducks and seaducks, dive to considerable depths (up to 60 m for long-tailed ducks, *Clangula hyemalis*) (Schorger, 1947). (2) The rails (Rallidae) and finfoots (Heliornithidae) include several wetland species, including coots (*Fulica*) and moorhens (*Gallinule*), capable of swimming at the surface for short distances. (3-5) Three independent lineages of birds are excellent divers that survive by primarily hunting fish underwater, grebes (Podicipedidae), loons (Gaviidae) and cormorants (Phalacrocoracidae). The convergent specialization of these birds results in reduced mobility on land and even flightlessness in some species. (6) An extinct lineage of birds from the Cretaceous period, Hesperornithes, closely resembled grebes and loons suggesting a similar lifestyle and swimming ability (Zinoviev, 2011; Hinić-Frlog and Motani, 2010). Other seabirds□including gulls, terns, auks, penguins, gannets, and some petrels□also occasionally swim using their feet. However, these groups are closely related to cormorants and loons, and are unlikely to represent an independent evolution of foot-propelled swimming (Prum et al., 2015). Pelicans, however, are most-closely related to non-swimming shoebills and herons, indicating a potential seventh independent lineage.

The hundreds of species represented in these lineages of foot-propelled swimming birds can generally be separated into three functional groups. Surface swimming birds□such as dabbling ducks and coots□primarily stay at the water surface, escape threatening situations through flight, and are relatively capable of walking on land (Abourachid, 2001). Highly specialized diving birds□such as grebes and loons□excel at swimming underwater,
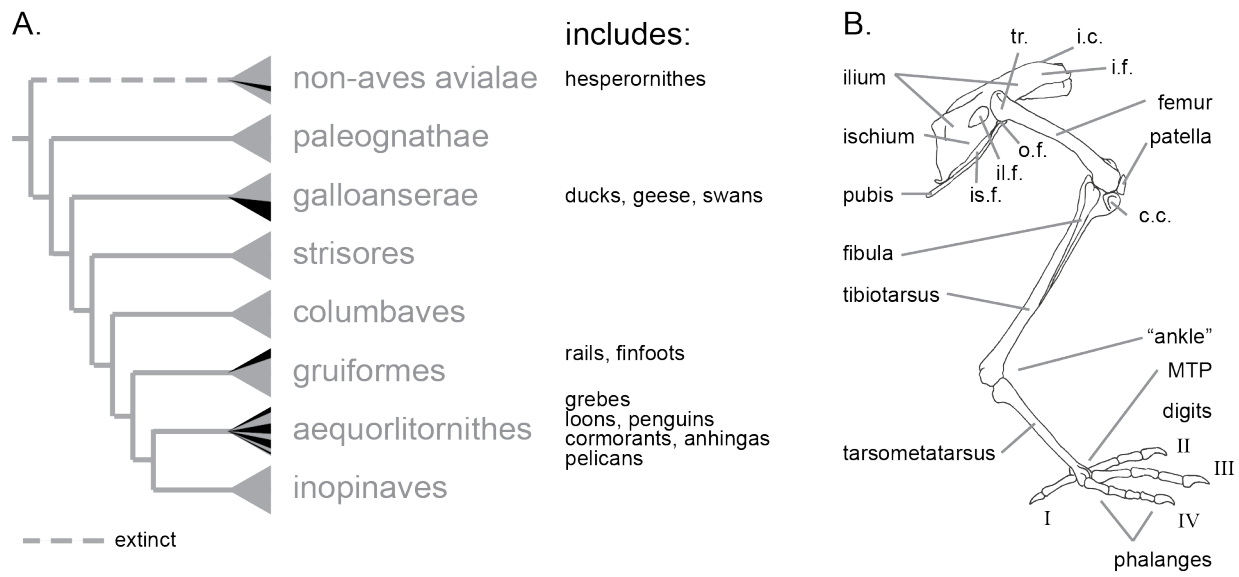
Figure 2.1: Evolution of foot-based swimming in birds and general avian skeletal anatomy. (A) Foot-based swimming has evolved at least six times within birds as denoted by black radiations within major gray bird lineages. The phylogeny is based on Prum et al., 2015. Branch lengths are not to scale. Dashed lines represent completely extinct groups. Common names of representative swimming birds from each lineage are listed to the right of the phylogeny. (B) General skeletal anatomy of birds annotated using the helmeted guineafowl (MCZ 341648). Abbreviations: trochanter (tr.), iliac crest (i.c.), iliac fossa (i.f.), obturator foramen (o.f.), ilioischiatic fenestra (il.f.), ischiopubic fenestra (is.f.), cnemial crest (c.c.), metatarsophalangeal joint (MTP).

dive to escape threats, and struggle to stand or walk on land (Johnsgard, 1987). Less specialized divers—such as seaducks and some cormorants—resemble highly specialized divers in their ability to swim underwater and their tendency to escape by diving, but retain some ability to walk on land (White et al., 2008; Abourachid, 2001).

All foot-propelled swimming birds must produce fluid forces using their feet originally adapted for walking on land. Generating force underwater is fundamentally different than on solid land. For a bird walking on land, the force its foot can exert against the ground to propel its body forward is only limited by the limb's musculoskeletal capacity to produce and withstand force. However, for a swimming bird, the force exerted against the water also depends on the size and shape of the foot, the orientation of the foot relative to its motion, and how quickly the foot is paddled (Vogel, 2008). To maximize fluid force production, and therefore swimming speed and maneuverability, an ideal swimmer would maximize the size of its feet and how quickly it pushes them through the water (Fish, 1993). Yet, large feet can make walking cumbersome and muscles optimized for speed may sacrifice force production. The need to produce fluid forces therefore places conflicting demands on the hindlimb of foot-

propelled swimming birds.

To contend with the challenges of producing forces underwater, all foot-propelled swimming birds have evolved specialized hindlimb features. Each species has an enlarged foot surface area due to webbing (three digits in Anatidae, loons, and seabirds or four digits in cormorants) or keratinous lobes around the toes (in grebes, rails, and finfoots) (Johnsgard, 1987). Foot-propelled swimming birds also have a thinner pelvis, shorter tarsometatarsus, a relatively short femur, and an enlarged cnemial crest (Zeffer et al., 2003; Hinić-Frlog and Motani, 2010; Doube et al., 2012). All of these features are exaggerated in highly specialized diving birds, which have especially large feet (Raikow, 1973), thin pelvises (Johnsgard, 1987), and enlarged knees through an expanded tibiotarsal cnemial crest in loons (Shufeldt, 1904), patella in cormorants (Owre, 1967; Shufeldt, 1913), or both in grebes (Beddard, 1896). These anatomical patterns exist across all independent lineages of foot-propelled swimming birds, suggesting that these features provide a selective benefit for swimming efficacy.

Most known avian hindlimb adaptations for swimming involve the skeleton due to the relative ease of preserving and analyzing bones. Yet while the hindlimb skeleton helps support forces transmitted to the limbs, muscles more directly reflect the capacity to produce forces that control and determine limb motion. Muscle is an extremely plastic tissue (Wisdom et al., 2015). This plasticity allows muscle to accommodate for use throughout an animal's lifetime as well as adapt over evolutionary time. Muscle size and architectural structure determine a muscle's capacity to produce force and change length. Where a muscle attaches to a bone defines the distance between its line of action and a joint, its moment arm. Longer moment arms produce stronger torques around the joint but result in small rotations relative to muscle length change (McMahon, 1984). Across generations, selection acts on muscle anatomy to accommodate movement demands with muscles changing in number (from fusion, loss, or novel muscles arising), size, architecture, and attachment location. Over long time scales, these changes result in macroevolutionary patterns where muscle anatomy represents an adaptation to an animal's lifestyle. As such, comparative muscle anatomy has the potential to reveal functional trends associated with a way of moving.

Although avian myology has been long studied, prior work has not provided comparative analysis of trends

associated with foot-propelled swimming. Most accounts survey anatomy across many species using one or two specimens per species and remark generally on foot-propelled swimming birds (George and Berger, 1966; Baumel and Witmer, 1993; Hudson, 1937; Bennett, 1996; Gadow and Selenka, 1891; Forbes, 1885; Garrod, 1875, 1874, 1873; Hudson et al., 1959; Raikow, 1987; Vanden Berge and Zweers, 1993). A few studies comprehensively address the myology of a single species of paddling bird using a small sample size (Owre, 1967; Shufeldt, 1904; Beddard, 1896; Garrod and Darwin, 1872; Haughton, 1865; Shufeldt, 1890; Wilcox, 1952; Rosser et al., 1982). But, stylistic and naming variations among these texts have made comparisons challenging. Here we compile data from these sources while accounting for multiple source languages, discrepancies in muscle naming, and the use of outdated species names. We also provide comparative data for species never before studied and for previously studied species to test past findings based on anatomical analysis of more specimens.

In this study we seek to identify functional trends in bird hindlimb anatomy relating to swimming performance. To address this aim, we directly compare hindlimb myology in species with varying levels of foot-propelled swimming specialization that represent convergently evolved lineages. We present data from detailed dissections of all extrinsic hindlimb muscles for 35 specimens representing seven species of foot-propelled swimming birds and one, non-swimming outgroup. We provide a convenient resource of accepted muscle names with common alternative names used in other works. Our scaled drawings, descriptions and discussion of the origins and insertions of the hindlimb muscles allow us, for the first time, to compare limb anatomy in the light of the functional demands of foot-based swimming. Our findings provide insight into convergent evolution within a subset of swimming birds. Additionally, our work presents a framework for future research to compare anatomical trends associated with swimming in other birds and aquatic animals.

2.3 Materials and Methods

Hindlimb dissections were performed for species representing four of five independent lineages of extant foot-propelled swimming birds and one, non-swimming outgroup. We obtained bird carcasses from rehabilitation

centers. The birds had either been brought to the center as carcasses or deceased while in care. Once at the re-

habilitation center, all carcasses were frozen (-18 °C) before transport to the Concord Field Station (CFS, Bed-

ford, MA). The following six species were collected from local rehabilitation centers including the Tufts Wildlife

Clinic (North Grafton, MA) and the New England Wildlife Center (Weymouth, MA): mallard (*Anas platyrhyn-*

chos), Canada goose (*Branta canadensis*), mute swan (*Cygnus olor*), double crested cormorant (*Phalacrocorax*

auritus), red-throated loon (*Gavia stellate*), and common loon (*Gavia immer*). Western grebe (*Aechmopho-*

rus occidentalis) carcasses were collected at the Wildlife Center of the North Coast (Astoria, Oregon), and then

shipped on dry ice to the CFS. All collections were covered by federal (MB005348-1) and state (Oregon 130-12,

Massachusetts 050.13SAL) scientific collecting permits. American coots, representing the fifth independent lin-

eage of extant foot-based swimming bird have been comprehensively dissected in a prior study (Rosser et al,

1992). Non-swimming helmeted guineafowl (*Numida meleagris*) were obtained from a local breeder and raised at

the CFS before being humanely euthanized using an overdose of Euthasol administered intravenously following

approved Harvard University IACUC procedures. In total, 43 carcasses were collected between 2013 and 2015.

Before dissection, we thawed each carcass at 2 °C. Thawed carcasses were weighed (Ranger RC6RS, Omaha

Corp., NJ, USA or PTHK, Mettler Toledo International, Inc., OH, USA) and emaciated birds were identified by

comparison to published normal weight ranges (Rodewald, 2015). We removed all emaciated carcasses from the

study and either donated the material to the Museum of Comparative Zoology (Cambridge, MA) or disposed

of the carcass as dictated by the collection permits. The right hindlimb and pelvis were plucked of feathers and

each hindlimb muscle was dissected (see Tables 2.1 and 2.2 for a list of all dissected muscles). Before removal, each

muscle was photographed with the limb in an approximate mid-stance or mid-swimming stroke position. After

removal, each muscle was weighed and analyzed for muscle length, fiber length, pennation angle, tendon mass,

and tendon length, which will form the basis for a companion paper.

Drawings of the pelvis and hindlimb skeleton were based from specimens from the Museum of Comparative

Zoology Ornithology Collections. We photographed re-articulated skeletal elements and scaled each picture to

actual size to trace or use as reference for our drawings. The specimens used were: 341648, 347156, 347645, 347051, 337606, 342951, 337590, and 347914. We digitally added muscles by overlaying dissection photos on scans of the skeletal drawings and tracing labeled muscle outlines. Our drawn muscles were compared for all specimens and carefully reviewed for accuracy during subsequent dissections of each species.

Table 2.1: Proximal hindlimb muscles dissected and alternate names in other sources. The left column shows abbreviations used in this paper. The right column identifies alternate names used in major avian myology works. If an alternate name is not identified for a given source it is either not mentioned in that work or uses the name listed in the "Full Muscle Name" column.

	Full Muscle Name	Alternate Names
IC	Iliotibialis cranialis	Extensor iliotibialis anterior [Ow] Iliotibialis internus s. sartorius [GS] Sartorius [Be, Ga73, GB, Ha, Hu, Sh, Wi]
ILPR	Iliotibialis lateralis pars preacetabularis	Extensor iliotibialis lateralis [Ow] Gluteus maximus [Be] Gluteus primus [Fo, Sh] Iliotibialis [GB, Hu] Iliotibialis anterior and Iliotibialis medius/tensor fasciae [GS] Tensor fasciae pars preacetaular [Ga73] Triple muscle [Ha]
ILPO	Iliotibialis lateralis pars postacetabularis	Extensor iliotibialis lateralis [Ow] Gluteus maximus [Be] Gluteus primus [Fo, Sh] Iliotibialis [GB, Hu] Iliotibialis posterior/gluteus posterior [GS] Tensor fasciae pars postacetaular [Ga73] Triple muscle [Ha]
ITCR	Iliotrochantericus cranialis	Gluteus iii [Ga73] Gluteus minimus [Be, Sh] Iliacus [Fi] Iliotrochantericus anterior [GS, GB, Hu] Iliotrochantericus anticus [Wi] Opponens quadratus femoris [Ha]
ITM	Iliotrochantericus medius	Gluteus minimus [Be] Iliacus [Ha]
ITCA	Iliotrochantericus caudalis	Gluteus ii [Ga73] Gluteus medius [Be, Ha, Sh] Gluteus profundis [Ow] Iliotrochantericus posterior [GS, GB, Hu] Iliotrochantericus posticus [Wi]

Table 2.1 – continued from previous page

	Full Muscle Name	Alternate Names
IF	Iliofibularis	Biceps cruris [Ga73] Biceps femoris [Be, GB, Ha, Hu, Wi] Biceps flexor cruris [Sh] Extensor iliofibularis [GS, Ow]
IFE	Iliofemoralis externus	Gluteus medius et minimus [GB, Hu] Gluteus minimus [Ha] Gluteus iv [Ga73] Piriformis [Fi]
IFI	Iliofemoralis internus	Iliacus [GB, Hu, Wi] Pectinaeus [Ha] Psoas [Ow]
FCLP	Flexor cruris lateralis pars pelvica	Caudiliofexorius [GS] Flexor cruris lateralis [Ow] Semintendinosus [Be, Fo, Ga73, GB, Ha, Hu, Sh, Wi]
FCLA	Flexor cruris lateralis pars accessoria	Accesorius semitendinosi or Accessory semitendinosus [Be, Fo, Ga73, GB, Ha, Hu, Sh] Caudiliofexorius accessorius [GS]
CFC	Caudofemoralis pars caudalis	Caudilofemoralis pars caudi-femoralis [GS] Caudofemoralis [Ow, Ra] Femorocaudal [Be, Fo, Ga73, Sh] Piriformis pars caudofemoralis [GB, Hu] Semimembranosus [Ha]
CFP	Caudofemoralis pars pelvica	Accessory femorocaudal [He, Fo, Ga73, Sh] Caudilofemoralis pars ilio-femoralis [GS] Piriformis pars iliofemoralis [GB, Hu] Semimembranosus [HaO:]
IS	Ischiofemoralis	Obturator externus [Sh] Quadratus femoris [Ha]
FCM	Flexor cruris medialis	Gracilis [Ha] Ischioflexorius [GS] Semimembranosus [Be, Fo, Ga73, GB, Hu, Sh, Wi]
PIFL	Pubo-ischio-femoralis lateralis	Adductor longus [Sh] Adductor longus et brevis [Wi] Adductor longus et brevis pars externa [GB, Hu] Adductor magnus [Ga73, Ha] Adductor superficialis [Ow] Pubischiofemoralis pars externa [GS] Puboischiofemoralis pars cranialis [Ra]

Table 2.1 – continued from previous page

	Full Muscle Name	Alternate Names
PIFM	Pubo-ischio-femoralis medialis	Adductor longus et brevis [Wi]
		Adductor longus et brevis pars interna [GB, Hu]
		Adductor magnus [Ga73, Ha, Sh]
		Adductor profundus [Ow]
		Pubischiofemoralis pars interna [GS]
		Puboischiofemoarlis pars caudalis [Ra]
OB	Obturator externus and internus	Gemellus and Obturator internus [Sh]
		Obturator and Accessorrii obturatoris [GS]
		Obturatorius lateralis and medialis [Ra]
AM	Ambiens	

Sources:

Be	Beddard, 1896	Ha	Haughton, 1865
Bn	Bennett, 1996	Hu	Hudson, 1937, 1959
Fo	Forbes, 1885	Ow	Owre, 1967
GS	Gadow and Selenka, 1891	Ra	Raikow, 1987
Ga72	Garrod and Darwin, 1872	Sh	Shufeldt, 1890
Ga73	Garrod, 1873, 1874	Va	Vanden Berge, 1979
Ga75	Garrod, 1875	Wi	Wilcox, 1952
GB	George and Berger, 1966		

Table 2.2: Distal hindlimb muscles dissected and alternate names in other sources. The left column shows abbreviations used in this paper. The right column identifies alternate names used in major avian myology works. If an alternate name is not identified for a given source it is either not mentioned in that work or uses the name listed in the "Full Muscle Name" column.

	Full Muscle Name	Alternate Names
FTI	Femorotibialis internus	Femoritibialis internus [GS, Hu, Wi] Vastus internus [Ha, Sh]
FTM	Femorotibialis medius	Cruraeus [Ha, Sh] Femoritibialis medius [GS, Hu, Wi] Vastus medialis [Ow]
FTE	Femorotibialis externus	Femoritibialis externus [GS, Hu, Wi] Vastus externus [Ga73, Ha, Sh] Vastus lateralis [Ow]
FL	Fibularis longus	Peroneus longus [Be, GB, Hu, Ow, Sh, Wi] Peroneus superficialis [GS]
FB	Fibularis brevis	Peroneus brevis [GB, Hu, Wi] Peroneus profundus [GS] Tibialis posticus [Sh]
EDL	Extensor digitorum longus	Extensor digitorum communis [Be, GS, Ga72, Ha] Extensor longus digitorum [Sh]
TC	Tibialis cranialis	Tibialis anterior [GB, Hu, Ow] Tibialis anticus [Be, GS, Ha, Sh, Wi]
GM	Gastrocnemius medialis	Gastrocnemido-solaeus [Ha] Gastrocnemius anticus [Be, GS] Gastrocnemius internal head [Sh, Wi] Gastrocnemius par medialis and pars supermedialis [Ra] Gastrocnemius pars interna [Be, GS, GB, Hu, Ow]
GI	Gastrocnemius intermedia	Gastrocnemido-solaeus [Ha] Gastrocnemius anticus [Fo, Ga72] Gastrocnemius medial head [Wi] Gastrocnemius pars intermedia [Ra, Va] Gastrocnemius pars media [Be, GS, GB, Hu, Ow] Gastrocnemius tibial head [Sh]
GL	Gastrocnemius lateralis	Gastrocnemido-solaeus [Ha] Gastrocnemius external head [Sh, Wi] Gastrocnemius pars externa [Be, GS, GB, Hu, Ow] Gastrocnemius posticus [Fo, Ga72] Gastronemius pars lateralis [Ra, Va]

Table 2.2 – continued from previous page

	Full Muscle Name	Alternate Names
SFPPDII	(Superficialis) Flexor perforans et perforatus digiti II	Flexor perforatus et perforans digiti II [GS] Flexor perforatus indicis secundus pedis [Sh]
SFPPDIII	(Superficialis) Flexor perforans et perforatus digiti III	Flexor digiti interni [Ga72] Flexor perforatus et perforans digiti III [Be, GS] Flexor perforatus medius secundus pedis [Sh]
SFPPDIV	(Superficialis) Flexor perforans et perforatus digiti IV	Flexor externi digiti [Ga72] Flexor perforatus annularis primus pedis [Sh] Flexor perforatus digiti IV [Be, Bn, FS, GB, Hu, Ow, Ra, Wi, Va]
FPDII	Flexor perforatus digiti II	Flexor perforatus indicis primus pedis [Sh]
FPDIII	Flexor perforatus digiti III	Flexor magnus [Ga72] Flexor perforatus medius primus pedis [Sh]
FHL	Flexor hallucis longus	Flexor longus hallucis [Fo, Ga75, Sh] Flexor profundus [Ga72]
FDL	Flexor digitorum longus	Flexor perforans digitorum [Fo, Ga75] Flexor profundus [Ga72] Flexor profundus s. perforans [GS] Flexor perforans digitorum profundus [Sh]
PL	Plantaris	Soleus [Sh]
PO	Popliteus	

Sources:

Be	Beddard, 1896	Ha	Haughton, 1865
Bn	Bennett, 1996	Hu	Hudson, 1937, 1959
Fo	Forbes, 1885	Ow	Owre, 1967
GS	Gadow and Selenka, 1891	Ra	Raikow, 1987
Ga72	Garrod and Darwin, 1872	Sh	Shufeldt, 1890
Ga73	Garrod, 1873, 1874	Va	Vanden Berge, 1979
Ga75	Garrod, 1875	Wi	Wilcox, 1952
GB	George and Berger, 1966		

Helmeted guinea fowl
Numida meleagris

5 cm

Pelvis Muscles:
- IC
- ILPR
- ILPO
- ITCA, ITCR
- IF
- IFE
- FCL
- FCM
- CFP, CFC
- IS
- PIFL
- PIFM

Leg Muscles:
- FTE, FTM
- FL
- TC
- GM
- GL
- SFPPDII
- SFPPDIII
- SFPPDIV
- FPDII
- FPDIII
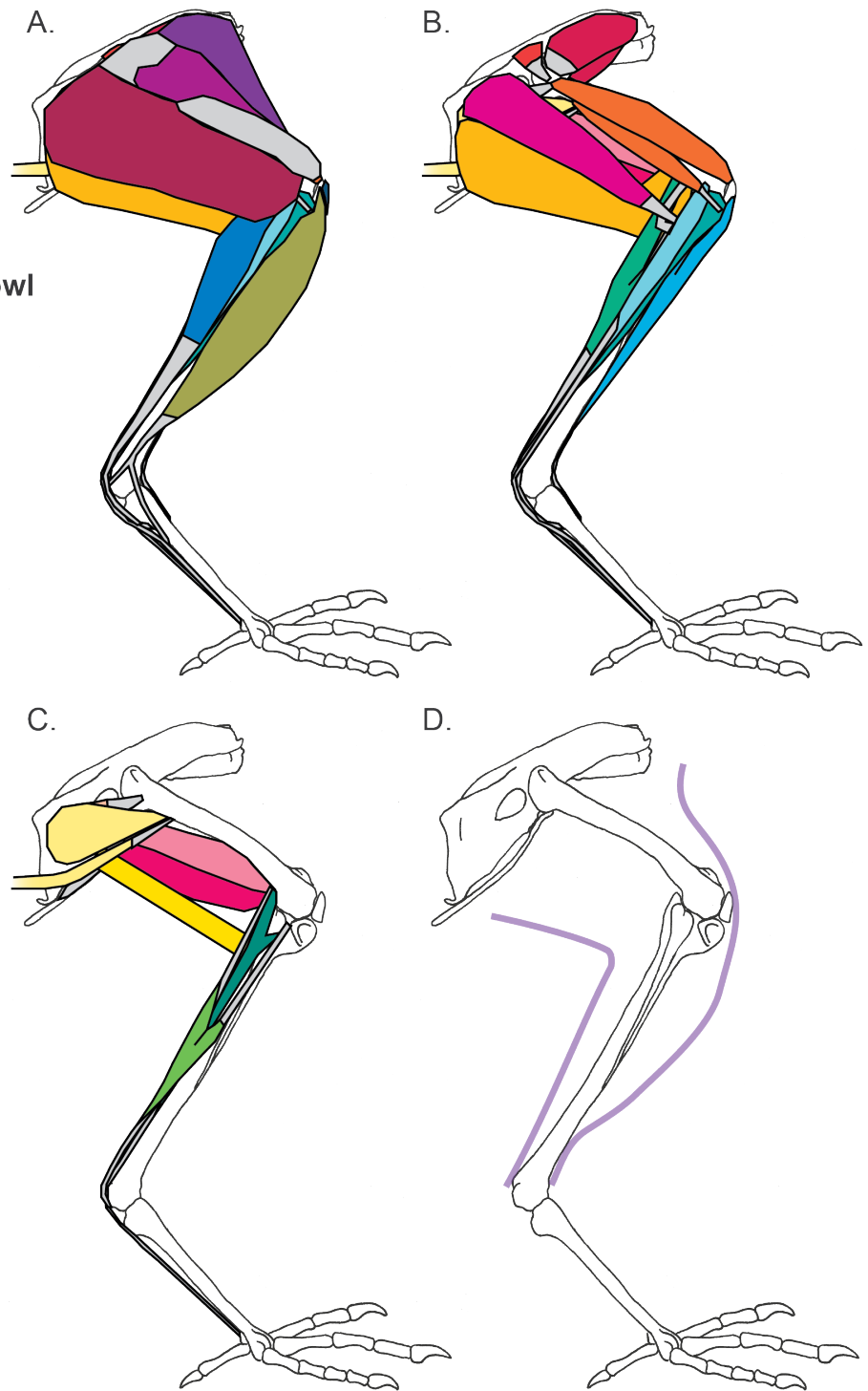
Figure 2.2: Helmeted guinea fowl hindlimb musculature. Major hindlimb muscles drawn based on dissections of several specimens. Panels show the hindlimb with (A) all muscles, (B) superficial muscles removed, (C) superficial and intermediate muscles removed, and (D) skeleton only and outline of limb skin (in purple). Skeleton drawing based on MCZ 341648. Muscle abbreviations listed in Tables 2.1 and 2.2.

Mallard
Anas platyrhynchos

5 cm

A.

B.

C.

D.

Pelvis Muscles:

- IC
- ILPR
- ILPO
- ITCA, ITCR
- IF
- IFE
- FCL
- FCM
- CFP, CFC
- IS
- PIFL
- PIFM

Leg Muscles:

- FTE, FTM
- FL
- TC
- GM
- GL
- SFPPDII
- SFPPDIII
- SFPPDIV
- FPDII
- FPDIII
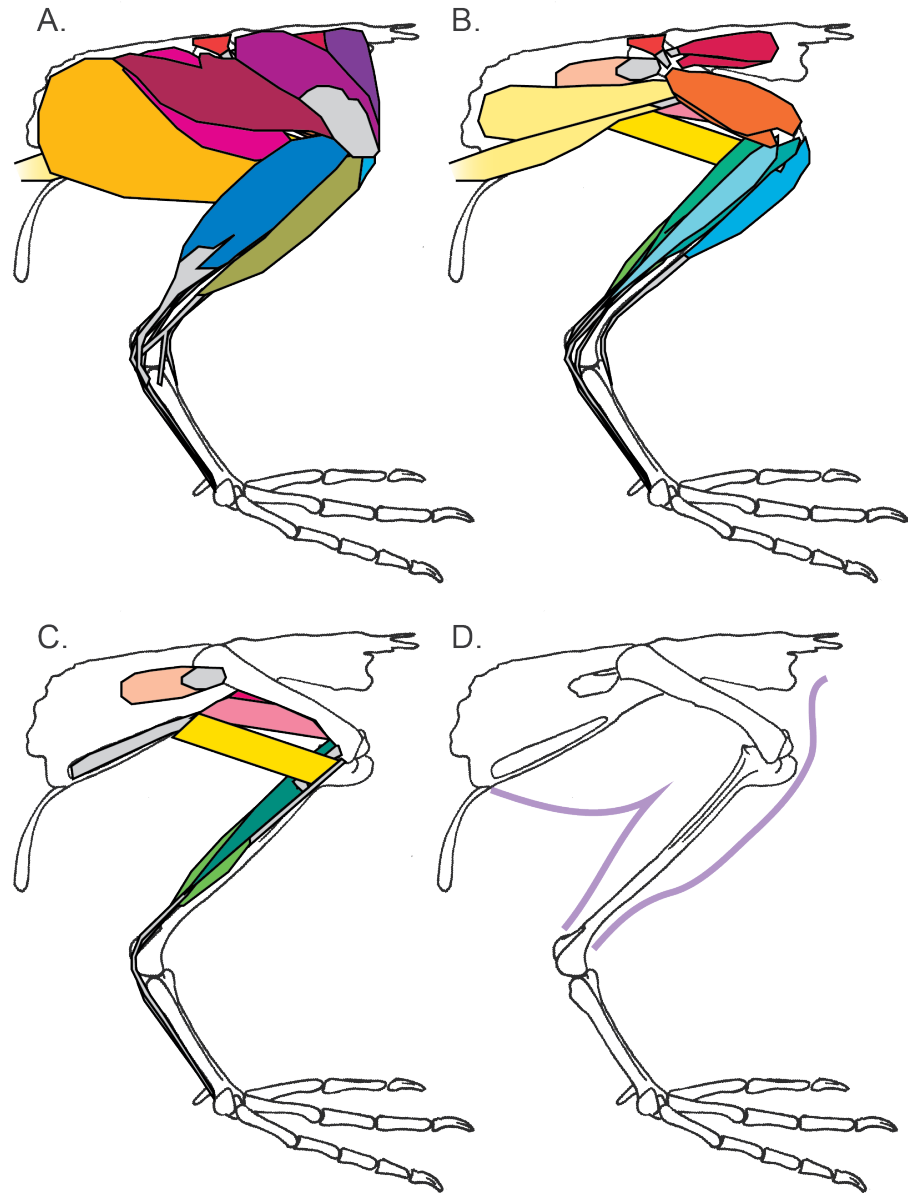
Figure 2.3: Mallard hindlimb musculature. Major hindlimb muscles drawn based on dissections of several specimens. Panels show the hindlimb with (A) all muscles, (B) superficial muscles removed, (C) superficial and intermediate muscles removed, and (D) skeleton only and outline of limb skin (in purple). Skeleton drawing based on MCZ 347156. Muscle abbreviations listed in Tables 2.1 and 2.2.

Canada goose
Branta canadensis

10 cm

Pelvis Muscles:
- IC
- ILPR
- ILPO
- ITCA, ITCR
- IF
- IFE
- FCL
- FCM
- CFP, CFC
- IS
- PIFL
- PIFM

Leg Muscles:
- FTE, FTM
- FL
- TC
- GM
- GL
- SFPPDII
- SFPPDIII
- SFPPDIV
- FPDII
- FPDIII

A.

B.

C.

D.
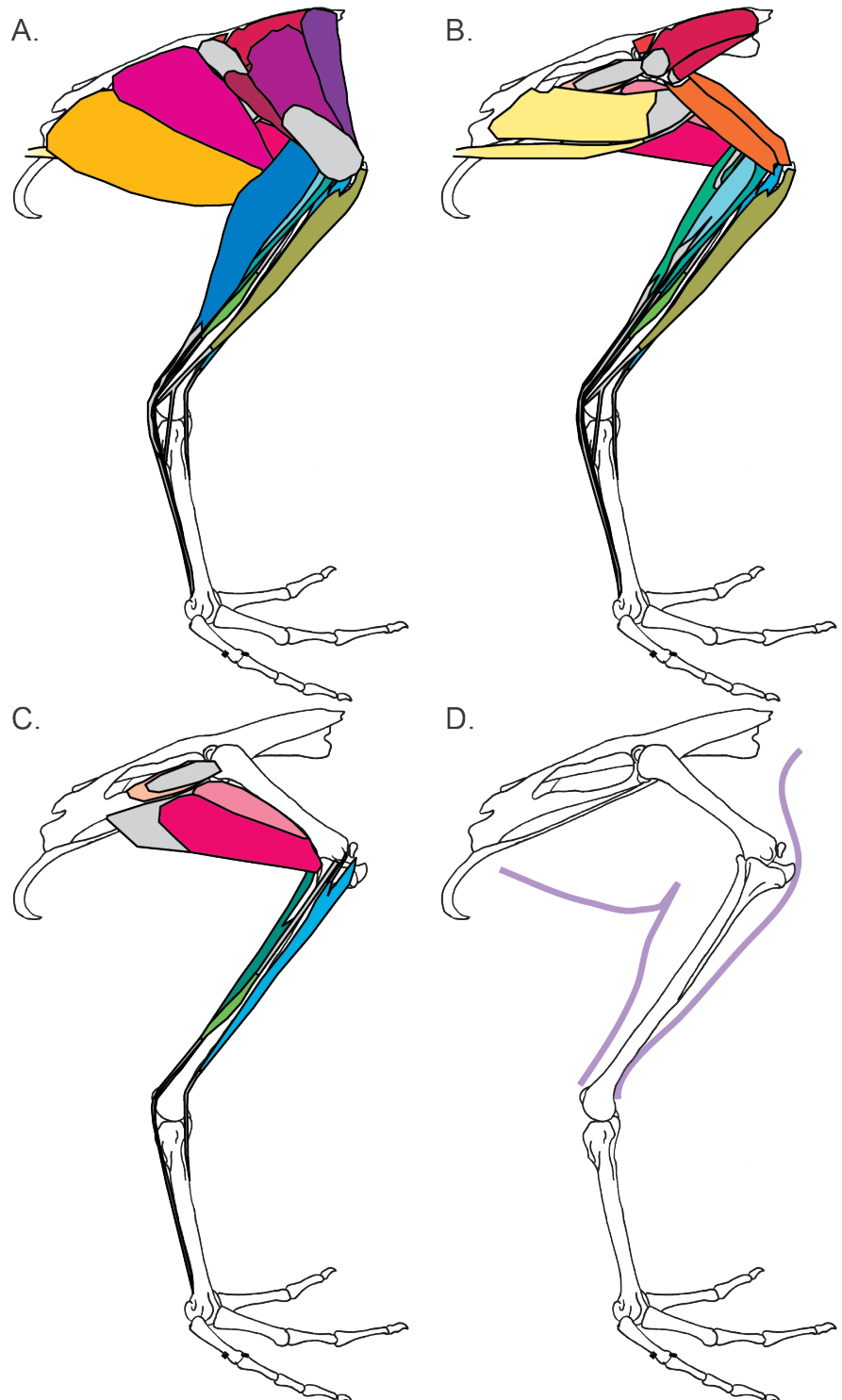
Figure 2.4: Canada goose hindlimb musculature. Major hindlimb muscles drawn based on dissections of several specimens. Panels show the hindlimb with (A) all muscles, (B) superficial muscles removed, (C) superficial and intermediate muscles removed, and (D) skeleton only and outline of limb skin (in purple). Skeleton drawing based on MCZ 347645. Muscle abbreviations listed in Tables 2.1 and 2.2.

Mute swan
Cygnus olor

10 cm

Pelvis Muscles:
- IC
- ILPR
- ILPO
- ITCA, ITCR
- IF
- IFE
- FCL
- FCM
- CFP, CFC
- IS
- PIFL
- PIFM

Leg Muscles:
- FTE, FTM
- FL
- TC
- GM
- GL
- SFPPDII
- SFPPDIII
- SFPPDIV
- FPDII
- FPDIII

A.

B.

C.

D.
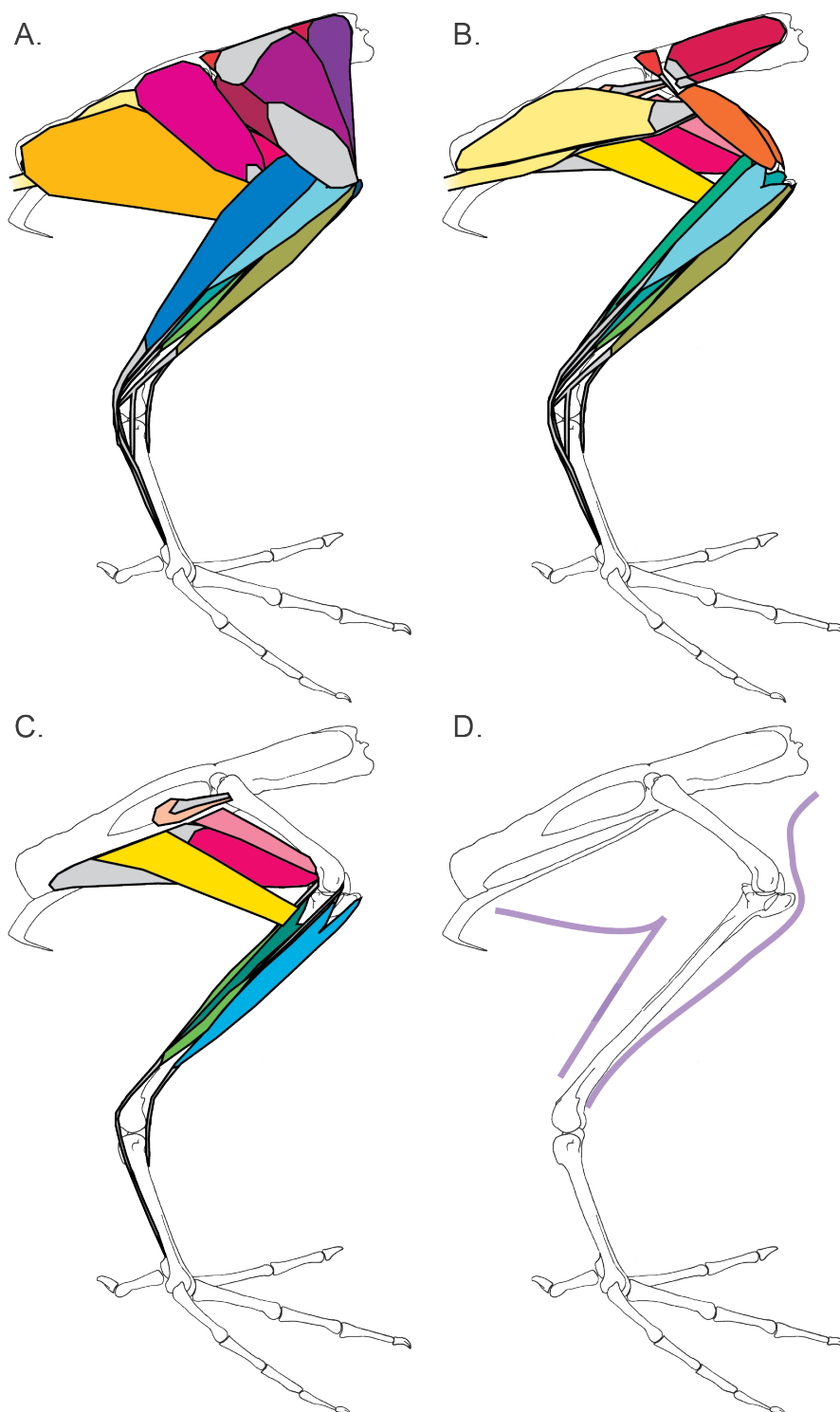
Figure 2.5: Mute swan hindlimb musculature. Major hindlimb muscles drawn based on dissections of several specimens. Panels show the hindlimb with (A) all muscles, (B) superficial muscles removed, (C) superficial and intermediate muscles removed, and (D) skeleton only and outline of limb skin (in purple). Skeleton drawing based on MCZ 347051. Muscle abbreviations listed in Tables 2.1 and 2.2.

27

Double crested cormorant
Phalacrocorax auritus

5 cm

A.

B.

C.

D.

Pelvis Muscles:
- IC
- ILPR
- ILPO
- ITCA, ITCR
- IF
- IFE
- FCL
- FCM
- CFP, CFC
- IS
- PIFL
- PIFM

Leg Muscles:
- FTE, FTM
- FL
- TC
- GM
- GL
- SFPPDII
- SFPPDIII
- SFPPDIV
- FPDII
- FPDIII
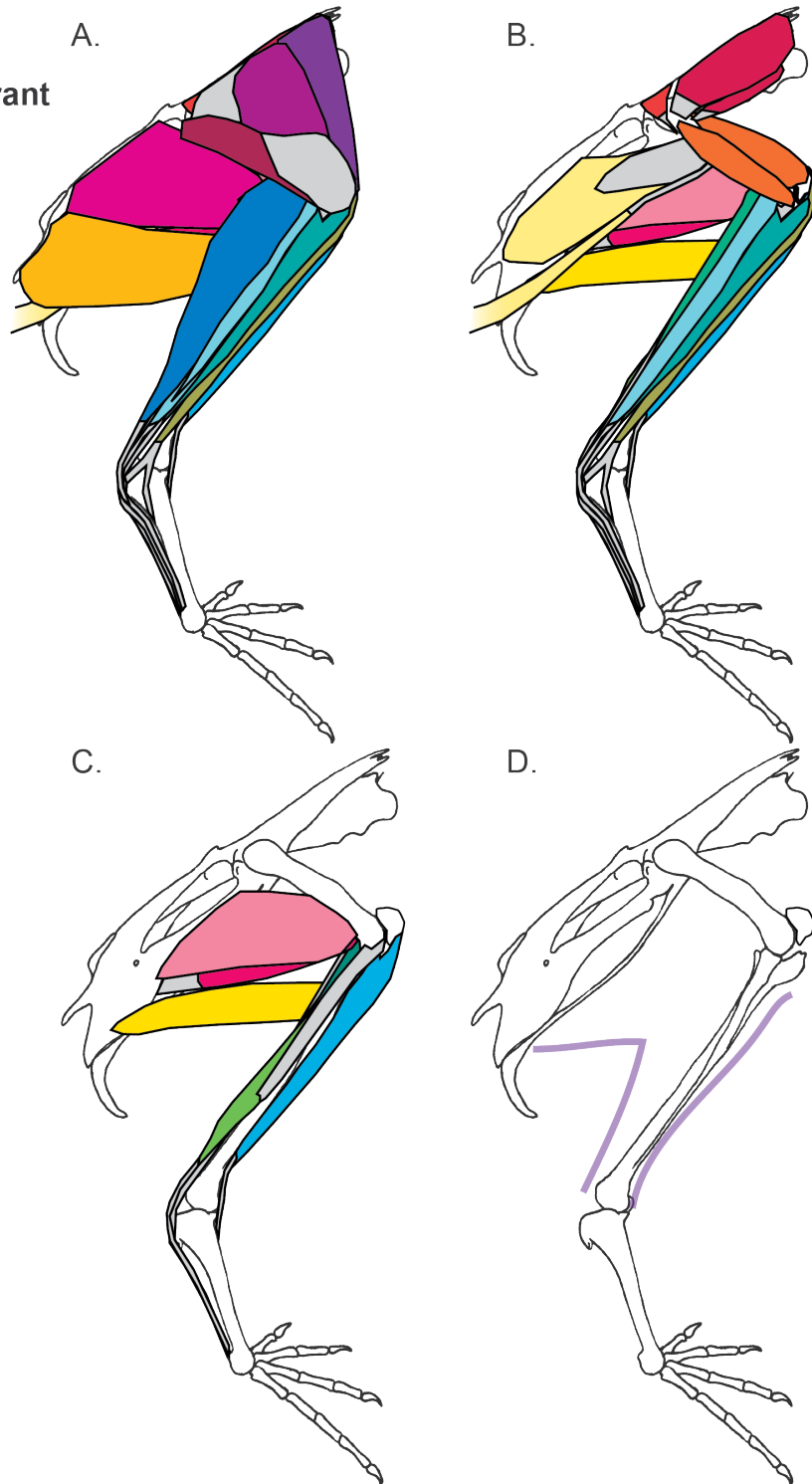
Figure 2.6: Double crested cormornat hindlimb musculature. Major hindlimb muscles drawn based on dissections of several specimens. Panels show the hindlimb with (A) all muscles, (B) superficial muscles removed, (C) superficial and intermediate muscles removed, and (D) skeleton only and outline of limb skin (in purple). Skeleton drawing based on MCZ 337606. Muscle abbreviations listed in Tables 2.1 and 2.2.

Western grebe
Aechmophorus occidentalis

5 cm

Pelvis Muscles:
- IC
- ILPR
- ILPO
- ITCA, ITCR
- IF
- IFE
- FCL
- FCM
- CFP, CFC
- IS
- PIFL
- PIFM

Leg Muscles:
- FTE, FTM
- FL
- TC
- GM
- GL
- SFPPDII
- SFPPDIII
- SFPPDIV
- FPDII
- FPDIII

A.

B.

C.

D.
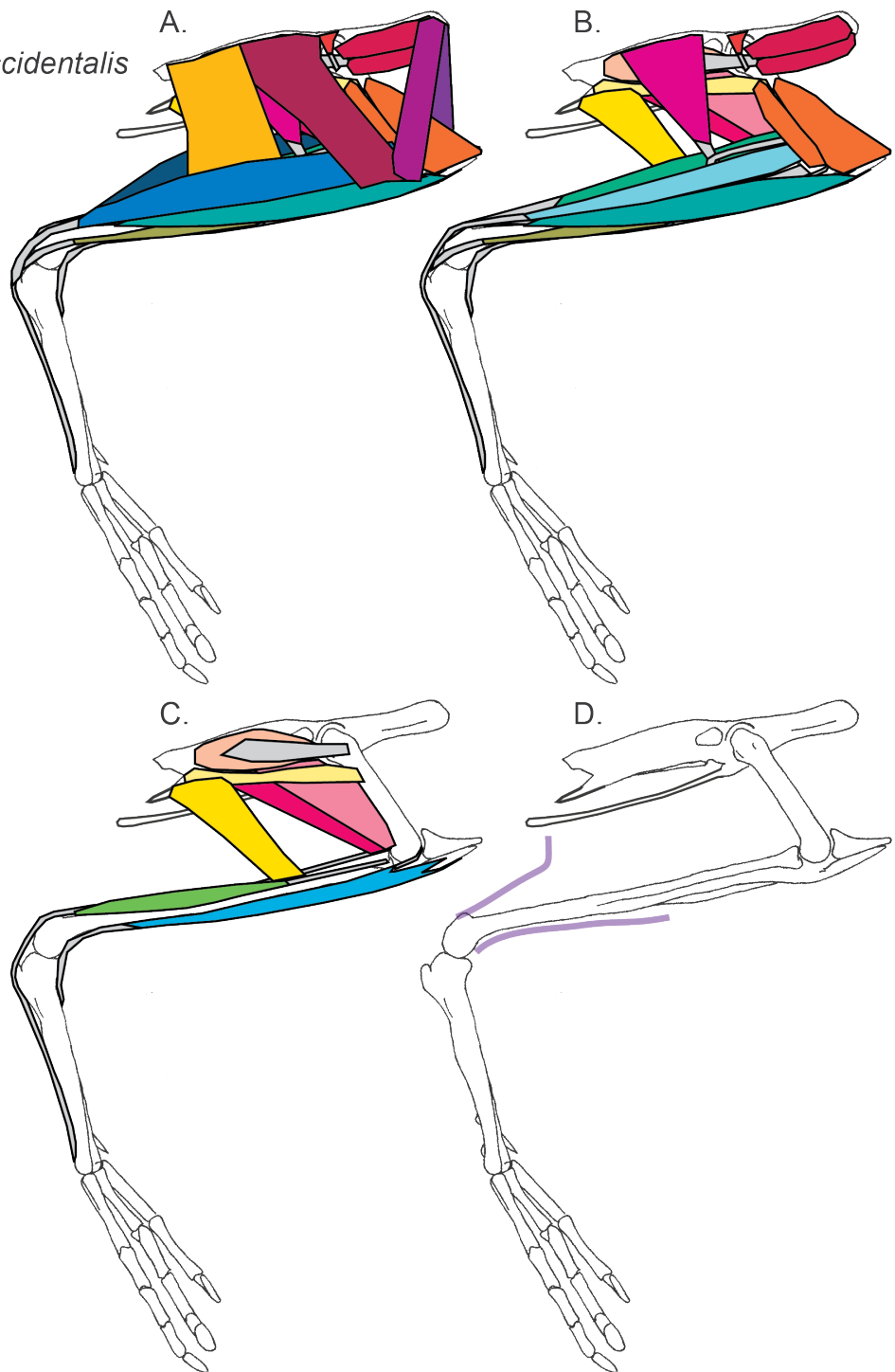
Figure 2.7: Western grebe hindlimb musculature. Major hindlimb muscles drawn based on dissections of several specimens. Panels show the hindlimb with (A) all muscles, (B) superficial muscles removed, (C) superficial and intermediate muscles removed, and (D) skeleton only and outline of limb skin (in purple). Skeleton drawing based on MCZ 342951. Muscle abbreviations listed in Tables 2.1 and 2.2.

Red throated loon
Gavia stellata

5 cm

Pelvis Muscles:
- IC
- ILPR
- ILPO
- ITCA, ITCR
- IF
- IFE
- FCL
- FCM
- CFP, CFC
- IS
- PIFL
- PIFM

Leg Muscles:
- FTE, FTM
- FL
- TC
- GM
- GL
- SFPPDII
- SFPPDIII
- SFPPDIV
- FPDII
- FPDIII

A.

B.

C.

D.
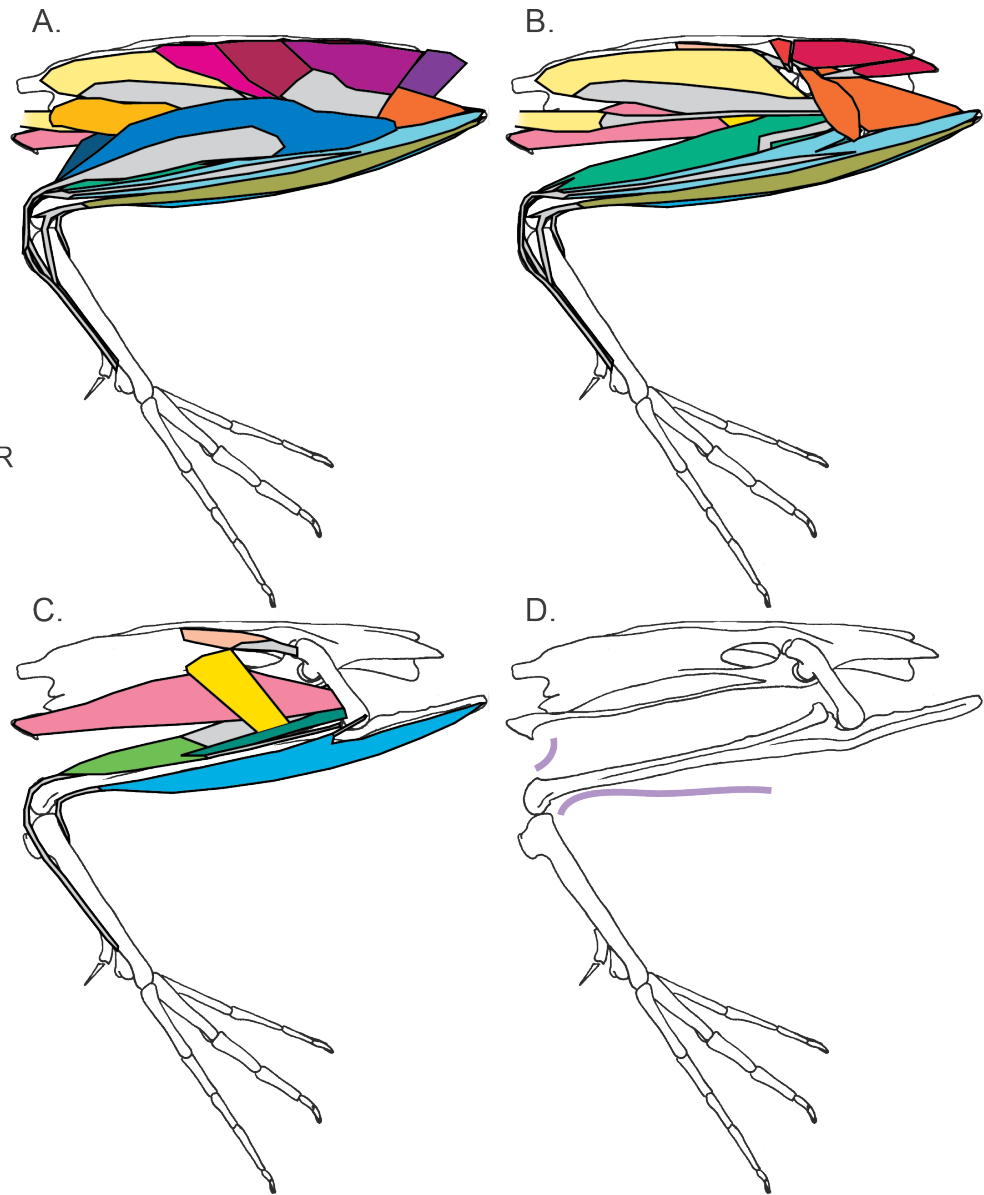
Figure 2.8: Red throated loon hindlimb musculature. Major hindlimb muscles drawn based on dissections of several specimens. Panels show the hindlimb with (A) all muscles, (B) superficial muscles removed, (C) superficial and intermediate muscles removed, and (D) skeleton only and outline of limb skin (in purple). Skeleton drawing based on MCZ 337590. Muscle abbreviations listed in Tables 2.1 and 2.2.

Common loon
Gavia immer

10 cm

Pelvis Muscles:
- IC
- ILPR
- ILPO
- ITCA, ITCR
- IF
- IFE
- FCL
- FCM
- CFP, CFC
- IS
- PIFL
- PIFM

Leg Muscles:
- FTE, FTM
- FL
- TC
- GM
- GL
- SFPPDII
- SFPPDIII
- SFPPDIV
- FPDII
- FPDIII

A.
B.
C.
D.
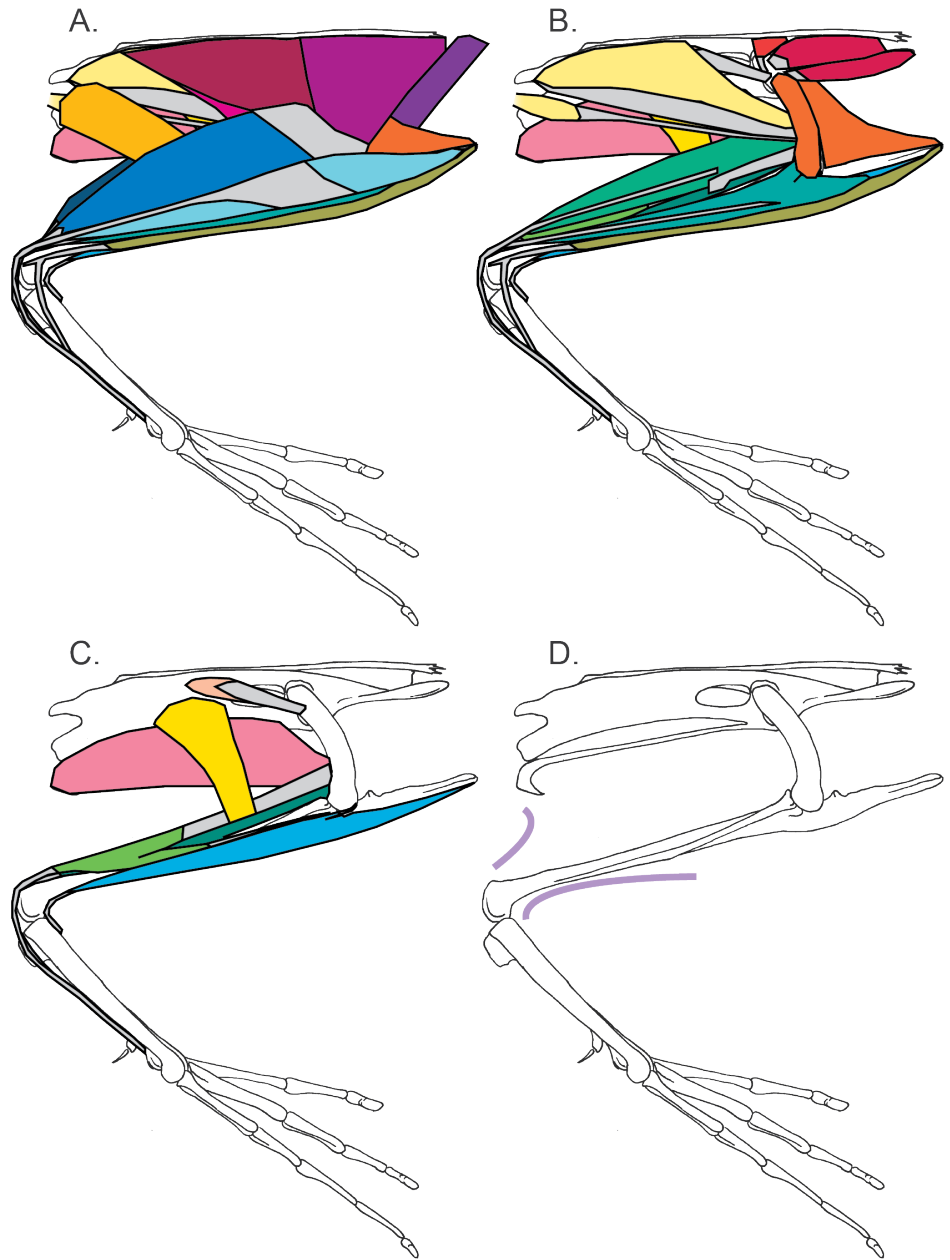
Figure 2.9: Common loon hindlimb musculature. Major hindlimb muscles drawn based on dissections of several specimens. Panels show the hindlimb with (A) all muscles, (B) superficial muscles removed, (C) superficial and intermediate muscles removed, and (D) skeleton only and outline of limb skin (in purple). Skeleton drawing based on MCZ 347914. Muscle abbreviations listed in Tables 2.1 and 2.2.

2.4 Results and Discussion

Diving birds incorporate the proximal hindlimb within the skin covering the abdomen in order increase hydrodynamic streamlining. In non-swimming and surface-swimming birds (including guineafowl and the Anatidae species analyzed in this study), the hindlimb extends away from the abdomen with free mobility at the hip and knee (Figure 2.2-5 D). In contrast, specialized divers (grebes and loons) tuck the proximal portion of the leg against the ribs, keeping the femur and most of the tibiotarsus within the skin overlying the abdomen (Figure 2.7-9 D). Double-crested cormorants represent an intermediate stage of specialization with high mobility both underwater and on land. Accordingly, cormorants incorporate an intermediate extent of the leg adjacent to the abdomen with only half of the tibiotarsus extending away from the body (Figure 2.6 D). Integrating the proximal portion of the leg adjacent to the abdomen streamlines the body for swimming by creating a smooth surface that is less likely to create turbulence or incur detrimental drag force (Fish, 1993). An enlarged flange of bone that extends above the acetabulum, the antitrochanter, aids this position of the hindlimb. The antitrochanter increases femoral extension and laterally pivots the femur away from the vertebral column in specialized diving birds (Hertel and Cambell Jr, 2007). The lateral orientation of the femur permits some diving birds to paddle their feet laterally instead of beneath (ventral to) the body as in surface swimmers (Ribak and Swallow, 2010; Johansson and Norberg, 2001; Provini et al., 2012). However, a laterally-directed femur and restriction of the proximal limb within the body wall skin reduces hip and knee mobility, preventing the feet from being positioned forward underneath the body's center of mass while standing on land. Instead, specialized swimmers assume a more vertical body position while on land to prevent toppling forward (Abourachid, 2000). Specialized diving birds that incorporate the proximal hindlimb into the abdominal skin streamline the body for swimming therefore face a tradeoff with stability on land.

Incorporating the proximal hindlimb inside of the body skin also facilitates large shifts in muscle attachments on the femur and tibiotarsus in specialized diving birds. Most hindlimb muscles demonstrate some anatomical

32

variation across the species studied (Tables 2.3-2.4). Here we present a subset of these muscles to highlight the most dramatic variation and discuss functional implications for swimming performance.

2.4.1 Pelvic musculature

Iliotibialis lateralis pars preacetabularis (ILPR)

The large superficial pelvic muscles covering the thigh in most birds are the *iliotibialis lateralis pars preacetabularis* (ILPR) and *pars postacetabularis* (ILPO). The preacetabular portion (ILPR) typically originates via an aponeurosis from the preacetabular iliac crest and inserts on a large aponeurosis that connects to the postacetabular portion of the muscle (ILPO) and the deep *femorotibialis externus* (FTE) muscle. This insertion aponeurosis then inserts on the patellar tendon, patella, and cnemial crest of the tibiotarsus. The ILPR acts to flex the hip and extend the knee.

Conserved across most species analyzed in this study, the ILPR originates on the caudal half of the preacetabular iliac crest. However, the ILPR of the Western grebe is completely fleshy and originates at the most cranial portion of the preacetabular iliac crest (Beddard, 1896). The strap-like muscle partially covers the *iliotibialis cranialis* (IC) muscle, with little connection to the ILPO. However, other specialized swimmers do not mirror this trend. The ILPR and ILPO are well developed in loons and cormorants.

Iliotrochantericus cranialis (ITCR)

Three *iliotrochantericus* muscles lie deep to the ILPR along the preacetabular iliac fossa and rim, inserting onto the femoral trochanter and proximal shaft. The most superficial muscle of this group, and typically the largest, is the *iliotrochantericus caudalis* (ITCA) originating from the iliac fossa. The *iliotrochantericus cranialis* (ITCR) originates from the ventral rim of the preacetabular ilium, showing variation in the length and location of its attachment across species. The *iliotrochantericus medicus* (ITM) is the smallest of the muscles, originating from the caudal portion of the preacetabular ilium ventral rim. All three *iliotrochantericus* muscles act to abduct the

hip and medially rotate the femur, causing abduction of the distal limb (Gatesy, 1994). In bipedal running birds, these muscles are active during stance phase to stabilize the hip and prevent pelvic roll (Gatesy, 1999).

While in most bird species the ITCR is much smaller than the ITCA (George and Berger, 1966), in grebes and loons the ITCR is very well-developed, approximately equal in size to the ITCA. This convergent pattern may partially result from pelvic shape. Diving birds possess a particularly long and narrow pelvis, with a thin iliac fossa but long iliac ventral rim (Johnsgard, 1987; Hinić-Frlog and Motani, 2010). Yet, the relatively large size of the ITCR may also serve a functional role. To dive underwater grebes and loons must generate force to both power forward propulsion and oppose buoyancy. To oppose buoyancy when not descending exactly vertically, diving birds must produce a component of force directed ventrally. Yet, grebes and loons swim by paddling their feet lateral to the body, with the femur at a large splay angle (Hertel and Cambell Jr, 2007). With the legs in this orientation, a ventrally-directed force will act on the feet to adduct the limbs. If the ITCR is active during the force-producing power stroke, analogous to stance phase in running birds (Gatesy, 1999), the ITCR would oppose limb adduction to stabilize the hip joint. Hip stabilization in diving birds is further aided through a large antitrochanter that braces against hip abduction (Hertel and Cambell Jr, 2007). A relatively large ITCR may serve as one of several anatomical features that reduce hip mobility to streamline the body.

Iliofibularis (IF)

The *iliofibularis* (IF) is a large superficial, triangular muscle arising from the postacetabular ilium. It forms a thick tendon, which passes through a tendinous loop attached to the distal femur, the *ansa fibularis* or IF loop, then travels distally along the tibiotarsus to insert on the fibular tubercle. The IF acts as a knee flexor and hip extensor.

In guineafowl, surface swimmers, and cormorants, the IF inserts onto the tibiotarsus at one-third its length distal to the knee joint. However, in specialized diving birds, grebes and loons, the insertion shifts to approximately halfway down the tibiotarsal shaft. The increased moment arm of the IF likely helps stabilize the knee joint by opposing knee extension moments caused during paddling. The power stroke of paddling birds primar-

ily involves ankle extension, moving the foot from an acutely dorsiflexed position to plantarflexion (Provini et al., 2012; Carr, 2008; Johansson and Norberg, 2001). During this motion, the reaction pressure acting on the foot acts in front of the knee creating an extensor moment at the knee. Without counteracting this moment, the knee would extend, driving the feet away from the body, resulting in increased drag that would resist forward motion of the body (Fish, 1993; Pennycuick et al., 1996). Shifting the insertion of the IF distally may allow specialized diving birds to effectively oppose large knee extensor moments produced by strong paddling forces.

Flexor cruris lateralis (FCL)

The *flexor cruris lateralis* (FCL) muscle lies caudal to the IF, originating on the caudal portion of the ilium, and in some cases, ischium. Many species possess two FCL muscles: the main muscle belly, called the *flexor cruris lateralis pars pelvica* (FCLP), and the accessory head, the *flexor cruris lateralis pars accessoria* (FCLA). The FCLP inserts onto the proximal, posterior tibiotarsus shaft with connections to the *flexor cruris medialis* (FCM), which insert directly deep to the FCL. Near the distal end of the FCLP is a ligamentous raphe, or seam, serving as the origin of the FCLA and inserting onto the tendon of the *gastrocnemius intermedia* (GI). The FCLA fibers insert onto the distal, posterior femoral shaft. Through this three-muscle linkage, the FCL acts in hip extension, knee flexion, and ankle extensor (Ellerby and Marsh, 2010).

The FCLA is present broadly across the avian phylogeny, in paleognathae, Galliformes, and nearly all passerines (George and Berger, 1966). However, the accessory head has been reported absent in almost all swimming birds, except for coots (*Fulica*), as well as in trogons and some woodpeckers (George and Berger, 1966). In Galliformes, the FCLA and FCLP are coactive in late stance during running, especially at an upward incline, suggesting that the FCLA primarily functions to enhance hip extension for fast movements (Ellerby and Marsh, 2010; Ellerby et al., 2005; Rubenson et al., 2006). The repeated evolutionary loss of the FCLA in swimming birds may result from reduced movement at the hip during swimming (see below).

The insertion of the FCLP shifts distally along the tibiotarsus with swimming ability. In non-swimming

guineafowl, the FCLP inserts at the most proximal portion of the posterior tibiotarsal shaft. In surface swimmers, the insertion centers around one-fifth or one-forth of the tibiotarsal shaft length distal to the knee. In specialized divers, the FCLP inserts one-third or halfway down the tibiotarsal shaft. A more distal FCLP insertion enhances the muscle's capacity to produce an extension moment at the hip and flexion moment at the knee, similar to the IF as discussed above. This distal shift could be facilitated by the elongation of the postacetabular ilium in diving birds (Johnsgard, 1987; Hinić-Frlog and Motani, 2010), resulting in a caudal shift of the FCLP origin relative to the hip. Taken to an extreme in loons, the FCLP primarily originates from the most caudal flange of the ischium (Figure 2.8-9). The evolutionary extension of the postacetabular pelvis in diving birds shifts the whole FCLP muscle distally along the tibiotarsus increasing the FCLP moment arm around the hip and knee.

Without the accessory head in swimming birds, the FCLP acts as a hip extensor and knee flexor. It is active during mallard surface swimming from slightly before the power stroke until midway through the recovery stroke (Carr, 2008). While walking, the FCL shortens during activation; however, during swimming it contracts almost isometrically, suggesting it acts to prevent motion at the hip and knee throughout the power stroke. Reducing hip motion and maintaining a flexed knee throughout swimming preserves a relatively streamlined body shape (Fish, 1993; Pennycuick et al., 1996). Despite this important function, the FCLP is relatively small in specialized diving birds. The muscle's reduced size could result from increased FCLP hip and knee moment arms in diving birds, which permit a reduction in muscle strength while maintaining the same joint moment capacity. Although experimental evidence does not exist for FCLP function in diving birds, it most likely serves a similar role as in mallards (Carr, 2008): resisting movement of the hip and knee throughout paddling and especially during the power stroke

2.4.2 Limb musculature

Femorotibialis medius (FTM)

Three *femorotibialis* muscles comprise the deep thigh musculature. The *femorotibialis medius* (FTM) originates along the anterior surface of the femur and inserts on the patella and patellar tendon. The FTM fuses with the *femorotibialis externus* (FTE) along the lateral surface of the femur, splitting only at the proximal origin. The FTM acts as a knee extensor.

The FTM is typically the largest *femorotibialis* muscle, but reaches an extreme size in specialized diving birds. Grebes and loons posses an exceptionally elongate cnemial crest, with a similarly extended patella in grebes (Shufeldt, 1904; Beddard, 1896) and a completely fused patella in loons (Shufeldt, 1913; Wilcox, 1952). Cormorants possess a somewhat expanded, bulky patella (Shufeldt, 1913; Owre, 1967), but its size is not as large as the knee structures in grebes and loons. In these specialized divers, the FTM muscle attaches to the entire posterior surface of the patella (grebes) or cnemial crest (loons), without contributing to a patellar tendon. With both an expanded size and increased moment arm, the FTM can produce comparatively large knee extension moments in diving birds. While the activation pattern of the FTM has never been studied, the flexion-extension immobility of the knee during swimming suggests that the FTM acts to reduce knee motion. The FTM may help oppose strong knee flexion moments produced by the IF and FCL, or could prevent knee flexion as the foot experiences backward drag during the recovery stroke or during steering maneuvers.

Gastrocnemius (GM, GI, GL)

The largest limb muscle is the *gastrocnemius*, consisting of three heads that form the common calcaneal (or Achilles) tendon. The medial head (GM) covers most of the internal shank, originating on the medial patella, cnemial crest, and proximal tibiotarsus. The lateral head (GL) originates from the posterolateral femoral shaft. The intermediate head (GI) is much smaller than the GM or GL, originating from the distal posterior femur with ad-

37

ditional fibers originating from the proximal posterior tibia in cormorants, grebes, and loons. Guineafowl have a common *gastrocnemius* aponeurosis on which all three heads insert. In all other species examined here, the GI tendon combines with the GM tendon, which then combines with the LG tendon to form the calcaneal tendon and insert on the tibial cartilage overlying the hypotarsus. All three heads act as ankle plantarflexors. The GI and GL also act to flex the knee.

All three *gastrocnemius* heads are relatively large in diving birds. In cormorants, grebes, and loons, the GI is unusually well-developed. In grebes and loons, the expanded GM origin extends from the tip of the medial cnemial crest to partway down the tibiotarsus shaft. In loons, the GL is especially enlarged with an origin extending across two-thirds of the femur. With the increased size of the *gastrocnemius* muscles, specialized diving birds can produce stronger plantarflexion moments to power paddling.

Size variation among the three *gastrocnemius* heads in specialized swimmers may demonstrate the importance of GI and GL biarticular actions. The GL and GM heads of a mallard produce approximately equal stress (force normalized for muscle area) while walking but not during surface swimming, which favors the GL (Biewener and Corning, 2001). This pattern may simply represent unequal recruitment under lower-force swimming conditions (Biewener and Corning, 2001). But, since the GL acts at the knee while the GM only acts at the ankle, the unequal contributions of the two muscles during swimming could also demonstrate a preference for concurrent knee flexion with ankle plantarflexion. Two other anatomical patterns support this theory. First, the GI, which also acts as both ankle plantarflexor and knee flexor, is enlarged in diving birds. Second, the more distal insertions of the IF and FCL increase their capacity to produce knee flexion moments in highly specialized divers, supporting the importance of knee flexion in swimming. Enlarged GI and GL heads could represent a demand for knee stabilization throughout ankle plantarflexion motion of the power stroke.

The effect of the enlarged and more powerful *gastrocnemius* in diving birds is augmented through an increased moment arm of the calcaneal tendon. In grebes, loons and especially cormorants, the hypotarsus (the proximal posterior portion of the tarsometatarsus) expands posteriorly away from the ankle center of rotation (Owre, 1967;

Mayr, 2016). A protruding hypotarsus increases the calcaneal tendon moment arm around the ankle joint, further enhancing the capacity of diving birds to propel their feet backward and power underwater swimming.

Digital flexor muscles (SFPPDII, SFPPDIII, SFPPDIV, FPDII, FPDIII)

Deep to the *gastrocnemius*, six muscles travel along the shank to insert on the plantar surface of the phalanges of the toes. The most superficial muscle on the lateral shank is the *(superficialis) flexor perforans et perforatus digiti II* (SFPPDII). The *(superficialis) flexor perforans et perforatus digiti III* (SFPPDIII) lies deep and lateral to SFPPDII. The *(superficialis) flexor perforans et perforatus digiti IV* (SFPPDIV) lies deep and medial to the SFPPDII, traveling along the posterior surface of the shank. Deep to these muscles, the *flexor perforatus digiti III* (FPDIII) muscle originates from two tendons, forming two muscle heads at one-third to one-half of the way down the tibiotarsus shank. The two heads fuse along the distal tibiotarsus, forming a single insertion tendon. The *flexor perforatus digiti II* (FPDII) also has two heads, one sometimes having a tendinous origin from the femur and the other from the common digital flexor tendon. The heads fuse proximally along the tibiotarsus and travel in between the FPDIII heads. The insertion tendon of each digital flexor muscle crosses the posterior ankle (see Garrod, 1875; Hudson, 1937; Mayr, 2016 for tendon-hypotarsus anatomy), travels through a sheath along the posterior tarsometatarsus, and inserts onto the phalanges of the digits. These muscles act mostly as digital flexors and ankle plantarflexors, with the SFPPDIV, FPDII, and FPDIII also acting as knee flexors.

Based on our comparative analysis, we propose changing the name of the digit IV flexor and adding superficialis to the name of three digital flexors. The currently accepted nomenclature of the digital flexor muscles derives from the superficial tendons perforating the deeper tendons after crossing the MTP joint. However, digit IV only has one digital flexor muscle, automatically classifying it as a perforatus muscle and not a perforans et perforatus muscle. Yet, the ultimate insertion of the digit IV flexor muscle onto the fourth phalanx suggests a homology with the perforans et perforatus muscles for digits II and III. To emphasize the grouping of these muscles, we propose adding superficialis to their names and identifying the digit IV flexor as the *(superficialis) flexor*

perforans et perforatus digiti IV (SFPPDIV).

All superficial digital flexors are relatively enlarged in diving birds, particularly in loons. The relatively large size of the superficial digital flexor muscles in specialized diving birds supports the importance of their role in powering underwater paddling. The bulky patella in cormorants and elongated cnemial crest in grebes and loons expand the origin for the SFPPDIII. In loons, the second head of the SFPPDII extends proximally along the anterolateral cnemial crest. Loons also possess an exceptionally large SFPPDIV, originating from half of the femur. The relative increase in the SFPPDIV origin could result from maintaining muscle size but with a relatively shortened femur (Hinić-Frlog and Motani, 2010; Raikow, 1985). However, the expanded SFPPDIV origin size is likely not only a consequence of a shortened femur since grebes do not demonstrate a similar SFPPDIV origin expansion but do possess a relatively short femur (Hinić-Frlog and Motani, 2010). In diving birds, large digital flexors produce stronger MTP and ankle flexion forces, and help to maintain foot shape, to power effective swimming.

Unlike their closest relatives, Western grebes exhibit tendon calcification in many distal limb muscles. Some extent of hindlimb tendon calcification is present in almost all lineages of birds (Hudson, 1937; Landis and Silver, 2002; Hutchinson, 2002). However, the closest relatives to grebes, flamingos and shorebirds, do not have multiple if any calcified tendons (Bennett, 1996; Vanden Berge, 1970; Weldon, 1883). Past studies have either identified only two calcified tendons in grebes (Vanden Berge and Storer, 1995) or generally remarked on the presence of calcification without specifying which tendons (Bennett, 1996). Here, we present the first known record of extensive calcification in grebe tendons (Hudson, 1937; Beddard, 1896; George and Berger, 1966). In Western grebes, the insertion tendon of every superficial digital flexor is calcified, along with the origin tendon of the FPDIII medial head.

The unusual calcification in the digital flexor tendons of Western grebes may represent an adaption to high forces experienced during a seasonal breeding display performed by males and females. Previous work on calcified tendons, primarily using the turkey *gastrocnemius*, suggests that tendons calcify in response to strong tensile forces to prevent rupture of tendon cells (Landis and Silver, 2002). However, theoretical peak swimming force

estimates for cormorants (15-20N or 0.70-0.93 body weights, BWs; Ribak et al., 2004), the closest available proxy for grebes, do not reach peak running forces in birds with calcified tendons (60-75N or 1.4-2.1 BWs in turkeys; Roberts et al., 1998; Birn-Jeffrey et al., 2014). Instead, the need for tendon calcification in grebes could stem from their participation in a physically demanding breeding display involving water surface running, called rushing. During rushing, grebes completely support their body weight through slapping the water surface at up to 20 steps per second and with no help from flapping wings (Clifton et al., 2015). Experimental measurements of slap impulses using taxidermy grebe feet suggest that each foot may experience more than 50N of force (6.4 BWs) while slapping the water surface (an impulse of 0.25 N s over 5ms, Clifton et al., 2015). These values more closely resemble running forces suggesting that grebe calcified tendons may help mitigate high loading of the thin digital flexor tendons during rushing.

2.5 Conclusions

In this study we highlight anatomical trends related to foot-based swimming by directly comparing the hindlimb myology of seven species of swimming birds. Our data draw from historical records as well as new, detailed dissections of eight bird species. We provide a convenient key that summarizes discrepancies in muscle naming from several historical texts to help promote future comparisons across these works.

Birds that excel at swimming using their feet exhibit several anatomical trends conserved across convergent evolutionary lineages. First, specialized diving birds tuck the proximal portion of the hindlimb inside the abdominal wall skin, creating a streamlined body shape but reducing mobility on land. Second, the shifted insertions and therefore increased moment arms of several pelvic muscles (including the ITCR, IF, and FCL) likely help stabilize the hip and knee joints while paddling. Third, as a result of increased moment arms and less mobile hip and knee joints, many pelvic muscles are relatively reduced in diving birds. Lastly, the most specialized divers possess especially enlarged knee structures (the patella, tibiotarsal cnemial crest, or both) increasing attachment areas for the FTM, *gastrocnemius* heads, and digital flexor muscles. The expanded size of these muscles demonstrates the

importance of knee stabilization and strong ankle plantarflexion while paddling. Surface swimmers across a range of body sizes display intermediate stages of these trends. These conserved anatomical patterns suggest that phylogenetically divergent lineages of birds have evolved similar hindlimb muscle features to accommodate the physical demands of foot-based swimming.

Table 2.3: Pelvic musculature origins and insertions. This table shows the origin and insertion of major pelvic muscles dissected in the helmeted guineafowl (GF), mallard (MA), Canada goose (CG), mute swan (MS), double-crested cormorant (DCC), Western grebe (WG), red-throated loon (RTL), and common loon (CL). Attachment points are fleshy unless otherwise noted. GF do not swim. MA, CG, and MS are surface-swimmers of increasing body mass. DCC, WG, RTL, and CL are divers, with the DCC representing an intermediate specialization since it retains the ability to walk. A key for muscle abbreviations can be found in Tables 2.1 and 2.2.

	ILPO	ILPR
GF	O: Aponeurosis from the caudal 1/2 of the preacetabular iliac crest. I: FT aponeurosis to the patellar tendon, lateral patella and GM.	O: The postacetabular iliac crest with some fibers arising underneath FCL from the ischium. I: FT aponeurosis to the lateral patella and cnemial crest with connections to SFPPDII.
MA	O: Aponeurosis from the caudal 1/2 of the preacetabular iliac crest. I: FT aponeurosis to the lateral cnemial crest, the patella, the patellar tendon and FL.	O: Cranial 1/2 of the postacetabular iliac crest. I: FT aponeurosis to the lateral patella and cnemial crest with connections to SFPPDII.
CG	O: Aponeurosis from the caudal 1/2 of the preacetabular iliac crest. I: FT aponeurosis to the lateral cnemial crest, the patella, the patellar tendon and FL.	O: Aponeurosis covering the trochanter of the femur that inserts onto the ilium just dorsal and posterior to the acetabulum. I: FT aponeurosis to the lateral patella and cnemial crest with connections to SFPPDII.
MS	O: Aponeurosis from the caudal 2/3 of the preacetabular iliac crest. I: FT aponeurosis to the patella and lateral cnemial crest and with connections to SFPPDII and SFPPDIII.	O: Aponeurosis from the most cranial postacetabular iliac crest. I: FT aponeurosis to the lateral patella and cnemial crest with connections to SFPPDII.
DCC	O: Aponeurosis from caudal 1/2 of preacetabular iliac crest. I: FT aponeurosis to the patella and lateral cnemial crest and with connections to SFPPDIII.	O: Aponeurosis from the iliac crest just posterior to the acetabulum. I: FT aponeurosis to the lateral cnemial crest and patella.
WG	O: Fleshy from the most cranial section of preacetabular iliac crest partially overlaying IC. I: Fleshy to the lateral patella.	O: Cranial 1/2 of the postacetabular iliac crest. I: Fleshy to the lateral cnemial crest with connections to the superficial digital flexors.
RTL	O: Fleshy from the entire length of the preacetabular ilium and the most caudal lumbar vertebrae. I: FT aponeurosis to the lateral cnemial crest.	O: Cranial 1/2 of the postacetabular iliac crest. I: FT aponeurosis to the lateral cnemial crest.
CL	O: Fleshy from the entire length of the preacetabular ilium and the most caudal lumbar vertebrae. I: FT aponeurosis to the lateral cnemial crest.	O: Cranial 2/3 of the postacetabular iliac crest. I: FT aponeurosis to the lateral cnemial crest.

43

Table 2.3 – continued from previous page

	IC	IFE
GF	O: Cranial 1/2 of the preacetabular ilium with close connection to ILPR. I: Connection to FTI and GM with insertion on the anteromedial patella.	O: Iliac crest dorsal to the acetabulum. I: Tendinous. Posterolateral femoral shaft just distal to the trochanter.
MA	O: Most cranial portion of the preactabular iliac crest. I: Medial cnemial crest of the tibiotarsus, anterormedial patella with connections to the GM.	O: Iliac crest dorsal and slightly caudal to the acetabulum. I: Tendinous. Posterolateral femoral shaft distal to the trochanter and posterior to the ITCR insertion.
CG	O: Most cranial portion of the preacetabular iliac crest. I: Medial cnemial crest of the tibiotarsus, anterormedial patella with connections to the GM and FT fascia.	O: Iliac crest dorsal and slightly caudal to the acetabulum. I: Tendinous. Posterolateral femoral shaft distal to the trochanter.
MS	O: Cranial, preacetabular ilium and iliac crest, and last free lumbar vertebrae. I: Anteromedial patella and medial cnemial crest of the tibiotarsus.	O: Iliac crest dorsal and slightly caudal to the acetabulum. I: Tendinous. Posterolateral femoral shaft distal to the trochanter.
DCC	O: Cranial 1/2 of the preacetabular iliac crest. I: Anteromedial patella with connections to FL.	O: Iliac crest dorsal to the acetabulum. I: Tendionous. Posterolateral femoral shaft distal to the trochanter and proximal to the CFP tendon. Notes: Relatively large muscle.
WG	O: Most cranial section of preacetabular ilium deep to ILPR. I: Medial cnemial crest of the tibiotarsus.	O: Iliac crest dorsal and slightly caudal to the acetabulum. I: Tendinous. Posterolateral femoral shaft distal to the trochanter. Notes: Muscle present contrary to previous studies.
RTL	O: 2-3 last lumbar vertebrae before synsacrum and most cranial aspect of the preacetabular ventral rim. I: Medial cnemial crest of the tibiotarsus.	O: Iliac crest dorsal and slightly caudal to the acetabulum. I: Tendinous. Posterolateral femoral shaft distal to the trochanter.
CL	O: 2-3 last lumbar vertebrae before synsacrum and most cranial aspect of the preacetabular ventral rim. I: Medial cnemial crest of the tibiotarsus with connections to GI.	O: Iliac crest dorsal and slightly caudal to the acetabulum. I: Tendinous. Posterolateral femoral shaft distal to the trochanter. Notes: Missing in some specimen

Table 2.3 – continued from previous page

	ITCR
GF	O: Cranial 2/3 of the ventral rim of the preacetabular iliac fossa. I: Tendinous. Deep to the FTE onto the lateral femoral shaft. Attaches to the femur at 1/4 of its length distal to the hip joint.
MA	O: Ventral rim of the preacetabular iliac fossa. I: Tendinous. Lateral femoral shaft just distal to the trochanter and proximal to the FTE. Attaches to the femur at 1/4 of its length distal to the hip joint.
CG	O: Cranial 3/4 of the ventral rim of the preacetabular iliac fossa. I: Tendinous. Lateral femoral shaft just distal to the trochanter and proximal to the FTE. Attaches to the femur at 1/4 of its length distal to the hip joint.
MS	O: Cranial 3/4 of the ventral rim of the preacetabular iliac fossa. I: Tendinous. Lateral femoral shaft just distal to the trochanter, anterior to the FTE, and proximal to the FTM. Attaches to the femur between 1/8 and 1/4 of its length distal to the hip joint.
DCC	O: Cranial ventral rim of the preacetabular iliac fossa. I: Tendinous. Deep to the FTE onto the lateral femoral shaft just distal to the trochanter. Attaches to the femur at 1/8 of its length distal to the hip joint.
WG	O: Cranial ventral surface and rim of the preacetabular iliac fossa. I: Mostly fleshy with small tendon. Lateral femoral shaft just distal to the trochanter, anterior to the FTE, and proximal to the FTM. Attaches to the femur between 1/8 and 1/4 of its length distal to the hip joint. Notes: Well-developed muscle approximately equal in size to ITCA.
RTL	O: Cranial ventral surface and rim of the preacetabular iliac fossa. I: Tendinous. Lateral femoral shaft distal to the trochanter between FTE and FTM origins. Attaches to the femur at 1/4 of its length distal to the hip joint. Notes: Well-developed muscle approximately equal in size to ITCA.
CL	O: Cranial ventral surface and rim of the preacetabular iliac fossa. I: Tendinous. Lateral femoral shaft distal to the trochanter, superficial to FTM, attaching between FTE and FTM origins. Attaches to the femur at 1/4 of its length distal to the hip joint. Notes: Well-developed muscle approximately equal in size to ITCA.

45

Table 2.3 – continued from previous page

	ITM	ITCA
GF	O: Ventral rim on the preacetabular iliac fossa caudal to the ITCR. I: Tendinous. Lateral surface of the femur just distal to the ITCA and proximal to the ITCR.	O: Preacatabular iliac fossa and iliac crest. I: Tendinous. Trochanter of the femur.
MA	O: Caudal 1/5 of the ventral rim of the preacetabular iliac fossa. I: Tendinous. Forms a thin tendon, which fuses with the proximal ITCR.	O: Preacatabular iliac fossa and iliac crest. I: Tendinous. Trochanter of the femur.
CG	O: Caudal 1/5 of the ventral rim of the preacetabular iliac fossa. I: Tendinous. Forms a thin tendon, which fuses with the proximal ITCR.	O: Preacatabular iliac fossa and iliac crest. I: Tendinous. Trochanter of the femur.
MS	O: Caudal 1/4 of the ventral rim of the preacetabular iliac fossa. I: Tendinous. Lateral femoral shaft proximal to the ITCR tendon and deep to the ITCA tendon.	O: Preacatabular iliac fossa and iliac crest. I: Tendinous. Trochanter of the femur.
DCC	Missing or fused with ITCR.	O: Preacatabular iliac fossa and iliac crest. I: Tendinous. Trochanter of the femur.
WG	O: Most caudal portion of the ventral rim of the preacetabular iliac fossa. I: Tendinous. Thin tendon onto the lateral femoral shaft just proximal to the ITCR and deep to the ITCA tendon.	O: Preacatabular iliac fossa and iliac crest. I: Tendinous. Trochanter of the femur.
RTL	O: Caudal 1/4 of the ventral rim of the preacetabular iliac fossa. I: Tendinous. Lateral femoral shaft just distal to the trochanter and deep to the ITCA tendon.	O: Preacatabular iliac fossa and iliac crest. I: Tendinous. Trochanter of the femur.
CL	O: Caudal 1/4 of the ventral rim of the preacetabular iliac fossa. I: Tendinous. Lateral femoral shaft just distal to the trochanter and deep to the ITCA tendon.	O: Preacatabular iliac fossa and iliac crest. I: Tendinous. trochanter of the femur.

Table 2.3 – continued from previous page

	IF	IS
GF	O: Entire length of the postacetabular iliac crest. I: Tendinous. Fibular tubercle $1/3$rd of the way down the tibiotarsus from the knee joint.	O: Lateral surface of the ischium and ilioischiadic membrane. I: Tendinous. Posterolateral femoral shaft just distal to the trochanter.
MA	O: Cranial $1/2$ of the dorsal postacetabular ilium deep to the ILPO. I: Tendinous. Small aponeurosis to the GL/GI. Large tendon to fibular tubercle $\sim 1/3$rd of the way down the tibiotarsus from the knee joint.	O: Lateral surface of the ischium and ilioischiatic membrane. I: Tendinous. Posterolateral femoral shaft just distal to the trochanter.
CG	O: Cranial $1/2$ of the postacetabular iliac crest and dorsal ilium. I: Tendinous. Small aponeurosis to the GL/GI. Large tendon to fibular tubercle $\sim 1/3$rd of the way down the tibiotarsus from the knee joint.	O: Lateral surface of the ischium and ilioischiadic membrane. I: Tendinous. Posterolateral femoral shaft just distal to the trochanter.
MS	O: Cranial $1/2$ of the postacetabular iliac crest and dorsal ilium. I: Tendinous. Fibular tubercle $1/3$rd of the way down the tibiotarsus from the knee joint.	O: Cranial ischium. I: Tendinous. Posterolateral head of the femur.
DCC	O: Cranial $3/4$ of the postacetabular iliac crest and dorsal ilium. I: Tendinous. Fibular tubercle $1/3$rd of the way down the tibiotarsus from the knee joint.	Absent. References to an IS muscle in previous records misidentify the CFP.
WG	O: Entire length of postacetabular iliac crest and dorsal ilium. I: Tendinous. Fibular tubercle $1/2$ of the way down the tibiotarsus from the knee joint.	O: Cranial postacetabular ilium and ischium I: Tendinous. Posterolateral surface of the trochanter.
RTL	O: Cranial $1/2$ of the postacetabular iliac crest with connections to the CFP. I: Tendinous. Fibular tubercle $1/2$ of the way down the tibiotarsus from the knee joint.	O: Cranial postacetabular ilium, ischium and the ilioischiatic membrane. I: Tendinous. Posterolateral femoral shaft just distal to the trochanter.
CL	O: Cranial $2/3$ of the postacetabular iliac crest and dorsal ilium. I: Tendinous. Fibular tubercle $1/2$ of the way down the tibiotarsus from the knee joint.	O: Cranial postacetabular ilium, ischium and the ilioischiatic membrane. I: Tendinous. Posterolateral femoral shaft just distal to the trochanter.
Notes	Tendon travels through the ansa fibularis (IF loop) before inserting.	

Table 2.3 – continued from previous page

	FCL
GF	O: Most caudal portion of the postacetabular ilium and the first free caudal vertebrae I: Main body inserts on proximal 10% of posterior tibiotarsus shaft, with connections to GI and FCM. Accessory head inserts on the distal posterior femoral shaft.
MA	O: Caudal 1/2 of the postacetabular ilium and 1-2 adjacent caudal vertebrae. I: Proximal 20% of the posterior tibiotarsus shaft between the GM and GI, with connection to FCM.
CG	O: Caudal 1/2 of the postacetabular ilium and adjacent 1-2 caudal vertebrae I: Posterior tibiotarsus shaft at 1/4 shaft length distal to the knee. Travels between GM and GI, with connection to FCM.
MS	O: Caudal 1/2 of the postacetabular ilium and adjacent 1-2 caudal vertebrae I: Posterior tibiotarsus shaft at 1/4 shaft length distal to the knee. Travels between GM and GI, with connection to FCM.
DCC	O: Caudal third of the postacetabular ilium and adjacent 1-2 caudal vertebrae I: Tendinous. Posterior tibiotarsus shaft at 1/3 shaft length distal to the knee. Travels between GM and GI, with connection to FCM.
WG	O: Caudal 1/2 of the postacetabular ilium. I: Posterior tibiotarsus shaft at 1/2 shaft length distal to the knee. Strong connection with GM, GI, and FCM.
RTL	O: Most caudal portion of the ilium and ischium with connections to the CFP. I: Tendinous. Posterior tibiotarsus shaft at 1/3 shaft length distal to the knee, with connection to FCM.
CL	O: Most caudal portion of the ilium and ischium with connections to the CFP I: Tendinous. Posterior tibiotarsus shaft at 1/3 shaft length distal to the knee, with connection to FCM.

48

Table 2.3 – continued from previous page

	CFP	CFC
GF	O: Inside the postacetabular iliac rim and along the ichiatic process. I: Mixed tendinous and fleshy. Proximal posterolateral femoral shaft.	O: Ventral, cranial pygostyle. I: Tendinous. Posterolateral femoral shaft about 1/4 of its length distal to the hip. Passes between the FCL and FCM
MA	O: Caudal 1/2 of the lateral postacetabular ilium and ischiatic process. I: Mixed tendinous and fleshy. Proximal 1/3 of the posterolateral femoral shaft.	O: Ventral, cranial pygostyle. I: Tendinous. Posterolateral femoral shaft about 1/3 of its length distal to the hip. Deep to FCL, superficial to FCM.
CG	O: Caudal 2/3 of the lateral postacetabular ilium and ischiatic process. I: Tendinous. Proximal 1/3 of the posterolateral femoral shaft.	O: Ventral, cranial pygostyle. I: Tendinous. Posterolateral femoral shaft about 1/3 of its length distal to the hip. Deep to FCL, superficial to FCM.
MS	O: Caudal 2/3 of the lateral postacetabular ilium and ischiatic process. I: Tendinous. Proximal 1/3 of the posterolateral femoral shaft.	O: Ventral, cranial pygostyle. I: Tendinous. Posterolateral femoral shaft about 1/3 of its length distal to the hip. Deep to FCL, superficial to FCM.
DCC	O: Caudal 1/2 of the lateral postacetabular ilium and ischiatic process. I: Tendinous. Proximal 1/2 of the posterolateral femoral shaft. Notes: Previously referred to as IS.	O: Ventral, cranial pygostyle. I: Tendinous. Posterolateral femoral shaft about 1/2 of its length distal to the hip. Deep to FCL, superficial to FCM.
WG	O: Caudal 1/2 of the lateral postacetabular ilium and ischiatic process. I: Tendinous. Proximal posterolateral femoral shaft at 1/3 its length distal to the hip.	Absent.
RTL	O: Caudal 3/4 of the lateral postacetabular ilium and ischiatic process. I: Tendinous. Proximal posterolateral femoral shaft at 1/2 its length distal to the hip.	O: Ventral, cranial pygostyle. I: Tendinous. Fuses with CFP tendon to posterolateral femoral shaft about 1/2 of its length distal to the hip. Deep to FCL, superficial to FCM.
CL	O: Caudal 3/4 of the lateral postacetabular ilium and ischiatic process. I: Tendinous and fleshy. Proximal posterolateral femoral shaft at 1/2 its length distal to the knee.	O: Ventral, cranial pygostyle. I: Tendinous. Fuses with CFP tendon to posterolateral femoral shaft about 1/2 of its length distal to the hip. Deep to FCL, superficial to FCM.

Table 2.3 – continued from previous page

	FCM	OB
GF	O: Ventral border of the ischium. I: Aponeurosis of the GI with connections to FCL. Notes: Narrow, strap-like muscle.	O: Medial surface of the ischium, pubis and isciopubic fenestra. I: Tendinous. Posterior proximal margin of the femoral head.
MA	O: Caudal ventral border of the ischium. I: Proximal, posterior tibiotarsus shaft between the GM and GI. Notes: Narrow, strap-like muscle.	O: Medial surface of the ischium, pubis and isciopubic fenestra. I: Tendinous. Posterior proximal margin of the femoral head.
CG	O: Caudal ventral border of the ischium. I: Proximal, posterior tibiotarsus shaft between the GM and GI. Notes: Narrow, strap-like muscle.	O: Medial surface of the ischium, pubis and isciopubic fenestra. I: Tendinous. Posterior proximal margin of the femoral head.
MS	O: Full length of the ventral border of the ischium. I: Fuses with FCL tendon to insert on the proximal posterior shaft of the tibiotarsus. Notes: Wide, somewhat triangular muscle.	O: Medial surface of the ischium, pubis and isciopubic fenestra. I: Tendinous. Posterior proximal margin of the femoral head.
DCC	O: Caudal ventral border of the ischium and caudal pubis. I: Posterior tibiotarsus shaft with FCL tendon. Notes: Narrow, strap-like muscle.	O: Medial surface of the ischium, pubis and isciopubic fenestra. I: Tendinous. Proximal lateral margin of the femoral head.
WG	O: Caudal ventral border of the ischium. I: Posterior tibiotarsus shaft with FCL tendon. Notes: Narrow, very thin, strap-like muscle.	O: Medial surface of the ischium, pubis and isciopubic fenestra. I: Tendinous. Proximal lateral margin of the femoral head deep to IS tendon.
RTL	O: Middle 1/3 of the ventral border of the ischium. I: Posterior tibiotarsus shaft with FCL tendon. Notes: Narrow, strap-like muscle.	O: Medial surface of the ischium, pubis and isciopubic fenestra. I: Tendinous. Proximal lateral margin of the femoral head deep to IS tendon.
CL	O: Middle 1/3 of the ventral border of the ischium. I: Posterior tibiotarsus shaft with FCL tendon. Notes: Narrow, strap-like muscle.	O: Medial surface of the ischium, pubis and isciopubic fenestra. I: Tendinous. Proximal lateral margin of the femoral head deep to IS tendon.
Notes		Includes both externus and internus muscles.

Table 2.3 – continued from previous page

	PIFM	PIFL
GF	O: Cranial 1/3 of the ventral ischium and the aponeurosis of PIFM. I: Distal 1/2 of the posterior femoral shaft. Notes: Strap-like muscle superficial to cranial PIFM.	O: Aponeurosis from the cranial 2/3 of the ischium, pubis, and ischiopubic fenestra. I: Distal posterior femoral shaft.
MA	O: Cranial 1/3 of the ventral ischium and the ischiopubic fenestra. I: Distal 1/2 of the posterior femoral shaft. Notes: Strap-like muscle superficial to caudal PIFM.	O: Aponeurosis from the entire ischium, pubis, and ischiopubic fenestra. I: Distal posterior femoral shaft.
CG	O: Cranial 1/3 of the ventral ischium and the ischiopubic fenestra. I: Distal 1/3 of the posterior femoral shaft. Notes: Strap-like muscle superficial to caudal PIFM.	O: Aponeurosis from the entire ischium, pubis, and ischiopubic fenestra. I: Distal 1/3 of the posterior femoral shaft.
MS	O: Cranial 1/3 of the ventral ischium and the ischiopubic fenestra. I: Distal 1/4 of the posterior femoral shaft and intercondylar region. Notes: Strap-like muscle superficial to cranial PIFM.	O: Aponeurosis from the entire ischium, pubis, and ischiopubic fenestra. I: Distal 1/4 of the posterior femoral shaft and intercondylar region.
DCC	O: Ventral ischium and ischiopubic fenestra caudal to acetabulum at 1/3 the ischium's length. I: Distal posterior femoral shaft and intercondylar region. Notes: Strap-like muscle superficial to cranial PIFM.	O: Aponeurosis from the central ischium, pubis, and ischiopubic fenestra. I: Intercondylar region of the femur.
WG	O: Ventral ischium and ischiopubic fenestra. I: Distal posterior femoral shaft and intercondylar region. Notes: Strap-like muscle superficial to caudal PIFM.	O: Aponeurosis from the cranial ischium, pubis, and ischiopubic fenestra. I: Intercondylar region of the femur.
RTL	O: Entire length of the ventral ischium, the ischiopubic fenestra, and the pubis. I: Most distal posterior femoral shaft and intercondylar region. Notes: Fused into single muscle mass with PIFM.	Fused with PIFL.
CL	O: Entire length of the ventral ischium, the ischiopubic fenestra, and the pubis. I: Most distal posterior femoral shaft and intercondylar region. Notes: Fused into single muscle mass with PIFM.	Fused with PIFL.

Table 2.3 – continued from previous page

	AM	IFI
GF	O: Tendinous. Pectineal process of the pubis. I: Tendinous. Common digital flexor tendon.	O: Ilium ventral to ITM. I: Proximal medial femoral shaft.
MA	O: Tendinous. Pectineal process of the pubis. I: Tendinous. Common digital flexor tendon.	O: Cranial, ventral portion of the postacetabular ilium. I: Proximal medial femoral shaft.
CG	O: Tendinous. Pectineal process of the pubis. I: Tendinous. Common digital flexor tendon.	O: Cranial, ventral portion of the postacetabular ilium. I: Proximal medial femoral shaft.
MS	O: Tendinous. Pectineal process of the pubis. I: Tendinous. Common digital flexor tendon.	O: Cranial, ventral portion of the postacetabular ilium. I: Proximal medial femoral shaft.
DCC	O: Tendinous. Pectineal process of the pubis. I: Tendinous. Common digital flexor tendon.	O: Cranial, ventral portion of the postacetabular ilium. I: Proximal medial femoral shaft.
WG	Absent.	O: Cranial, ventral portion of the postacetabular ilium. I: Proximal medial femoral shaft.
RTL	O: Tendinous. Pectineal process of the pubis. I: Tendinous. Common digital flexor tendon.	O: Ventral caudal preacetabular ilium. I: Tubercle on medial femoral neck. Notes: Muscle strongly developed.
CL	O: Tendinous. Pectineal process of the pubis. I: Tendinous. Common digital flexor tendon.	O: Ventral caudal preacetabular ilium. I: I: Tubercle on medial femoral neck. Notes: Muscle strongly developed.
Notes	Insertion tendon dives under the GM, along a groove in the patella, and through the patellar tendon to fuse with the common digital flexor tendon.	

Table 2.4: Limb musculature origins and insertions. This table shows the origin and insertion of major pelvic muscles dissected in the helmeted guineafowl (GF), mallard (MA), Canada goose (CG), mute swan (MS), double-crested cormorant (DCC), Western grebe (WG), red-throated loon (RTL), and common loon (CL). Attachment points are fleshy unless otherwise noted. GF do not swim. MA, CG, and MS are surface-swimmers of increasing body mass. DCC, WG, RTL, and CL are divers, with the DCC representing an intermediate specialization since it retains the ability to walk. A key for muscle abbreviations can be found in Tables 2.1 and 2.2.

	FTE
GF	O: Posterolateral shaft of the femur over most of its length. I: Aponeurosis to the patella. Posterior tendon to the lateral condyle of the tibiotarsus.
MA	O: Posterolateral shaft of the femur over most of its length. I: Aponeurosis to the patella. Posterior tendon to the lateral cnemial crest and SFPPDII.
CG	O: Posterolateral shaft of the femur over most of its length. I: Aponeurosis to the patella. Posterior tendon to the lateral cnemial crest and SFPPDII.
MS	O: Posterolateral shaft of the femur over most of its length. I: Aponeurosis to the patella. Posterior tendon to the lateral cnemial crest and SFPPDII.
DCC	O: Posterolateral shaft of the femur over most of its length. I: Aponeurosis to the patella. Posterior tendon to the lateral cnemial crest and SFPPDII.
WG	O: Posterolateral shaft of the femur over most of its length. I: Fleshy to lateral cnemial crest and distal, lateral patella.
RTL	O: Posterolateral shaft of the femur over most of its length. I: Aponeurosis to the distal, lateral cnemial crest.
CL	O: Posterolateral shaft of the femur over most of its length. I: Aponeurosis to the distal, lateral cnemial crest.

Table 2.4 – continued from previous page

	FTM	FTI
GF	O: Anterior and anterolateral femoral shaft. I: Aponeurosis and fleshy to the patella.	O: Medial femoral shaft. I: Tendinous. Medial cnemial crest.
MA	O: Anterior femoral shaft and neck of the femur. I: Aponeurosis and fleshy to the patella.	O: Medial femoral shaft. I: Tendinous. Medial cnemial crest.
CG	O: Anterior femoral shaft and neck of the femur. I: Aponeurosis and fleshy to the patella.	O: Medial femoral shaft. I: Tendinous. Medial cnemial crest.
MS	O: Anterior and proximal, lateral femoral shaft. I: Aponeurosis and fleshy to the patella.	O: Medial femoral shaft. I: Tendinous. Medial cnemial crest.
DCC	O: Anterior femoral shaft. I: Aponeurosis and fleshy to dorsal patella.	O: Medial femoral shaft. I: Tendinous. Medial cnemial crest.
WG	O: Anterior femoral shaft. I: Entire posterior surface of the patella. Notes: Much larger than FTE and FTI.	O: Medial femoral shaft. I: Medial cnemial crest.
RTL	O: Anterior femoral shaft. I: Entire posterior cnemial crest. Notes: Much larger than FTE and FTI.	O: Medial femoral shaft. I: Distal medial cnemial crest.
CL	O: Anterior femoral shaft. I: Entire posterior cnemial crest. Notes: Much larger than FTE and FTI.	O: Medial femoral shaft. I: Distal medial cnemial crest.

Table 2.4 – continued from previous page

	FL
GF	O: Lateral cnemial crest and lateral patellar tendon. Connections to TC, SFPPDIII, and SFPPDII. I: Tendinous. Anterior tendon fuses with tendon of FPDIII. Posterior tendon inserts at proximal, lateral tibial cartilage.
MA	O: Lateral cnemial crest and lateral patellar tendon. Connections to TC, SFPPDIII, and SFPPDII. I: Tendinous. Anterior tendon fuses with tendon of FPDIII. Posterior tendon inserts at proximal, lateral tibial cartilage.
CG	O: Lateral cnemial crest and lateral patellar tendon. Connections to TC, SFPPDIII, and SFPPDII. I: Tendinous. Anterior tendon fuses with tendon of FPDIII. Posterior tendon inserts at proximal, lateral tibial cartilage.
MS	O: Lateral cnemial crest and lateral patellar tendon. Connections to TC, SFPPDIII, and SFPPDII. I: Tendinous. Anterior tendon fuses with tendon of FPDIII. Posterior tendon inserts at proximal, lateral tibial cartilage.
DCC	O: Tendinous from lateral cnemial crest and anterolateral proximal tibial shaft. Fleshy from the lateral fibula. Connections to TC, SFPPDIII and SFPPDII. I: Tendinous. Anterior tendon fuses with tendon of FPDIII. Posterior tendon inserts at proximal, lateral tibial cartilage.
WG	O: Tendinous from anteromedial cnemial crest. Fleshy from the lateral fibular shaft. Connections to TC, SFPPDIII and SFPPDII. I: Tendinous. Proximal, lateral tibial cartilage.
RTL	O: Anterior cnemial crest and lateral fibular shaft. Connections to TC, SFPPDIII and SFPPDII. I: Tendinous. Proximal, lateral tibial cartilage. Small slip to FPDIII tendon.
CL	O: Anterior cnemial crest and lateral fibular shaft. Connections to TC, SFPPDIII and SFPPDII. I: Tendinous. Proximal, lateral tibial cartilage. Small slip to FPDIII tendon.

55

Table 2.4 – continued from previous page

	TC
GF	O: Large head from anterolateral cnemial crest and anterior patellar tendon. Tendinous small head from anterolateral femoral condyle inside knee joint. I: Dorsal surface of proximal tarsometatarsus.
MA	O: Large head from anterolateral cnemial crest, anterior patellar tendon, and proximal anterior tibiotarsus. Tendinous small head from anterolateral femoral condyle inside knee joint. I: Dorsal surface of proximal tarsometatarsus.
CG	O: Large head from anterolateral cnemial crest, anterior patellar tendon, and proximal anterior tibiotarsus. Tendinous small head from anterolateral femoral condyle inside knee joint. I: Dorsal surface of proximal tarsometatarsus.
MS	O: Large head from anterolateral cnemial crest, anterior patellar tendon, and proximal anterior tibiotarsus. Tendinous small head from anterolateral femoral condyle inside knee joint. I: Dorsal surface of proximal tarsometatarsus.
DCC	O: Large head from anterolateral cnemial crest, anterior patellar tendon, and proximal anterior tibiotarsus. Tendinous small head from anterolateral femoral condyle inside knee joint. I: Dorsal surface of proximal tarsometatarsus.
WG	O: Large head from anterolateral cnemial crest and patella. Small head from anterior tibiotarsus and tendinous to anterolateral femoral condyle inside knee joint. I: Dorsal surface of proximal tarsometatarsus. Notes: Insertion tendon is partially calcified.
RTL	O: Large head from anterolateral cnemial crest. Tendinous small head from anterolateral femoral condyle inside knee joint. I: Dorsal surface of proximal tarsometatarsus.
CL	O: Large head from anterolateral cnemial crest. Tendinous small head from anterolateral femoral condyle inside knee joint. I: Dorsal surface of proximal tarsometatarsus.
Notes	Insertion tendon goes through retinaculum at intertarsal ankle joint.

Table 2.4 – continued from previous page

	EDL	FB
GF	O: Anteromedial cnemial crest and proximal tibiotarsus. I: Tendinous. Ungual phalanx of digits II-IV, with slips to proximal phalanges.	O: Lateral tibiotarsus shaft and anterior fibular shaft. I: Tendinous. Most proximal, lateral hypotarsus.
MA	O: Anteromedial cnemial crest and proximal tibiotarsus. I: Tendinous. Ungual phalanx of digits II-IV, with slips to proximal phalanges.	O: Distal anteriolateral fibula. I: Tendinous. Most proximal, lateral hypotarsus.
CG	O: Anteromedial cnemial crest and proximal tibiotarsus. I: Tendinous. Ungual phalanx of digits II-IV, with slips to proximal phalanges.	O: Distal anteriolateral fibula. I: Tendinous. Most proximal, lateral hypotarsus.
MS	O: Anteromedial cnemial crest and proximal tibiotarsus. I: Tendinous. Ungual phalanx of digits II-IV, with slips to proximal phalanges.	O: Distal lateral tibiotarsus and anterior fibula. I: Tendinous. Most proximal, lateral hypotarsus.
DCC	O: Anteromedial cnemial crest and proximal tibiotarsus. I: Tendinous. Ungual phalanx of digits II-IV, with slips to proximal phalanges.	O: Distal lateral tibiotarsus and anterior fibula. I: Tendinous. Most proximal, lateral hypotarsus.
WG	O: Anteromedial cnemial crest and proximal tibiotarsus. I: Tendinous. Ungual phalanx of digits II-IV, with slips to proximal phalanges.	Absent.
RTL	O: Anteromedial cnemial crest and proximal tibiotarsus. I: Tendinous. Ungual phalanx of digits II-IV, with slips to proximal phalanges.	O: Distal lateral tibiotarsus and anterior fibula. I: Tendinous. Most proximal, lateral hypotarsus.
CL	O: Anteromedial cnemial crest and proximal tibiotarsus. I: Tendinous. Ungual phalanx of digits II-IV, with slips to proximal phalanges.	O: Distal lateral tibiotarsus and anterior fibula. I: Tendinous. Most proximal, lateral hypotarsus.
Notes	Tendon travels through retinaculum and bony canal on anterior distal tibiotarsus.	

Table 2.4 – continued from previous page

	GM	GI
GF	O: Anteromedial patella, medial cnemial crest, proximal tibial shaft. With connections to FL. I: Tendinous. Aponeurosis combines with that of GL to form common calcaneal tendon to the hypotarsus.	O: Posterior intercondylar region of the femur immediately distal to FCLA insertion. I: Tendinous. Fibers insert onto the combined GL/GM aponeurosis, which becomes the calcaneal tendon to the hypotarsus.
MA	O: Anteromedial patella, medial cnemial crest, proximal tibial shaft. With connections to FL. I: Tendinous. Fuses with GI tendon then GL tendon to the hypotarsus.	O: Medial surface of medial femoral condyle. I: Tendinous. Fuses with GM tendon, then the GL tendon. Inserts onto the hypotarsus.
CG	O: Anteromedial patella, medial cnemial crest, proximal tibial shaft. With connections to FL. I: Tendinous. Fuses with GI tendon then GL tendon to the hypotarsus.	O: Medial surface of medial femoral condyle. I: Tendinous. Fuses with GM tendon, then the GL tendon. Inserts onto the hypotarsus.
MS	O: Anteromedial patella, medial cnemial crest, proximal tibial shaft. With connections to FL. I: Tendinous. Fuses with GI tendon then GL tendon to the hypotarsus.	O: Medial surface of medial femoral condyle. I: Tendinous. Fuses with GM tendon, then the GL tendon. Inserts onto the hypotarsus.
DCC	O: Anteromedial patella, medial cnemial crest, proximal tibial shaft. With connections to FL. I: Tendinous. Fuses with GI tendon then GL tendon to the hypotarsus.	O: Medial surface of medial femoral condyle and proximal posteromedial tibial shaft. I: Fibers fuse with GM.
WG	O: Anteromedial cnemial crest, proximal 1/2 of medial tibiotarsus, and proximal tip of the posterior patella. I: Tendinous. Fuses with GI tendon then GL tendon to the hypotarsus.	O: Medial surface of medial femoral condyle and proximal posteromedial tibial shaft. I: Tendinous. Fuses with GM tendon, then the GL tendon. Inserts onto the hypotarsus.
RTL	O: Anteromedial cnemial crest and proximal tibial shaft. I: Tendinous. Fuses with GI tendon then GL tendon to the hypotarsus.	O: Medial surface of medial femoral condyle and proximal posteromedial tibial shaft. I: Tendinous. Fuses with GM tendon, then the GL tendon. Inserts onto the hypotarsus.
CL	O: Anteromedial cnemial crest and proximal tibial shaft. I: Tendinous. Fuses with GI tendon then GL tendon to the hypotarsus.	O: Medial surface of medial femoral condyle and proximal posteromedial tibial shaft. I: Tendinous. Fuses with GM tendon, then the GL tendon. Inserts onto the hypotarsus.

Table 2.4 – continued from previous page

	GL	SFPPDII
GF	O: Distal, posterolateral femoral shaft. I: Tendinous. Aponeurosis combines with that of GM to form common calcaneal tendon to the hypotarsus.	O: Lateral femoral condyle. Connections to SFPPDIII and FL. I: Tendinous. Distal basal phalanx and proximal phalanx 2 of digit II.
MA	O: Tendinous. Distal, posterolateral femoral shaft. I: Tendinous. Fuses with GM/GI tendon to the hypotarsus.	O: One head from lateral femoral condyle. Other head from lateral cnemial crest. Connections to SFPPDIII and FL. I: Tendinous. Distal basal phalanx and proximal phalanx 2 of digit II.
CG	O: Tendinous. Distal, posterolateral femoral shaft. I: Tendinous. Fuses with GM/GI tendon to the hypotarsus.	O: One head from lateral femoral condyle. Other head from lateral cnemial crest. Connections to SFPPDIII and FL. I: Tendinous. Distal basal phalanx and proximal phalanx 2 of digit II.
MS	O: Tendinous. Distal, posterolateral femoral shaft. I: Tendinous. Fuses with GM/GI tendon to the hypotarsus.	O: One head from lateral femoral condyle. Other head from lateral cnemial crest. Connections to SFPPDIII and FL. I: Tendinous. Distal basal phalanx and proximal phalanx 2 of digit II.
DCC	O: Tendinous and fleshy. Distal, posterolateral femoral shaft. I: Tendinous. Fuses with GM/GI tendon to the hypotarsus.	O: Lateral femoral condyle, lateral femoral shaft just proximal to the condyle. Connections to SFPPDIII and FL. I: Tendinous. Distal basal phalanx and proximal phalanx 2 of digit II.
WG	O: Distal, posterolateral femoral shaft. I: Tendinous. Fuses with GM/GI tendon to the hypotarsus.	O: Lateral femoral condyle and lateral femoral shaft just proximal to the condyle. Connections to SFPPDIII and FL. I: Tendinous. Distal basal phalanx and proximal phalanx 2 of digit II. Notes: Calcified tendon.
RTL	O: Aponeurosis and fleshy. Distal 2/3 of posterolateral femoral shaft and lateral cnemial crest. I: Tendinous. Fuses with GM/GI tendon to the hypotarsus.	O: One head from lateral femoral condyle. Other head from anterolateral cnemial crest with connections to SFPPDIII and FL. I: Tendinous. Distal basal phalanx and proximal phalanx 2 of digit II. Notes: Tendon goes through bony canal in hypotarsus.
CL	O: Aponeurosis and fleshy. Distal 2/3 of posterolateral femoral shaft. I: Tendinous. Fuses with GM/GI tendon to the hypotarsus.	O: One head from lateral femoral condyle. Other head from anterolateral cnemial crest with connections to SFPPDIII and FL. I: Tendinous. Distal basal phalanx and proximal phalanx 2 of digit II. Notes: Tendon goes through bony canal in hypotarsus.

Table 2.4 – continued from previous page

	SFPPDIII
GF	O: Lateral femoral condyle, lateral cnemial crest, and patellar tendon. Connections to FL and FPDIII. I: Tendinous. Distal phalanx 2 and proximal phalanx 3 of digit III.
MA	O: Lateral femoral condyle, lateral cnemial crest, lateral fibula, and the common digital flexor tendon. I: Tendinous. Distal phalanx 2 and proximal phalanx 3 of digit III.
CG	O: Lateral femoral condyle, lateral cnemial crest, lateral fibula, and the common digital flexor tendon. I: Tendinous. Distal phalanx 2 and proximal phalanx 3 of digit III.
MS	O: Lateral femoral condyle, lateral cnemial crest, lateral patella, lateral fibula, and the common digital flexor tendon. Connection to FL. I: Tendinous. Distal phalanx 2 and proximal phalanx 3 of digit III.
DCC	O: Lateral femoral condyle, lateral cnemial crest, lateral patella, lateral fibula, and the common digital flexor tendon. Connection to FL. I: Tendinous. Distal phalanx 2 and proximal phalanx 3 of digit III.
WG	O: Lateral femoral condyle, lateral cnemial crest, lateral patella, lateral fibula, and the common digital flexor tendon. Connection to FL. I: Tendinous. Distal phalanx 2 and proximal phalanx 3 of digit III. Notes: Calcified tendon.
RTL	O: Lateral femoral condyle, lateral cnemial crest, lateral fibula, and the common digital flexor tendon. Connection to FL. I: Tendinous. Distal phalanx 2 and proximal phalanx 3 of digit III. Notes: Tendon goes through bony canal in hypotarsus.
CL	O: Lateral femoral condyle, lateral cnemial crest, lateral fibula, and the common digital flexor tendon. Connection to FL. I: Tendinous. Distal phalanx 2 and proximal phalanx 3 of digit III. Notes: Tendon goes through bony canal in hypotarsus.

Table 2.4 – continued from previous page

	SFPPDIV
GF	O: Larger posteromedial head from the intercondylar region of the femur and the ansa fibularis. Smaller anterolateral head tendinous from common digital flexor tendon.
	I: Tendinous. Proximal phalanx 4 of digit IV with slips to proximal interphalangeal joints.
MA	O: Larger posteromedial head from the intercondylar region of the femur, distal posterior femoral shaft, and the ansa fibularis. Smaller anterolateral head tendinous from common digital flexor tendon.
	I: Tendinous. Proximal phalanx 4 of digit IV with slips to proximal interphalangeal joints.
CG	O: Larger posteromedial head from the intercondylar region of the femur, distal posterior femoral shaft, and the ansa fibularis. Smaller anterolateral head tendinous from common digital flexor tendon.
	I: Tendinous. Proximal phalanx 4 of digit IV with slips to proximal interphalangeal joints.
MS	O: Larger posteromedial head from the intercondylar region of the femur, distal posterior femoral shaft, and the ansa fibularis. Smaller anterolateral head tendinous from common digital flexor tendon.
	I: Tendinous. Proximal phalanx 4 of digit IV with slips to proximal interphalangeal joints.
DCC	O: Larger posteromedial head from the distal posterior femoral shaft and the ansa fibularis. Smaller anterolateral head tendinous from common digital flexor tendon.
	I: Tendinous. Proximal phalanx 4 of digit IV with slips to proximal interphalangeal joints.
WG	O: Large ahead from the distal posterior femoral shaft and the ansa fibularis.
	I: Tendinous. Proximal phalanx 3 of digit IV with slips to proximal interphalangeal joints.
	Notes: Calcified tendon.
RTL	O: Large head from the distal 1/2 of posterior femoral shaft, the ansa fibularis, and FPDIII medial head tendon.
	I: Tendinous. Proximal phalanx 2 of digit IV with slips to proximal interphalangeal joints.
	Notes: Tendon goes through bony canal in hypotarsus.
CL	O: Large head from the distal 1/2 of posterior femoral shaft, the ansa fibularis, and FPDIII medial head tendon.
	I: Tendinous. Proximal phalanx 2 of digit IV with slips to proximal interphalangeal joints.
	Notes: Tendon goes through bony canal in hypotarsus.

Table 2.4 – continued from previous page

	FPDII
GF	O: Medial head joins FPDIII tendon to most medial part of the intercondylar region of the femur. Lateral head tendinous from the common digital flexor tendon.
	I: Proximal basal phalanx (1) of digit II.
	Notes: Tendon goes through connective tissue canal in hypotarsus.
MA	O: Medial head joins FPDIII tendon to most medial part of the intercondylar region of the femur. Lateral head tendinous from the common digital flexor tendon.
	I: Proximal basal phalanx (1) of digit II.
	Notes: Tendon goes through connective tissue canal in hypotarsus.
CG	O: Medial head joins FPDIII tendon to most medial part of the intercondylar region of the femur. Lateral head tendinous from the common digital flexor tendon.
	I: Proximal basal phalanx (1) of digit II.
	Notes: Tendon goes through connective tissue canal in hypotarsus.
MS	O: Medial head joins FPDIII tendon to most medial part of the intercondylar region of the femur. Lateral head tendinous from the common digital flexor tendon.
	I: Proximal basal phalanx (1) of digit II.
	Notes: Tendon goes through connective tissue canal in hypotarsus.
DCC	O: Medial head fleshy from lateral intercondylar region of femur. Lateral head tendinous from the common digital flexor tendon.
	I: Proximal basal phalanx (1) of digit II.
	Notes: Tendon goes through connective tissue canal in hypotarsus.
WG	Absent.
RTL	O: Medial head fleshy from distal, posterior femoral shaft and FPDIII tendon. Lateral head tendinous from the common digital flexor tendon.
	I: Proximal basal phalanx (1) of digit II.
	Notes: Tendon goes through bony canal in hypotarsus.
CL	O: Medial head fleshy from distal, posterior femoral shaft and FPDIII tendon. Lateral head tendinous from the common digital flexor tendon.
	I: Proximal basal phalanx (1) of digit II.
	Notes: Tendon goes through bony canal in hypotarsus.

Table 2.4 – continued from previous page

	FPDIII
GF	O: Medial head tendinous from the medial intercondylar region of the femur. Lateral head tendinous from the common digital flexor tendon.
	I: Tendinous. Distal basal phalanx (1) and proximal phalanx 2 of digit III.
MA	O: Medial head tendinous from the medial intercondylar region of the femur. Lateral head tendinous from the common digital flexor tendon.
	I: Tendinous. Distal basal phalanx (1) and proximal phalanx 2 of digit III.
CG	O: Medial head tendinous from the medial intercondylar region of the femur. Lateral head tendinous from the common digital flexor tendon.
	I: Tendinous. Distal basal phalanx (1) and proximal phalanx 2 of digit III.
MS	O: Medial head tendinous from the medial intercondylar region of the femur. Lateral head tendinous from the common digital flexor tendon.
	I: Tendinous. Distal basal phalanx (1) and proximal phalanx 2 of digit III.
DCC	O: Medial head tendinous from the medial intercondylar region of the femur. Lateral head tendinous from the common digital flexor tendon.
	I: Tendinous. Distal basal phalanx (1) and proximal phalanx 2 of digit III.
WG	O: Medial head tendinous from the medial intercondylar region of the femur. Lateral head tendinous from the common digital flexor tendon.
	I: Tendinous. Distal basal phalanx (1) and proximal phalanx 2 of digit III.
	Notes: Medial head tendon calcified.
RTL	O: Medial head tendinous from the posterior femoral shaft 1/2 down its length. Lateral head tendinous from the common digital flexor tendon.
	I: Tendinous. Distal basal phalanx (1) and proximal phalanx 2 of digit III.
	Notes: Muscle body short with long broad medial head tendon. Insertion tendon goes though a bony canal in the hypotarsus.
CL	O: Medial head tendinous from the posterior femoral shaft 1/2 down its length. Lateral head tendinous from the common digital flexor tendon.
	I: Tendinous. Distal basal phalanx (1) and proximal phalanx 2 of digit III.
	Notes: Muscle body short with long broad medial head tendon. Insertion tendon goes though a bony canal in the hypotarsus.

Table 2.4 – continued from previous page

	FHL	FDL
GF	O: Lateral intercondylar region of the femur. I: Tendon fuses with FDL tendon along TMT then splits to insert on ungual phalanx (1) of digit I (hallux).	O: One head to posterior tibial shaft. Other head to posterolateral fibula. I: Tendon fuses with FHL tendon along TMT then splits into 3 parts to insert on ungual phalanges of digits II-IV.
MA	O: Lateral intercondylar region of the femur. I: Tendon fuses with FDL tendon along TMT then splits to insert on ungual phalanx (1) of digit I (hallux).	O: One head to posterior tibial shaft. Other head to posterolateral fibula. I: Tendon fuses with FHL tendon along TMT then splits into 3 parts to insert on ungual phalanges of digits II-IV.
CG	O: Lateral intercondylar region of the femur. I: Tendon fuses with FDL tendon along TMT then splits to insert on ungual phalanx (1) of digit I (hallux).	O: One head to posterior tibial shaft. Other head to posterolateral fibula. I: Tendon fuses with FHL tendon along TMT then splits into 3 parts to insert on ungual phalanges of digits II-IV.
MS	O: Lateral intercondylar region of the femur. I: Tendon fuses with FDL tendon along TMT then splits to insert on ungual phalanx (1) of digit I (hallux).	O: One head to posterior tibial shaft. Other head to posterolateral fibula. I: Tendon fuses with FHL tendon along TMT then splits into 3 parts to insert on ungual phalanges of digits II-IV.
DCC	O: Lateral intercondylar region of the femur. I: Tendon fuses with FDL tendon along TMT then splits to insert on ungual phalanx (1) of digit I (hallux).	O: One head to posterior tibial shaft. Other head to posterolateral fibula. I: Tendon fuses with FHL tendon along TMT then splits into 3 parts to insert on ungual phalanges of digits II-IV.
WG	O: Lateral intercondylar region of the femur. I: Tendon fuses with FDL tendon along TMT.	O: One head to posterior tibial shaft. Other head to posterolateral fibula. I: Tendon fuses with FHL tendon along TMT then splits into 3 parts to insert on ungual phalanges of digits II-IV.
RTL	O: Lateral intercondylar region of the femur. I: Tendon fuses with FDL tendon along TMT.	O: One head to posterior tibial shaft. Other head to posterolateral fibula. I: Tendon fuses with FHL tendon along TMT then splits into 3 parts to insert on ungual phalanges of digits II-IV.
CL	O: Lateral intercondylar region of the femur. I: Tendon fuses with FDL tendon along TMT.	O: One head to posterior tibial shaft. Other head to posterolateral fibula. I: Tendon fuses with FHL tendon along TMT then splits into 3 parts to insert on ungual phalanges of digits II-IV.
Notes	Tendon calcified along TBT. Tendon goes through bony canal in hypotarsus.	Tendon goes through deep bony canal in hypotarsus. Tendon calcified along TMT.

Table 2.4 – continued from previous page

	PL	PO
GF	O: Medial tibial condyle and most proximal, posterior tibial shaft. I: Tendinous. Proximal, medial tibial cartilage.	O: Proximal, posterior tibial shaft and intercondylar region. I: Posteromedial fibular head and proximal shaft.
MA	O: Medial tibial condyle and most proximal, posterior tibial shaft. I: Tendinous. Proximal, medial tibial cartilage.	O: Proximal, posterior tibial shaft and intercondylar region. I: Posteromedial fibular head and proximal shaft.
CG	O: Medial tibial condyle and most proximal, posterior tibial shaft. I: Tendinous. Proximal, medial tibial cartilage.	O: Proximal, posterior tibial shaft and intercondylar region. I: Posteromedial fibular head and proximal shaft.
MS	O: Medial tibial condyle and most proximal, posterior tibial shaft. I: Tendinous. Proximal, medial tibial cartilage.	O: Proximal, posterior tibial shaft and intercondylar region. I: Posteromedial fibular head and proximal shaft.
DCC	O: Medial tibial condyle and most proximal, posterior tibial shaft. I: Tendinous. Proximal, medial tibial cartilage.	O: Proximal, posterior tibial shaft and intercondylar region. I: Posteromedial fibular head and proximal shaft.
WG	O: Medial tibial condyle and most proximal, posterior tibial shaft. I: Tendinous. Proximal, medial tibial cartilage.	O: Proximal, posterior tibial shaft and intercondylar region. I: Posteromedial fibular head and proximal shaft.
RTL	O: Medial tibial condyle and most proximal, posterior tibial shaft. I: Tendinous. Proximal, medial tibial cartilage.	O: Proximal, posterior tibial shaft and intercondylar region. I: Posteromedial fibular head and proximal shaft.
CL	O: Medial tibial condyle and most proximal, posterior tibial shaft. I: Tendinous. Proximal, medial tibial cartilage.	O: Proximal, posterior tibial shaft and intercondylar region. I: Posteromedial fibular head and proximal shaft.

2.6 References

Abourachid, A. (2000). Bipedal locomotion in birds: the importance of functional parameters in terrestrial adaptation in Anatidae. Can. J. Zool. 78, 1994-1998.

Abourachid, A. (2001). Kinematic parameters of terrestrial locomotion in cursorial (ratites), swimming (ducks), and striding birds (quail and guinea fowl). Comp. Biochem. Physiol. A. Mol. Integr. Physiol. 131, 113-119.

Baumel, J. and Witmer, L. M. (1993). Handbook of avian anatomy: nomina anatomica avium. (ed. Baumel, J., King, A. S., Breazile, J. E., Evans, H. E., and Vanden Berge, J. C.) Cambridge, MA: Nuttall Ornithological Club.

Beddard, F. (1896). On the Anatomy of a Grebe (*Aechmophorus major*), with Remarks upon the Classification of some of the Schizognathous Birds. Proc. Zool. Soc. London.

Bennett, M. (1996). Allometry of the leg muscles of birds. J. Zool. 238, 435-443.

Biewener, A. A. and Corning, W. R. (2001). Dynamics of mallard (*Anas platyrhynchos*) gastrocnemius function during swimming versus terrestrial locomotion. J. Exp. Biol. 204, 1745-1756.

Birn-Jeffrey, A. V, Hubicki, C. M., Blum, Y., Renjewski, D., Hurst, J. W. and Daley, M. A. (2014). Don't break a leg: running birds from quail to ostrich prioritize leg safety and economy on uneven terrain. J. Exp. Biol. 217, 3786-3796.

Butler, P. J. (2004). Metabolic regulation in diving birds and mammals. Respir. Physiol. Neurobiol. 141, 297-315.

Carr, J. A. (2008). Muscle function during swimming and running in aquatic, semi-aquatic and cursorial birds.

Clifton, G. T., Hedrick, T. L. and Biewener, A. A. (2015). Western and Clark's grebes use novel strategies for run-

ning on water. J. Exp. Biol. 218, 1235-1243.

Doube, M., Yen, S. C. W., K?osowski, M. M., Farke, A. A., Hutchinson, J. R. and Shefelbine, S. J. (2012). Whole-bone scaling of the avian pelvic limb. J. Anat. 221, 21-29.

Ellerby, D. J. and Marsh, R. L. (2010). The mechanical function of linked muscles in the guinea fowl hind limb. J. Exp. Biol. 213, 2201-8.

Ellerby, D. J., Henry, H. T., Carr, J. A., Buchanan, C. I. and Marsh, R. L. (2005). Blood flow in guinea fowl *Numida meleagris* as an indicator of energy expenditure by individual muscles during walking and running. J. Physiol. 564, 631-648.

Fish, F. E. (1993). Influence of Hydrodynamic Design and Propulsive Mode on Mammalian Swimming Energetics. Aust. J. Zool. 42, 79-101.

Forbes, W. A. (1885). The Collected Scientific Papers of the Late William Alexander Forbes. (ed. Beddard, F. and Sclater, P.) London, UK: Taylor and Francis.

Gadow, H. and Selenka, E. (1891). Aves. In Dr. H.G. Bronn's Klassen und Ordnungen des Thier-Reiches, in Wort und Bild, Leipzig und Heidelberg.

Garrod, A. H. (1873). On certain muscles of birds and their value in classification. Part I. Proc. Zool. Soc. London 41, 626-644.

Garrod, A. H. (1874). On certain muscles of birds and their value in classification. Part II. Proc. Zool. Soc. London 42, 111-123.

Garrod, A. H. (1875). On the disposition of the deep plantar tendons in different birds. Proc. Zool. Soc. London

339-348.

Garrod, A. H. and Darwin, F. (1872). Notes on an ostrich lately living in the Society's collection. Proc. Zool. Soc. London 356-363.

Gatesy, S. M. (1994). Neuromuscular Diversity in Archosaur Deep Dorsal Thigh Muscles. Brain. Behav. Evol. 43, 1-14.

Gatesy, S. M. (1999). Guineafowl hind limb function. II: Electromyographic analysis and motor pattern evolution. J. Morphol. 240, 127-142.

George, J. C. and Berger, A. J. (1966). Avian myology. New York: Academic Press.

Haughton, S. (1865). Notes on animal mechanics. No III: On the muscular mechanism of the leg of the ostrich. Proc. R. Irish Acad. 9, 50-61.

Hertel, F. and Campbell Jr, K. E. (2007). The antitrochanter of birds: form and function in balance. Auk 124, 789-805.

Hinić-Frlog, S. and Motani, R. (2010). Relationship between osteology and aquatic locomotion in birds: determining modes of locomotion in extinct Ornithurae. J. Evol. Biol. 23, 372-85.

Hudson, G. (1937). Studies on the Muscles of the Pelvic Appendage in Birds. Am. Midl. Nat. 18, 1-108.

Hudson, G., Lanzillotti, P. and Edwards, G. (1959). Muscles of the Pelvic Limb in Galliform Birds. Am. Midl. Nat. 61, 1-67.

Hutchinson, J. R. (2002). The evolution of hindlimb tendons and muscles on the line to crown-group birds.

Comp. Biochem. Physiol. Part A Mol. Integr. Physiol. 133, 1051-1086.

Johansson, L. and Norberg, U. M. (2001). Lift-based paddling in diving grebe. J. Exp. Biol. 204, 1687-96.

Johnsgard, P. A. (1987). Diving Birds of North America. Lincoln, Nebraska: University of Nebraska Press.

Landis, W. J. and Silver, F. H. (2002). The structure and function of normally mineralizing avian tendons. Comp. Biochem. Physiol. A. Mol. Integr. Physiol. 133, 1135-57.

Mayr, G. (2016). Variations in the hypotarsus morphology of birds and their evolutionary significance. Acta Zool. 97, 196-210.

McMahon, T. A. (1984). Muscles, reflexes, and locomotion. Princeton University Press.

Owre, O. T. (1967). Locomoton and feeding in the anhinga and the double-crested cormorant. Ornithol. Monogr. 6, 1-138.

Pennycuick, C. J., Klaassen, M., Kvist, A. and Lindström, Å. (1996). Wingbeat frequency and the body drag anomaly: wind-tunnel observations on a thrush nightingale (*Luscinia luscinia*) and a teal (*Anas crecca*). J. Exp. Biol. 199, 2757-2765.

Provini, P., Goupil, P., Hugel, V. and Abourachid, A. (2012). Walking, Paddling, Waddling: 3D Kinematics Anatidae Locomotion (*Callonetta leucophrys*). J. Exp. Zool. 317, 275-282.

Prum, R. O., Berv, J. S., Dornburg, A., Field, D. J., Townsend, J. P., Lemmon, E. M. and Lemmon, A. R. (2015). A comprehensive phylogeny of birds (Aves) using targeted next-generation DNA sequencing. Nature 526, 569-573.

Raikow, R. J. (1973). Locomotor Mechanisms in North American Ducks. Wilson Bull. 85, 295-307.

Raikow, R. J. (1985). Locomotor system. In Form and function in birds (ed. King, A.) and McLelland, J.), pp. 57-147. Academic Press.

Raikow, R. J. (1987). Hindlimb myology and evolution of the Old World suboscine passerine birds (Acanthisittidae, Pittidae, Philepittidae, Eurylaimidae). Ornithol. Monogr. 41, iii-81.

Ribak, G. and Swallow, J. (2010). Drag-based □hovering□ in ducks: the hydrodynamics and energetic cost of bottom feeding. PLoS One 5, 1-11.

Ribak, G., Weihs, D. and Arad, Z. (2004). How do cormorants counter buoyancy during submerged swimming? J. Exp. Biol. 207, 2101-2114.

Roberts, T. J., Chen, M. S. and Taylor, C. R. (1998). Energetics of bipedal running II: Limb design and running mechanics. J. Exp. Biol. 201, 2753-2762.

Rodewald, P. ed. (2015). The Birds of North America. Ithaca, NY: Cornell Laboratory of Ornithology.

Rosser, B. W. C., Secoy, D. and Riegert, P. (1982). The leg muscles of the American coot (*Fulica americana* Gmelin). Can. J. Zool. 60, 1236-1256.

Rubenson, J., Henry, H. T., Dimoulas, P. M. and Marsh, R. L. (2006). The cost of running uphill: linking organismal and muscle energy use in guinea fowl (*Numida meleagris*). J. Exp. Biol. 209, 2395-2408.

Schorger, A. (1947). The Deep Diving of the Loon and Old-Squaw and Its Mechanism. Wilson Bull. 59, 151-159.

Shufeldt, R. W. (1890). The myology of the raven (*Corvus corax sinuatus*): A guide to the study of the muscular

system in birds. Macmillan and Company.

Shufeldt, R. (1904). On the osetology and systematic position of the pygopodes. Am. Nat. 38, 13-49.

Shufeldt, R. (1913). On the patella in the Phalacrocoracidae. Proc. Zool. Soc. London 83, 393-402.

Strod, T., Arad, Z., Izhaki, I. and Katzir, G. (2004). Cormorants keep their power: visual resolution in a pursuit-diving bird under amphibious and turbid conditions. Curr. Biol. 14, R376-R377.

Vanden Berge, J. C. (1970). A Comparative Study of the Appendicular Musculature of the Order Ciconiiformes. Am. Midl. Nat. 84, 289.

Vanden Berge, J. C. and Storer, R. W. (1995). Intratendinous ossification in birds: A review. J. Morphol. 226, 47-77.

Vanden Berge, J. C. and Zweers, G. . (1993). Myologia. In Handbook of avian anatomy: Nomina anatomica avium (ed. Baumel, J., King, A. S., Breazile, J. E., Evans, H. E., and Vanden Berge, J. C.), pp. 189-247. Cambridge, MA: Nuttall Ornithological Club.

Vogel, S. (2008). Modes and scaling in aquatic locomotion. Integr. Comp. Biol. 48, 702-12.

Weldon, W. (1883). On some points in the anatomy of Phoenicopterus and its allies. J. Zool. 51, 638-652.

White, C. R., Martin, G. R. and Butler, P. J. (2008). Pedestrian locomotion energetics and gait characteristics of a diving bird, the great cormorant, *Phalacrocorax carbo*. J. Comp. Physiol. B. 178, 745-754.

Wilcox, H. H. (1952). The Pelvic Musculature of the loon, *gavia immer*. Am. Midl. Nat. 48, 513-573.

Wisdom, K. M., Delp, S. L. and Kuhl, E. (2015). Use it or lose it: multiscale skeletal muscle adaptation to mechan-

ical stimuli. Biomech. Model. Mechanobiol. 14, 195-215.

Zeffer, A., Johansson, L. C. and Marmebro, Å. (2003). Functional correlation between habitat use and leg mor-

phology in birds (Aves). Biol. J. Linn. Soc. 79, 461-484.

Zinoviev, A. V. (2011). Notes on the hindlimb myology and syndesmology of the Mesozoic toothed bird *Hesper-*

ornis regalis (Aves: Hesperornithiformes). J. Syst. Palaeontol. 9, 65-84.

3

Western and Clark's grebes use novel strategies for

running on water

Coauthors: Tyson L. Hedrick, Andrew A. Biewener

3.1 Abstract

Few vertebrates run on water. The largest animals to accomplish this feat are western and Clark's grebes (*Aechmophorus occidentalis* and *Aechmophorus clarkii*). These birds use water running to secure a mate during a dis-

play called rushing. Grebes weigh an order of magnitude more than the next largest water runners, basilisk lizards (Basilicus basiliscus), and therefore face a greater challenge to support their body weight. How do these birds produce the hydrodynamic forces necessary to overcome gravity and sustain rushing? We present the first quantitative study of water running by grebes. High-speed video recordings elucidate the hindlimb movements of grebes rushing in the wild. We complement these findings with laboratory experiments using physical models and a preserved grebe foot to estimate how slapping the water surface contributes to weight support. Our results indicate that grebes use three novel tactics to successfully run on water. First, rushing grebes use exceptionally high stride rates, reaching 10 Hz. Second, grebe foot size and high water impact speed allow grebes to generate up to 30-55% of the required weight support through water slap alone. Finally, flattened foot bones reduce downward drag, permitting grebes to retract each foot from the water laterally. Together, these mechanisms outline a water-running strategy qualitatively different from that of the only previously studied water runner, the basilisk lizard. The hydrodynamic specializations of rushing grebes could inform the design of biomimetic appendages. Furthermore, the mechanisms underlying this impressive display demonstrate that evolution can dramatically alter performance under sexual selection.

3.2 INTRODUCTION

Only a few animals are capable of running on water. Vertebrates are too dense to support their body above the water surface using surface tension alone, and must instead generate sizable hydrodynamic forces to run on water. Under these circumstances, body mass plays a primary role in determining the difficulty of this feat. Yet, the largest animals capable of running on water, western and Clark's grebes (*Aechmophorus occidentalis* and *Aechmophorus clarkii*), have never been quantitatively studied. These birds water run during a pair bonding display called rushing. An order of magnitude heavier than the next largest water runners, basilisk lizards (*Basilicus basiliscus*; Glasheen and McMahon, 1996a), rushing grebes are an untapped resource for studying the mechanisms used to successfully run on water.

Most animals that locomote on water are small insects, whose long limbs deform the water surface to generate surface tension forces capable of supporting their body weight (Hu and Bush, 2010). Larger animals would need unfeasibly long legs to use this mechanism (Baudoin, 1955). Instead, these animals locomote at the water surface by driving their legs into and through the water with enough power to produce other hydrodynamic forces, resulting from inertial impulses, fluid drag and added mass (Bush and Hu, 2006). Unlike forces generated on solid ground, these fluid forces depend on an object's velocity and shape. Both of these aspects are constrained in large water-running animals. Muscle power and contraction velocities limit the speed at which an animal can move its hindlimb through water (Hill, 1950). Foot sizes that maximize supportive hydrodynamic forces might also produce downward drag during limb retraction or impede movements during other forms of locomotion (Raikow, 1973; Richards and Clemente, 2013). The challenge of these requirements prohibits most animals, including humans, from running on water (Glasheen and McMahon, 1996a; Minetti et al., 2012). Among vertebrates, the only true water runners that have been studied are the basilisk lizards.

Western and Clark's grebes are arguably more successful at running on water than basilisk lizards. The much heavier grebes, weighing between 700 and 1800 g (Vuilleumier, 2009), must produce larger hydrodynamic forces than those of basilisk lizards to sustain water running. Moreover, basilisk lizards experience a limit on their capacity to run on water with increased body size (Hsieh, 2003; Glasheen and McMahon, 1996c). Adults struggle to stay above the water, often sinking after just a few steps. In contrast, a size-dependence on rushing ability has never been observed in grebes, and even the largest birds accomplish rushing bouts that last several seconds and dozens of steps. Lastly, most basilisk lizards initiate water running from land or nearby branches (Rand and Marx, 1967), whereas grebes start rushing from within the water. Grebes must accelerate their body out of the water and against water resistance, requiring the production of hydrodynamic forces greater than their body weight, without the use of their wings. These observations indicate that grebes outperform basilisk lizards at water running on multiple levels. Grebes are thus an interesting system in which to study effective locomotion at the water surface. Furthermore, the tactics that grebes use to support heavy weights during water running is particularly

75

relevant for applications where weight minimization is a consistent challenge, such as robotics.

Rushing is more than an athletic achievement for western and Clark's grebes. During the spring breeding season, grebes perform rushing to attract a mate and reinforce pair bonding. Each display consists of two or more grebes propelling themselves out of the water to run atop the surface. The wings of each bird are held still behind the body, and probably do not contribute to weight support.

Rushing displays typically cover between 5 and 20 m and can last up to 7 s (Nuechterlein and Storer, 1982). Although obviously a representation of strength and stamina, the qualities of rushing associated with female choice have yet to be identified. Rushing takes place throughout the breeding season, but decreases in regularity once most birds pair up and begin preparing for young.

For rushing grebes to successfully stay above the water, the forces produced during each stride must fully counteract gravity. Following the classification used for basilisk lizards (Glasheen and McMahon, 1996a), there are two main stride phases that generate supportive hydrodynamic forces: water slap and stroke. The extent that slap and stroke contribute to support overall body weight varies with size in basilisk lizards. Previous studies that quantify weight support in basilisk lizards focus on the generation of upward impulses: a measurement that incorporates both the magnitude of supportive forces and the time over which they are exerted. In small lizards (<10 g), slap impulses account for up to 60% of weight support, whereas they account for only 25% in large lizards (Glasheen and McMahon, 1996c). Consequently, larger lizards must derive a greater percentage of weight support from stroke phases in order to resist sinking. Weighing even more than basilisk lizards, do grebes also experience a reduction in the extent that slap contributes to weight support? What mechanisms do grebes use to produce enough force to sustain rushing?

This study quantitatively analyzes the rushing behavior of western and Clark's grebes for the first time. Using high-speed cameras, we film grebes in the wild and describe the behavioral and kinematic characteristics of successful water running. To further investigate the force contribution of water slap, we modify a classic experiment to determine the upward impulse generated by model grebe feet in comparison with a freshly preserved grebe

foot specimen. Our results reveal that rushing grebes use a previously unidentified water-running mechanism that involves: (1) using exceptionally high step rates; (2) producing large supportive slap forces with lobate feet; and (3) retracting the feet laterally from the water. Our findings provide new insight into the requirements for running at the water surface.

3.3   RESULTS

Throughout the 2012 breeding season, the density of western and Clark's grebes on Upper Klamath Lake increased and the abundance of rushing displays peaked, sometimes with over 30 displays per hour. Rushing was unaffected by weather conditions or wind speeds. The highest densities of displays occurred in early morning and midday, and were often initiated by environmental disturbances (such as loud passing aircraft or boats). Rushing would repeatedly occur in bouts, with one group displaying numerous times in succession and triggering displays in other groups.

3.3.1   STRIDE DURATION AND FREQUENCY

We calculated stride duration using high-speed video recordings from 40 occurrences of grebe rushing. Rushing displays typically last 4 s, but range up to 7 s (Nuechterlein and Storer, 1982). The data capacity for the high-speed cameras limited each trial to 1.7 s at 325 f.p.s. Therefore, each filmed trial only recorded a section of the full display. For all trials, stride duration ranged between 0.10 and 0.15 s, corresponding to stride frequencies between 10 and 6.7 strides per second (Figure 3.1). Because each rushing stride consists of two steps, our observed stride duration range corresponds to step frequencies between 20 and 13.3 steps per second. As the birds rise out of the water during rush initiation, stride duration is low and typically reaches a minimum within the first 10 steps (Figure 3.1A). Stride duration decreases as grebes continue rushing (Figure 3.1B). Some birds exhibit variability in stride duration throughout rushing; however, this variation does not appear to be linked to weather or water conditions. To terminate rushing, grebes lean forward from their upright rushing posture and dive into the wa-
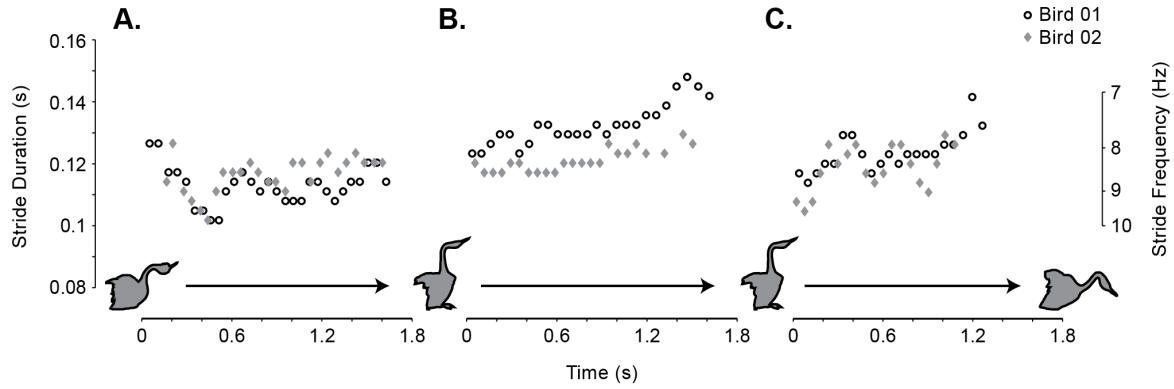
Figure 3.1: Stride duration and frequency during progressive stages of rushing in Western and clark's grebes. Each subplot shows a separate pair of grebes with open circles versus closed diamonds differentiating the two birds. (A) Stride duration decreases immediately (at 0.2 s) after rising out of the water then remains mostly constant. (B) Stride duration and frequency for a pair of grebes during the middle of a rushing display. Stride duration increases for both birds while rushing. (C) Stride duration and frequency for two grebes prior to ending a rushing display and diving into the water. One bird shows a fairly constant increase in stride duration before diving. The other bird☐s stride duration is more variable, but also increases during the final few strides.

ter. Regardless of the absolute stride duration at rushing termination, all birds show a successive increase in stride duration during the final 3-5 steps (Figure 3.1C).

3.3.2 Rushing speed

Because of the challenging field environment, only a small fraction of our recordings were suitable for calibration and kinematic analysis (see Materials and methods for more detail). The suitable recordings are an unbiased, random sampling of all rushing trials. Despite our small sample size, the findings from each trial are consistent.

For eight rushing trials, two calibrated camera views were used to analyze the speed of rushing grebes. The tip of each bird's beak was used as a proxy for whole body movement since grebes hold their neck still throughout rushing. The speed in the water-surface plane typically ranged between 1.5 and 4 m s^{-1} (Figure 3.2). In all trials, the speed of both rushing birds was closely matched. When rising out of the water to begin rushing, translational speed was relatively high and remained mostly constant for at least one second (Figure 3.2A). This high speed coincided with low stride durations. However, speed decreased steadily as rushing progressed, accompanied by an increase in stride duration (Figure 3.2B). None of the calibrated trials showed rush termination. Overall, grebes
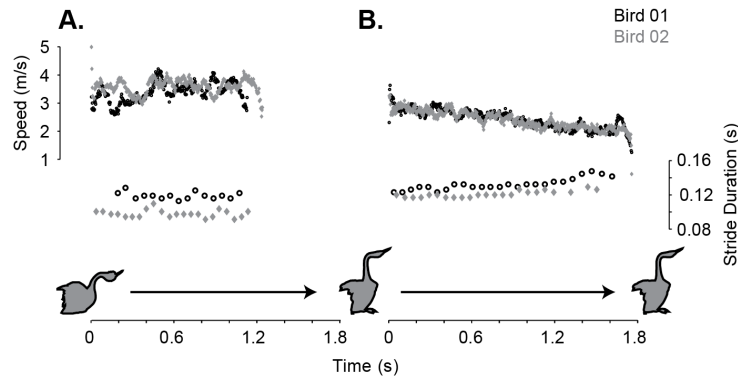
Figure 3.2: Speed and stride duration profiles for two grebes during beginning and middle of rushing. Due to the limited number of calibrated trials used to calculate speed, these profiles are not the same as those shown for stride duration (Figure 3.1). Speed was calculated as the numeric derivative of beak position and was passed through a simple moving average filter using 20 points, which relates to half of the average 40 frames per stride. (A) Two grebes rise out of the water and initiate rushing with relatively constant speeds and stride durations. Although the cameras could capture up to 1.76 seconds, these birds ran outside of the camera view after around 1.25 seconds. (B) Two grebes during the middle of rushing decrease speed and increase stride duration. No calibrated trials included grebes diving into the water after rushing.

began rushing with a high translational speed then, in coordination with their rushing partners, slowed down throughout the rest of the display.

3.3.3 Rushing hindlimb kinematics

In two trials, the distal hindlimb was digitally tracked for a total of 13 strides. Data completeness for each stride varied greatly as a result of bird orientation, water splash and movement inconsistencies. Despite this variation, all strides showed the same qualitative patterns (Figure 3.3C-E). Each stride can be divided into two sections: foot submersion (Figure 3.3C,D; outlined green triangles) and swing (filled-in green triangles). Submersion includes propulsive phases, slap and stroke, as well as foot retraction. Swing is defined as the time when the entire foot is removed from the water. The beginning of water slap marks the transition from swing to submersion.

Throughout the stride, the distal hindlimb moves in a stereotyped pattern. The intertarsal 'ankle' joint (Figure 3.3A, green triangle) makes a slight vertical arc but moves principally in the travel direction of the bird (Figure 3.3C,D). The metatarsophalangeal joint (MTP; Figure 3.3A, red square) is retracted obliquely out of the water, making a broad vertical and medial arc. After reaching its most vertical position, the MTP briefly swings laterally

79
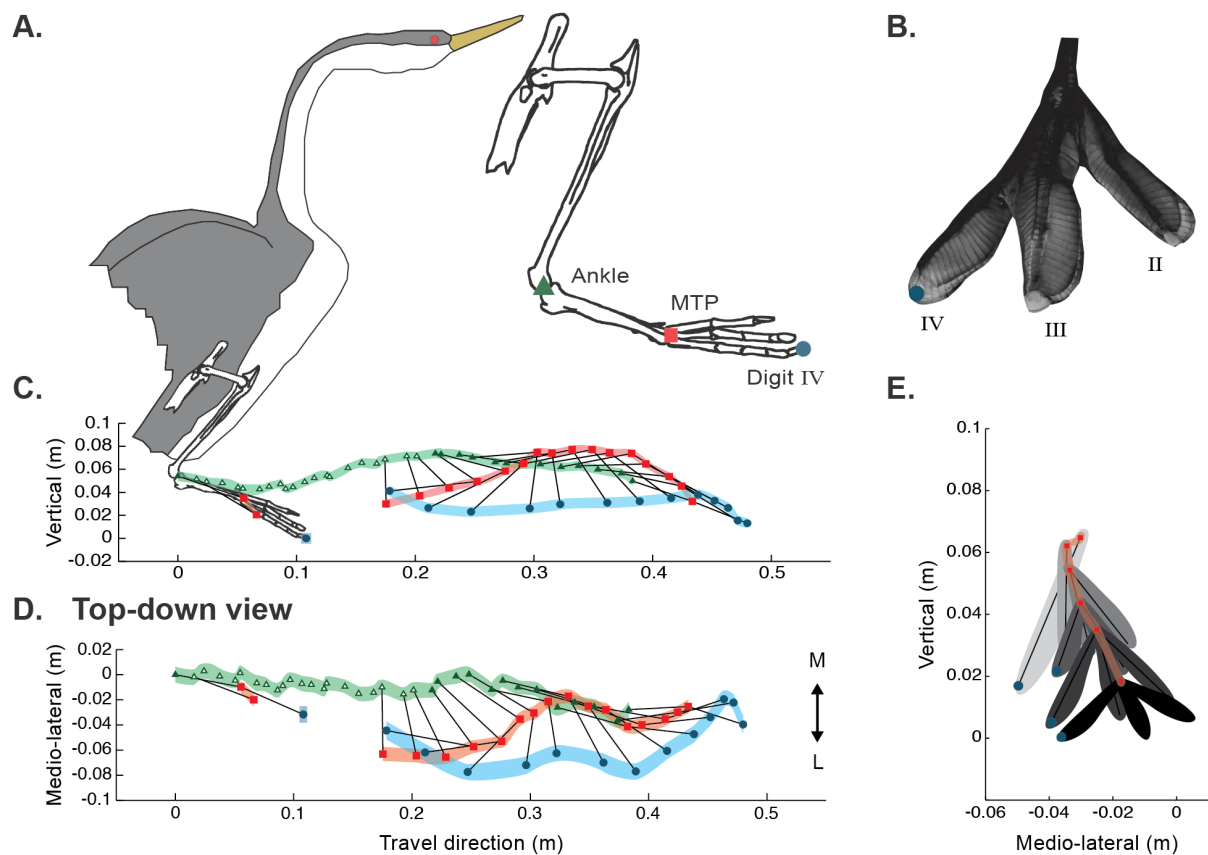
Figure 3.3: 3D kinematics of a complete rushing stride with respect to bird travel direction and vertical. (A) A diagram of *A. occidentalis* body posture during rushing and of the right hindlimb skeleton. The drawing of the skeleton (Museum of Comparative Zoology, Harvard University, specimen 342951) shows digitized locations for the ankle, metatarsophalangeal (MTP) joint, and distal phalanx of digit IV. (B) A detailed view of the asymmetrically-lobed digits of A. occidentalis (MCZ specimen 342951). The hallux, digit I, is located on the palmar side of the foot. (C, D) Movement of the distal right hindlimb during one complete stride, as seen from (C) the right lateral side of the bird and (D) above the bird. Filled-in ankle points (green triangles) denote frames in which the foot is completely removed from the water; open ankle points are times during which part or all of the foot is submerged. The origin is located at the water surface vertically and at the initial ankle position for medio-lateral and travel directions. Light shaded lines represent 95% confidence intervals of marker position for the given calibration and digitized points. Black lines connect digitized joint positions in the same frame. M and L indicate medial and lateral planes, respectively. (E) Details of foot spreading before water slap, as viewed from in front of the bird. Locations of digits II through IV were tracked using high-speed videography of rushing. The origin is consistent with that defined in (C, D). Shading gets darker with consecutive frames, ending with black during the final frame prior to surface slap.

then returns medially during the foot's final descent before slap (Figure 3.3D and Figure 3.4B). At the time of slap, the MTP is medial with respect to the ankle (Figure 3.4B). The distal aspect of each digit was tracked; however, the lobate digits (Figure 3.3B) are collapsed together throughout most of swing, only spreading during the final 15-20 ms before slap. The location of digit IV therefore represents the movement of all digits for the first three-quarters of swing. During foot retraction, the digits are tucked tightly behind the tarsometatarsus. As the MTP travels medially, the digits swing laterally and remain at a fairly constant vertical height (Figure 3.3C and Figure 3.4A). Before descending for slap, the digits begin traveling medially and reach their most vertical excursion.

During the final six frames of swing (approximately 18 ms), the foot descends and the toes spread in preparation for water slap. The ankle makes a small inferior and lateral excursion (Figure 3.3C,D). The MTP and digits undergo coordinated mediolateral movements while descending, resulting in toe spreading. At the beginning of descent, the MTP has already traced a small lateral arc and the folded digits remain lateral to the MTP. The folded digits accompany the MTP as it swings medially; however, the digits undergo a larger excursion and reach a more medial position (Figure 3.4B, arrow). During the final 3-4 frames, the digits separate as digit IV then digit III swing laterally (Figure 3.3E). At the time of slap, the digits are completely spread, with digits II and III medial to the MTP. The velocity of the foot at the time of slap was calculated using the MTP vertical speed during three frames prior to slap. For 13 strides, the foot slap velocity was 3.83±0.65 (mean±s.e.) m s^{-1}.

A. Lateral view

B. Top-down view
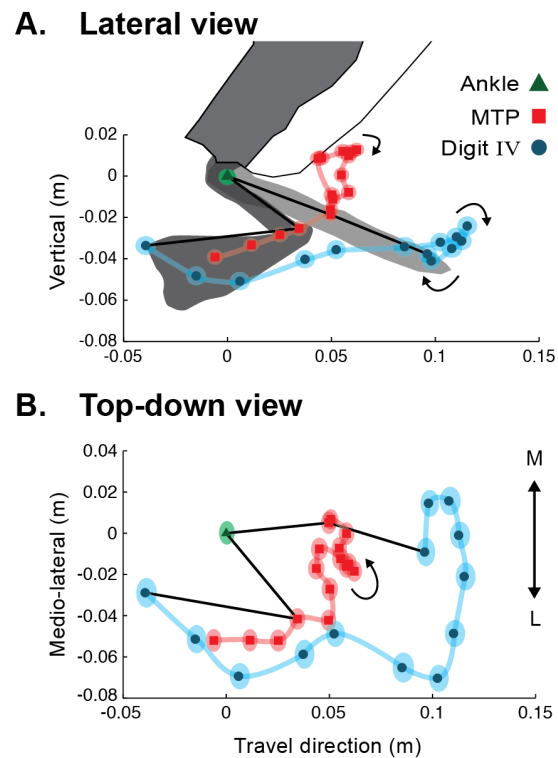
Figure 3.4: Movement of the MTP joint and digit IV relative to the ankle joint during swing. Trajectories of the right distal hindlimb are shown (A) from a lateral view and (B) from above the bird. Lightly shaded ellipses show the 95% confidence interval of the measurement in both directions for each point. Black lines denote the first frame with digit IV visible and the last frame before water slap. M and L indicate medial and lateral plane.

To further understand the forces produced while rushing, a classic laboratory experiment (Glasheen and McMahon, 1996b,c) was reproduced and then analyzed in reference to the slap impact velocity observed for wild grebes (see Materials and methods). We found that the slap impulse of model grebe feet and a preserved grebe foot depends both on impact velocity and foot area (Figure 3.5). Slap impulses generated by the preserved grebe foot (34.2 cm2) relative to the large (34.3 cm2) foot model were slightly larger, but not significantly different (P=0.77, see Materials and methods), suggesting that the small difference may depend on the intrinsic compliance of the preserved grebe foot relative to the rigid foot model. The experimental slap impulses for the models and preserved grebe foot increased with impact velocity. The relationship between slap impulse and impact velocity is best described using a quadratic regression (large model: R2=0.98; large preserved: R2=0.95; small model: R2=0.99; see Materials and methods). The larger model foot and preserved grebe foot produced greater slap impulses than the small model foot.

For a bird with each foot size, the theoretical minimum impulse needed to resist sinking was calculated using the mass of the associated carcass (small: 0.78 kg, large: 1.44 kg) and a maximum stride frequency of 10 Hz obtained from field trials (see Equation 3.1 in Materials and methods). The calculated minimum needed impulses (small: 0.38 N s, large: 0.71 N s) were used to convert the experimental slap impulses into a percentage of what would be needed to stay above water. Within the range of average foot slap velocities observed in field trials, our laboratory-based foot slaps produced between 35-55% (small foot) and 30-50% (large model and cadaver feet) of the impulse needed to support a grebe's body weight (Figure 3.5). While the larger feet produced a greater magnitude slap impulse, its relative contribution to body weight support is less than for the smaller foot model.
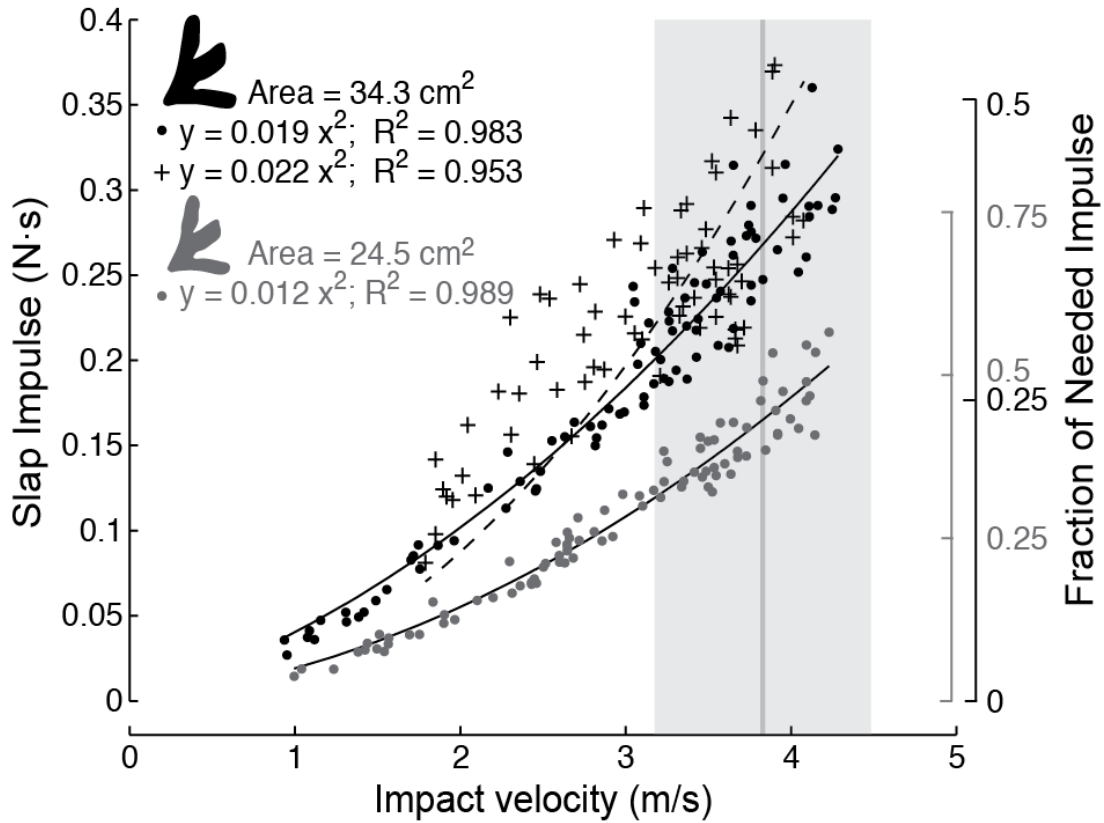
Figure 3.5: Impulse during slap phase of grebe foot models in comparison to a preserved grebe foot. The vertical slap impulse experienced by small (gray circles) and large (black circles) model grebe feet dropped into water in comparison to a fresh taxidermically prepared grebe foot (+ symbols). The prepared grebe foot had a flattened profile area of 34.2 cm², slightly smaller than the large grebe foot model. The coefficients of the best-fit quadratic regressions for the large model foot (solid black line) and large preserved foot (dashed black line) are not significantly different (p=0.77, two-tailed). The vertical gray bars correspond to the average $\pm$ 1 s.e. of foot impact velocities recorded in the wild (3.83 $\pm$ 0.65 m/s). The right-hand y-axis transforms slap impulse values to the fraction of impulse needed to support body weight, using a body mass of 1.44 kg for the large foot and 0.78 kg for the small foot.

3.4   Discussion

For the first time, we filmed and quantitatively analyzed the rushing behavior of the heaviest known water run-

ners, western and Clark's grebes. As a result of their relatively heavy weights, these birds must produce the largest

hydrodynamic forces of any known water- running animal. We analyzed numerous rushing displays during the

spring 2012 breeding season to determine how these birds produce the forces necessary to sustain rushing. We

found three primary elements that contribute to a grebe's ability to successfully run on water: high stride rate,

high slap force production and drag reduction during foot retraction.

3.4.1   Stride rate

During rushing, grebes use the highest stride rate recorded for any previously-studied, running bird. Rushing

grebes take between 14 and 20 steps per second, a stride frequency of 6.7 to 10 Hz (Figure 3.1). This stride rate

equals that of the basilisk lizard (Glasheen and McMahon, 1996c), and is much higher than expected for an an-

imal of a grebe's size. Theoretical biomechanical models assuming dynamic similarity predict that stride fre-

quency should scale inversely with leg length, and therefore body size (McMahon, 1975; Alexander and Jayes,

1983; Biewener, 2003). This scaling relationship has been broadly supported in quadrupedal mammals (Heglund

et al., 1974; Heglund and Taylor, 1988; Iriarte-Díaz, 2002). Although less extensively studied in bipeds, inverse

scaling of stride frequency with body mass holds for several running birds and humans (Gatesy and Biewener,

1991). This work indicates that the heavier grebes should run with lower stride frequencies than basilisk lizards,

but in fact they actually use equal rates. Additionally, bipedal running birds with comparable masses to grebes,

namely guinea fowl, run with lower maximum stride frequencies: 3.2 strides per second on a treadmill (Gatesy

and Biewener, 1991) or 4.0 strides per second in the wild (Maloiy et al., 1979). Compared with running birds of a

similar size, grebes rush with a much higher stride rate. In fact, we were unable to find a record of a higher stride

rate used by any bird.

A high stride rate is essential for grebes to run on water. For a set amount of force that a single step can pro-

duce, an increased stride rate allows that force to be generated more often, directly boosting total force production over a given period of time. While forces could also be augmented through modifications in grebe foot anatomy, these changes are likely to have broad impacts on other aspects of grebe behavior. Larger feet would increase their mass inertia and might therefore limit stride rate. Altering stride frequency faces fewer constraints, and is an effective way for grebes to increase body weight support at the water surface.

Because the stride rate of a water runner directly influences how much force is generated over time, it makes sense for grebes to adjust running frequency based on force requirement. Various rushing phases (e.g. initiation) necessitate differing magnitudes of supportive force. Grebes begin rushing with a very high stride frequency, which then decreases throughout the rest of the display (Figure 3.1). The difficulty of accelerating the body out of the water could account for the peak stride frequency observed at the beginning of rushing. Throughout the remainder of a rushing display, translational speed decreases, accompanied by a decrease in stride rate (Figure 3.2). This link suggests that grebes use stride frequency to regulate force production throughout rushing.

3.4.2   SLAP IMPULSE PRODUCTION

Compared with adult basilisk lizards, western and Clark's grebes obtain approximately twice as much relative weight support from slapping the water surface. Our laboratory experiments suggest that slap phase during grebe rushing accounts for 30-55% of the impulse needed for weight support (Figure 3.5), whereas slap in basilisk lizard water running only contributes 15-30% (Glasheen and McMahon, 1996c). Our results comparing rigid large and small model feet with a slightly smaller taxidermically prepared and mounted grebe foot show that the intrinsic compliance of actual grebe feet only slightly influences the slap impulse generated. In order to sustain rushing, the total impulse generated from each step - including both its slap and stroke phase - must be equal to or greater than the gravitational impulse acting on the bird during that time. By generating larger relative slap impulses, grebes relax constraints on stroke impulse and make whole-body weight support more attainable.

During water slap, both small and large grebe feet contribute similarly to weight support, a trend distinct from

the size-dependent impulse production observed in basilisk lizards. While smaller grebes generate slightly higher relative slap contributions than larger grebes (35-55% vs 30-50%, respectively), the observed difference is much less than that seen in basilisk lizards. Basilisk lizards weighing less than 10 g produce up to 60% of weight support through water slap, whereas adults weighing above 150 g are restricted to 10-25% (Glasheen and McMahon, 1996c). This discrepancy corresponds to variations in success in water running. Juvenile basilisk lizards generate force surpluses exceeding 50% of their body weight (Hsieh and Lauder, 2004), but large adults barely overcome gravity even when producing maximal forces (Glasheen and McMahon, 1996c). In comparison, both small and large grebes produce relative slap impulses similar to those of juvenile basilisk lizards. The slap impulses that all rushing grebes generate correspond to those of only the smallest, and most able, basilisk lizards.

Production of high slap forces by rushing grebes may result from their unusual foot shape and fast slap velocity. Hydrodynamic forces acting on an object predominantly rely on its size, shape and velocity. When compared with basilisk lizards, grebe foot size alone does not account for their enhanced slap force contribution. Using an experimentally derived scaling relationship between basilisk lizard body mass and foot area (Glasheen and McMahon, 1996c), the foot area of a grebe-sized basilisk lizard would be 19 or 27 cm² for a small and large grebe, respectively. Actual grebe feet are only 25% larger than scaled basilisk lizard feet, at 24 and 34 cm². The relationship between area and slap impulse has not been experimentally measured for complicated foot shapes. However, simpler shapes have been examined. Circular discs dropped into water produce slap impulses directly proportional to the mass of a sphere of water with the same radius as the disc, its virtual mass (Glasheen and McMahon, 1996a). Therefore, the slap impulse scales with (disc area)$^{3/2}$. If we assume that grebe feet behave like circular discs, a 25% increase in area only produces a 40% increase in slap impact, not enough to account for the 100% gain observed. Instead, other factors likely contribute to a grebe foot's ability to produce hydrodynamic forces during water slap. First, the feet of all grebes are uniquely lobate, a shape that has been proposed to function as lift-producing airfoils during underwater swimming (Johansson and Norberg, 2000). This shape may benefit rushing grebes by generating larger slap forces. Second, rushing grebes strike the water surface at high impact ve-

locities (v_{impact}) reaching up to 4.5 m s^{-1}. In comparison, basilisk lizards slap the water surface at a peak velocity

of 3.75 m s^{-1} (Glasheen and McMahon, 1996b; Hsieh, 2003). Because hydrodynamic forces increase with velocity

squared (v^2_{impact}), even a modest 20% increase of impact velocity in grebes would amplify slap impulse by 44%.

While size, shape, and velocity may all contribute to observed increases in grebe slap impulse, foot size and slap

impact velocity are likely to be the most important.

3.4.3 Drag reduction

To successfully run on water, an animal must not only produce supportive, upward forces, but also minimize any

downward forces that might induce sinking. These downward forces primarily result from drag acting on the

feet during their retraction from the water. As an animal pulls its foot upward, hydrodynamic drag acts to pull

the animal down. Therefore, reducing drag production during foot retraction mitigates the necessary supportive

forces for staying above the water.

Grebes retract their feet from the water laterally, indicating that they use a different drag reduction mechanism

than basilisk lizards. A critical aspect of water running in basilisk lizards involves retracting the feet through air

cavities formed during underwater stroke (Glasheen and McMahon, 1996a,c). Air has a lower mass density than

water, and therefore imposes less resistive drag. As a basilisk lizard slaps the water and pushes its foot downward,

an air bubble forms behind the foot. Missile drop experiments on basilisk lizard feet indicate that foot size de-

termines the time it takes for the cavity to seal and collapse (Glasheen and McMahon, 1996a,c). To reduce drag,

basilisk lizards pull each foot through the air bubble before its collapse by retracting their feet underneath their

body (Hsieh, 2003). Grebes, however, use a different movement during foot retraction: the metatarsophalangeal

joint makes a broad arc out of the water, exiting the water lateral to the bird (Figure 3.3C and Figure 3.4A). Be-

cause grebes still slap the water surface medially under the body, a lateral foot retraction prohibits them from

utilizing an air cavity. Although it is unknown why grebes would use a lateral retraction, this movement might

reflect a constraint on the underwater stroke foot motion. Diving grebes use a medially directed power stroke

to produce lift (Johansson and Norberg, 2001). Rushing grebes may use a similar tactic to support their body weight, necessitating a lateral retraction of the foot out of the water. Regardless of its potential benefit, the lateral retraction observed during rushing suggests that grebes do not use the same air-cavity tactic as basilisk lizards for reducing drag during foot retraction.

Without the use of an air cavity, rushing grebes must either produce enough upward force to overcome any downward drag or use a unique drag reduction technique. One possibility for the latter could relate to the unusual structure of grebe feet, which become streamlined when collapsed. Grebe feet are compact while exiting the water, with the lobate toes folded together and curled behind the tarsometatarsus (TMT). Although we observed a relatively small effect of foot compliance on slap force production when comparing actual grebe feet with rigid physical models (Figure 3.5), the intrinsic compliance of grebe feet likely facilitates digit collapse and overall compression of the foot. This collapsed orientation also results from specialized foot joints. In grebes, the interphalangeal and MTP articulations allow each digit to rotate when it reaches a flexion of 90 degrees (Stolpe, 1935). The folded digits lie underneath the plantar edge of the TMT. Unlike in most birds, the TMT in grebes is flattened medio-laterally with a relatively thick dorsal edge and tapered plantar edge. A coronal section of the TMT resembles an airfoil with a fineness ratio of 3.3 (Johansson and Norberg, 2001). Together, the TMT and folded toes reduce the cross-sectional area of the foot profile and form a streamlined shape. During retraction, the collapsed grebe feet move in line with the reduced cross-sectional area of the foot profile. The coordination of the limb movements with the collapse of the feet indicates that rushing grebes utilize the specialized anatomy of their feet to reduce drag.

3.5   Applications and conclusions

The difficulty and rarity of water running makes it of high interest in several fields. At least two water-running robots have been developed based on the basilisk lizard (Floyd et al., 2006; Xu et al., 2012). By altering the foot design (Floyd et al., 2008), number of limbs (Floyd and Sitti, 2008) and tail type (Park and Sitti, 2009) these

robots can travel up to 1.2 m at the water surface. Yet, current designs are energetically expensive and can only transition to terrestrial locomotion using footpad designs suboptimal for swimming (Park and Sitti, 2009). The water-running mechanisms used by rushing grebes could provide inspiration for additional amphibious robots. Furthermore, the efficiency with which grebe feet produce upward forces suggests that grebes could serve as important models for the design of commercial and industrial products, such as paddles.

In summary, we find that that, in comparison with basilisk lizards, western and Clark's grebes use three novel mechanisms for running at the water surface. First, rushing grebes take up to 20 steps per second, corresponding to a stride frequency of 10 Hz that is higher than any previously studied running bird. Second, lobate toes and a high impact velocity of the feet allow grebes to generate up to 55% of the force needed to stay above water through slapping the water surface. Lastly, grebes retract their feet laterally, using flattened foot bones and unique distal joint articulations to reduce downward drag. These findings present new insight into the requirements for successfully running on water and help elucidate the complicated hydrodynamics of the air-water boundary. As the largest animals capable of water running, western and Clark's grebes are probably the best models for human-fabricated designs that produce large forces at the water surface.

3.6 MATERIALS AND METHODS

3.6.1 FIELD RECORDINGS

Western and Clark's grebes (*Aechmophorus occidentalis* Lawrence 1858 and *Aechmophorus clarkia* Lawrence 1858) perform rushing in order to select a mate for the breeding season. As a pair bonding display, rushing cannot be elicited in a laboratory setting. Instead, study of this behavior requires observing grebes in their natural environment. The highest density of breeding western and Clark's grebes occurs in the Pacific Northwest. We filmed rushing grebes at Putnam's Point of Upper Klamath Lake (Klamath Falls, OR, USA) during May 2012. Wind speed and weather conditions were recorded at the time of each trial.

Rushing was filmed using two high-speed cameras (NR5S1, Integrated Design Tools, Tallahassee, FL, USA).
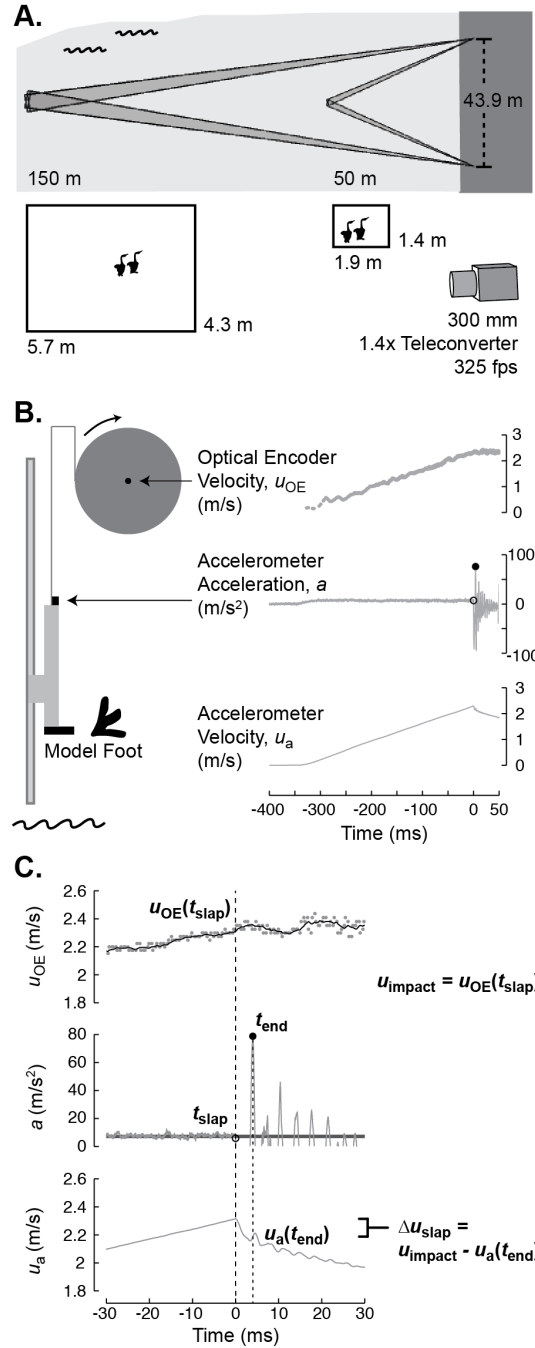
Figure 3.6: Experimental set-up of field recordings and foot slap laboratory protocol. (A) Schematic of high-speed videography set-up at Upper Klamath Lake, OR. Two high-speed cameras were separated by 43.9 m and focused on grebes ranging from 50-150 m away. (B) The set-up for slap impulse experiments and data from a typical trial. One of two 3D printed grebe feet was attached to the bottom of a small, "missile" section of 80/20 aluminum stock. A long vertical length of 80/20 ensured a consistent vertical drop. The foot missile was connected to a foam spool, which was attached to an optical encoder. The angular velocity was converted into the vertical drop velocity of the missile, u_{OE}. An accelerometer attached to the missile measured the missile acceleration, a, and velocity, u_a. (C) Method of extracting data for each slap impulse trial. The time of slap, t_{slap}, was determined as the first acceleration value outside one standard deviation of the average free fall acceleration (dark line in the acceleration record). The velocity at the time of slap impact, u_{impact} was found from the filtered optical encoder velocity curve (moving average, N=5) and used to calibrate the accelerometer velocity profile. The end of slap period, tend, was set as the largest positive value from the accelerometer trace. The velocity at the end of slap, $u_a(t_{end})$, was subtracted from u_{impact} to find the change in velocity of the missile during the slap phase.

The cameras were placed 43.9 m apart on the southshoreline of Upper Klamath Lake (Figure 3.6A). Each camera set-up included a 300 mm zoom lens (70-300 mm, Nikon), a 1.4x teleconverter (420 mm equivalent focal length), and a circular polarizing filter (62 mm). Recordings were collected using Motion Studio Software at 325 f.p.s. with a resolution of 2336x1728 pixels.

Filming a rushing bout was an unpredictable and involved process. At any point in time, between 20 and 200 grebes were present in the observable range of the cameras, typically within 50 to 150 m from the cameras. Rushing grebes began showing pre-rushing behaviors 3-8 s before rushing initiation (Nuechterlein and Storer, 1982). Both cameras were manually repositioned, zoomed and focused on grebes expected to begin rushing. For each rushing trial, the cameras were post-triggered and recorded a maximum of 572 frames, equivalent to 1.7 s. The distance from each camera to the rushing site was estimated using a laser rangefinder (Bushnell Sport 850, Bushnell Outdoor Products, Overland Park, KS, USA). We filmed more than 100 trials in total. We approximate that we witnessed over 1000 rushing displays throughout the month. The trials we filmed represent a random sampling due to filming conditions, and likely do not represented a biased resampling of individuals.

3.6.2   Uncalibrated trials

Twenty of the most focused and zoomed-in rushing trials were analyzed for stride duration. This included 40 birds, with one to three grebes per trial. The stride duration was defined as the time between successive water slaps by the same limb, using the onset of submersion as the indicator of slap. The number of frames between slap was converted to duration (1 frame~3.07 ms) and instantaneous frequency (freq=duration^{-1}). Each trial was identified as rushing initiation, steady rushing or rushing termination.

3.6.3   Calibrated trials

Deriving quantitative spatial information from a rushing trial requires additional camera calibration recordings and analysis. When completed, calibration allows triangulation of a three-dimensional (3D) location from two-

dimensional locations identified in the grebe video images. In this case, calibration was performed by moving an object of known length (a calibration wand) through the field of view of the cameras. An 86 cm wand was attached to a remote control boat, which was then driven through the camera view following a rushing recording. Camera calibration was performed using the easyWand MATLAB (The MathWorks, Natick, MA, USA) routine (Theriault et al., 2014) using the wand information and known camera intrinsic parameters for the principal point and focal length. In addition to the wand length, calibrations were validated by computing the distance between the two cameras and comparing it with the value measured in the field for each recording. The resulting calibration was aligned to the water surface with additional custom MATLAB routines and the final calibration expressed as a set of direct linear transformation coefficients facilitating data analysis using the DLTdv5 MATLAB routine (Hedrick, 2008). Because of the unpredictable location of rushing events, re- calibration of the cameras was required for every trial.

Only a small fraction of rushing trials depicted enough detail for analysis and satisfied the requirements for successful calibration. The difficulties of filming animals in the field limited the scope and quality of our data. Rushing occurred close to shore only a few times. The majority of our recordings captured grebes too far away for detailed study. Furthermore, the direction of rushing and water splash often obscured the view of the hindlimbs, preventing kinematic analysis. The calibration process posed additional challenges. Accurately transforming filmed data to 3D coordinates requires that: (1) both cameras remain perfectly still throughout recordings, (2) cameras do not shift between rushing and calibration recordings, and (3) the calibration wand is recorded in enough locations to provide sufficient shared information among the two cameras. The windy and choppy field conditions, as well as the need to rapidly reposition cameras in anticipation of a rushing event, made it difficult to achieve the first and second criteria, while the remote boat method limited wand information to a ~1-m-high region above the water surface, increasing the number of wand points required for a successful calibration.

Despite the challenges of filming rushing grebes in the wild, moving the calibration wand throughout the camera field of view and achieving suitable camera conditions, eight trials were successfully calibrated, two show-

ing hindlimb detail. These trials were random samples from all rushing trials and showed findings qualitatively consistent with each other. These data are therefore likely to adequately characterize rushing and represent a significant new achievement of obtaining quantitative high-speed three- dimensional kinematic data under field conditions.

3.6.4 Field kinematics analysis

Eight trials were successfully calibrated and 15 grebes were analyzed for whole body speed. The tip of each bird's beak was digitally tracked (Hedrick, 2008). Rushing grebes hold their head and neck still relative to their body, making the tip of the beak a good approximation of whole body movement. The x-y and z speed of each bird was calculated as the numerical derivative of the digitized beak position and was passed through a simple moving average filter using 20 points, corresponding to half of the average 40 frames per stride. Each trial was identified as either rushing initiation or steady rushing. No calibrated trials included rushing termination.

Two of the calibrated trials showed sufficient detail to be used for hindlimb kinematic analysis. In western and Clark's grebes, the upper hindlimb is incorporated in the body musculature and the hip and knee joints are not identifiable. Therefore, the following skeletal landmarks were tracked: ankle joint, metatarsophalangeal joint (MTP) and distal phalanx of digits II-IV (Figure 3.3A,B). These points were often only visible during swing, when the foot was completely removed from the water. During two strides, the ankle was visible for the entire stride. The x-axis was defined as the average travel direction of the bird's ankle joint throughout the digitized range. The y-axis represented the mediolateral plane of the bird, using the digitized points from both ankles. The z-axis was calculated from the cross product of x- and y-axes, representing the vertical axis of the bird relative with an origin at the water surface. Owing to variation in the visibility of joints, kinematic data could not be quantitatively combined over multiple strides.

For two birds, the MTP joint was analyzed to calculate the velocity of the foot at water slap. The MTP impact velocity of 13 total slaps was calculated from the digitized MTP position data for 3 frames prior to slap. The slap

velocity was averaged for each bird then combined to find the grand average and variance.

3.6.5 Slap impulse experiment theory

Measurement of the hydrodynamic forces produced while rushing is not possible from the field kinematics. In order to elucidate the impulses that rushing grebes produce to support their body weight, we modified and replicated a classic laboratory experiment on the water slap of basilisk lizards (Glasheen and McMahon, 1996a,c). The hydrodynamic impulses produced by irregularly shaped objects cannot be theoretically calculated and must be experimentally quantified. Following the model of Glasheen and McMahon (1996a,b,c), we estimate the contribution of water slap to full body weight support. Assuming that only one foot is submerged at a time and aerial phases are short or absent, the minimum impulse needed to fully support one's body weight (Impulse$_\text{needed}$) is:

$$\text{impulse}_\text{needed} = M_\text{b} \cdot g \cdot \tau_\text{step} \tag{3.1}$$

where M_b is body mass (kg), g is gravitational acceleration (m/s²), and τ_step is the period between consecutive foot slaps (s). To meet this impulse requirement and therefore resist sinking, water runners produce hydrodynamic forces during water slap and underwater stroke. Here, we focus on the slap phase because our field recordings do not allow for estimation of underwater movements of grebe feet. The impulse generated by a foot slapping the surface (impulse$_\text{slap}$) equals the mass of water accelerated by the slap multiplied by the slap velocity of the foot . From the conservation of momentum, slap impulse must also equal:

$$\text{impulse}_\text{slap} = M_\text{foot} \cdot \Delta u_\text{slap} \tag{3.2}$$

$$\Delta u_\text{slap} = u_\text{impact} - u_\text{end} \tag{3.3}$$

where M_foot is the foot mass (kg), u_impact is foot velocity at beginning of slap, and u_end is foot velocity at the end of slap phase.

94

3.6.6 Grebe Foot Model Design and Cadaver Preparation

Model grebe feet were designed using measurements from western grebe carcasses and 3D printed. Seven western grebe carcasses (mass=0.7-1.4 kg) were obtained from rehabilitation centers and the limbs were measured and photographed. The area and dimensions of each foot was digitally calculated (ImageJ, NIH, Bethesda, MD, USA). A representative outline of a grebe foot (34.3 cm²) was traced from a picture of the second largest grebe specimen. The outline was scaled to the calculated area of the second smallest (24.3 cm²) specimen. A flat model of each outline was fabricated using a 3D printer (thickness=1 cm). The hydrodynamic performance of the second largest grebe foot specimen (34.2 cm²) was also tested by securing the freshly preserved foot in a taxidermically abducted position using Masters Blend (McKenzie Taxidermy Supply, Granite Quarry, NC).

3.6.7 Slap impulse experiment set-up

The slap impulse of the small and large model grebe feet and the prepared grebe foot were measured using a laboratory set-up similar to that of Glasheen and McMahon (1996a,b,c). Model grebe feet were attached onto a 0.46 m 'missile' of 80/20 aluminium stock (80/20 Inc., Columbia City, IN). The missile was attached onto a 1.52 m long, vertical 80/20 track using a linear motion fitting (Figure 3.6B). The track enforced a consistent vertical drop of the foot into a water tank with a 0.366 m depth. The top of the missile was attached to a low stretch, Spectra string that was wrapped around a foam spool. The spool was directly attached to an analog optical encoder (E5, 900 CPR, US Digital, Vancouver, WA), which measured its angular velocity. This signal was converted to a measurement of the downward velocity of the foot. The optical encoder was calibrated by translating the missile at six known velocities using a linear actuator. A single-axis accelerometer (ADXL193, Analog Devices, Norwood, MA) was enclosed in a waterproof case and attached to the top of the missile. The optical encoder and accelerometer outputs were sampled at 100 kHz.

Using this set-up, the model feet and cadaveric foot were dropped into the water from varying heights (0.04-1.5 m) for a total of 90 trials each. The attachment angle of the cadaveric foot imposed a lower limit on drop height,

precluding trials for the lower impact velocity range. Any trials with irregularities in the optical encoder output were excluded. The mass of the missile, M_{foot}, was weighed before every trial to account for water retention within the missile and string. Timing of slap phase was found from the accelerometer trace. For each trial, the beginning of slap, t_{slap}, was defined as the last data point within one standard deviation of the average free fall acceleration (Figure 3.1C). For the model feet, the end of slap, t_{end}, was determined as the time of maximum acceleration after slap began. Because the attachment of the taxidermically prepared grebe foot prevented the missile from slapping the water surface perpendicularly, the time of slap was prolonged and determined by finding when the derivative of the filtered acceleration trace was positive for the next 300 frames (0.52 s). This threshold was chosen because it consistently corresponded to the inflection point for the integrated velocity as shown in Glasheen and McMahon (1996a, Figure 3.1A). The optical encoder velocity data for both model feet and the preserved grebe foot was passed through a moving average filter (n=5) and the resulting trace, u_{OE}, was used to find the foot velocity at slap impact, u_{impact}. The integrated accelerometer output u_a was calibrated such that $u_a(t_{slap}) = u_{impact}$. The change in velocity during slap was calculated as:

$$\Delta u_{slap} = u_{impact} - u_{end} \tag{3.4}$$

where uend is the velocity at end of slap. The fraction of needed impulse obtained from slapping the water surface was found by:

$$\text{fraction of needed impulse} = \frac{M_{foot} \cdot \Delta u_{slap}}{\text{impulse}_{needed}} \tag{3.5}$$

Impulse$_{needed}$ is calculated using Equation 1 with a τ_{step} of 0.05 s, corresponding with that of the foot model. The body mass associated with each model foot size – 0.78 and 1.44 kg for small and large, respectively – was estimated as the body mass of the carcass with the most similar foot area.

The experimental slap impulse data were fit using a nonlinear regression, $y = a \cdot x^2$, based on hydrodynamic theory (Shiffman and Spencer, 1945) and prior experimental support (Moghisi and Squire, 1981). To test whether

the data for the large model foot differ from those for the large cadaver foot, we use a two-tailed t-test of the regression coefficient a (MATLAB).

Table 3.1: List of abbreviations

a	acceleration output from accelerometer
Δu_{slap}	change in velocity during slap phase
$\text{impulse}_{\text{needed}}$	impulse needed to fully support a water runner□s body weight
$\text{impulse}_{\text{slap}}$	Impulse produced by slapping the water surface
M_{body}	body mass
M_{foot}	mass of foot
MTP	metatarsophalangeal joint
t_{end}	time of end of slap phase
t_{slap}	time of beginning of slap phase
τ_{step}	period between consecutive steps
TMT	tarsometatarsus
u_{a}	velocity from integrated accelerometer output
u_{end}	velocity at end of slap phase
u_{impact}	vertical velocity at impact
u_{OE}	velocity output from optical encoder

3.7 REFERENCES

Alexander, R. and Jayes, A. (1983). A dynamic similarity hypothesis for the gaits of quadrupedal mammals. J. Zool. 135-152.

Baudoin, R. (1955). La physicochimie des surfaces dans la vie des Arthropodes aeriens des miroirs d□eau, des ri-vages marins et lacustres et de la zone intercotidale. Bull. Biol. Fr. Belg. 89, 16-164.

Biewener, A. A. (2003). Animal Locomotion. Oxford, UK: Oxford University Press.

Bush, J. W. M. and Hu, D. L. (2006). WALKING ON WATER: Biolocomotion at the Interface. Annu. Rev. Fluid Mech. 38, 339-369.

Floyd, S., Keegan, T., Palmisano, J. and Sitti, M. (2006). A Novel Water Running Robot Inspired by Basilisk Lizards. 2006 IEEE/RSJ International Conference on Intelligent Robots and Systems 5430-5436.

Floyd, S. and Sitti, M. (2008). Design and development of the lifting and propulsion mechanism for a biologi-cally inspired water runner robot. IEEE Transactions on Robotics 24, 698-709.

Floyd, S., Adilak, S., Ramirez, S., Rogman, R. and Sitti, M. (2008). Performance of different foot designs for a water running robot. 2008 IEEE International Conference on Robotics and Automation 244-250.

Gatesy, S. and Biewener, A. (1991). Bipedal locomotion: effects of speed, size and limb posture in birds and hu-mans. J. Zool. 224, 127-147.

Glasheen, J. and McMahon, T. (1996a). Vertical water entry of disks at low Froude numbers. Phys. Fluids 8, 2078.

Glasheen, J. and McMahon, T. (1996b). A hydrodynamic model of locomotion in the basilisk lizard. Nature 380, 340-342.

Glasheen, J. and Mcmahon, T. (1996c). Size-dependence of water-running ability in basilisk lizards (*Basiliscus basiliscus*). J. Exp. Biol. 199, 2611-8.

Hedrick, T. L. (2008). Software techniques for two- and three-dimensional kinematic measurements of biological and biomimetic systems. Bioinspiration Biomimetics 3, 1-6.

Heglund, N. and Taylor, C. (1988). Speed, stride frequency and energy cost per stride: how do they change with body size and gait? J. Exp. Biol. 138, 301-318.

Heglund, N., Taylor, C. and McMahon, T. (1974). Scaling stride frequency and gait to animal size: mice to horses. Science 186, 1112-1113.

Hill, A. V. (1950). The dimensions of animals and their muscular dynamics. Sci. Prog. Twent. Cent. 38, 209-230.

Hsieh, S. T. (2003). Three-dimensional hindlimb kinematics of water running in the plumed basilisk lizard (*Basiliscus plumifrons*). J. Exp. Biol. 206, 4363-4377.

Hsieh, S. T. and Lauder, G. V (2004). Running on water: Three-dimensional force generation by basilisk lizards. Proc. Natl. Acad. Sci. U. S. A. 101, 16784-8.

Hu, D. L. and Bush, J. W. M. (2010). The hydrodynamics of water-walking arthropods. J. Fluid Mech. 644, 5.

Iriarte-Díaz, J. (2002). Differential scaling of locomotor performance in small and large terrestrial mammals. J. Exp. Biol. 205, 2897-908.

Johansson, L. C. and Norberg, U. M. (2000). Asymmetric toes aid underwater swimming. Nature 407, 582-583.

Johansson, L. C. and Norberg, U. M. (2001). Lift-based paddling in grebes. J. Exp. Biol. 204, 1687-1696.

Maloiy, G., Alexander, R., Njau, R. and Jayes, A. (1979). Allometry of the legs of running birds. J. Zool. 187, 161-167.

McMahon, T. (1975). Using body size to understand the structural design of animals: quadrupedal locomotion. J. Appl. Physiol. 39, 619-627.

Minetti, A. E., Ivanenko, Y. P., Cappellini, G., Dominici, N. and Lacquaniti, F. (2012). Humans running in place on water at simulated reduced gravity. PloS One 7, 1-7.

Moghisi, M. and Squire. P.T. (1981). An experimental investigation of the inertial force of impact on a sphere striking a liquid surface. J. Fl. Mech. 108, 133-146.

Nuechterlein, G. L. and Storer, R. W. (1982). The Pair-formation displays of the western grebe. Condor 84, 351-369.

Park, H. S. and Sitti, M. (2009). Compliant footpad design analysis for a bio-inspired quadruped amphibious robot. 2009 IEEE/RSJ International Conference on Intelligent Robots and Systems 645-651.

Raikow, R. (1973). Locomotor Mechanisms in North American Ducks. The Wilson Bulletin 85, 295-307.

Rand, A. and Marx, H. (1967). Running speed of the lizard *basiliscus basiliscus* on water. Copeia 1967, 230-233.

Richards, C. T. and Clemente, C. J. (2013). Built for rowing?: frog muscle is tuned to limb morphology to power swimming. J. R. Soc. Interface 10, 20130236.

Shiffman, M. and Spencer D.C. (1945). The force of impact on a sphere striking a water surface. Approximation by the Flow about a Lens. App. Math. Panel, NDRC, Report 105.

Stolpe, M. (1935). Colymbus, Hesperornis, Podiceps: ein Vergleich ihrer hinteren Extremit□t. Journal fur Or-nithologie 83, 115-128.

Therialt, D. H., Fuller, N. W., Jackson, B. E., Bluhm, E., Evangelista, D., Wu, Z., Betke, M., Hedrick, T. L. (2014). A method for accurate multi-camera field videography. J. Exp. Biol. 217, 1843-1848.

Vuilleumier, F. (2009). Birds of North America. New York: Dorling Kindersley.

Xu, L., Wei, X., Cao, K. and Shi, Y. (2012). Dynamic analysis of fluid-structure interaction for the biped robot running on water. International Conference on Control, Automation, Robotics and Vision 1546-1550.

4

Foot-propelled swimming kinematics and turning strategies in common loons

4.1 Abstract

Loons (Gaviiformes) are arguably one of the most successful groups of swimming birds. As specialist foot-propelled swimmers, loons are capable of diving up to 70 meters, remaining underwater for several minutes, and capturing fish. Despite the swimming prowess of loons, their undomesticated nature has prevented prior quantitative analysis. Our study used high-speed underwater cameras to film healthy common loons (Gavia immer) at the Tufts Wildlife Clinic in order to analyze their swimming and turning strategies. Loons swim by synchronously pad-

dling their feet laterally at an average of 1.8 Hz. Combining flexion-extension of the ankle with rotation at the knee, loon swimming resembles grebe swimming and likely generates lift forces for propulsion. Loons modulate swimming speed by altering power stroke duration and use head-bobbing to enhance underwater vision. We observed that loons execute tight but slow turns compared to other aquatic swimmers, potentially associated with hunting by flushing fish from refuges at short range. To execute turns, loons use several strategies. Loons increase the force produced on the outside of the turn by increasing the speed of the outboard foot, which also begins its power stroke before the inboard foot. During turns, loons bank the body away from the turn and alter the motion of the feet to maintain the turn. Our findings demonstrate that foot-propelled swimming has evolved convergently in loon and grebes, but divergently from cormorants. The swimming and turning strategies used by loons that allow them to capture fish could inspire robotic designs or paddling techniques.?

4.2   INTRODUCTION

Loons excel at swimming, paddling their feet to dive underwater for more than 70 meters. They survive by capturing fish, a skill that requires a high level of maneuverability and speed. Yet, loons evolved from birds that use the hindlimbs for walking on land, repurposing their legs as paddles. Although producing propulsive forces underwater poses distinct physical challenges from walking, several independent lineages of birds have evolved foot-propelled diving, including grebes, cormorants, seaducks, and extinct Hesperornithiformes (Zinoviev, 2011). Within extant foot-propelled diving birds, loons demonstrate a strong preference for large bodies of water and a particular intolerance for captivity, resulting in loon swimming having never been quantitatively studied. As one of nature's most agile foot-based swimmers, loons offer valuable insight into successful strategies for swimming and maneuvering underwater by means of foot-propelled paddling.

Diving birds face specific physical challenges to power underwater locomotion, leading to varying levels of specialization within foot-propelled diving birds. The most recent common ancestor of all extant birds was able to walk and fly, passing on to its descendants anatomical features to support the body against gravity while on land

and reduce body mass for flight (such as hollow bones). Yet, many of these characters limit swimming performance. All swimming birds must overpower buoyancy to dive, with adaptations to increase body density such as wettable feathers (Grɛmillet et al., 2005) or solid bones (Chinsamy et al., 1998). Birds that swim using their feet encounter particular physical challenges associated with the hindlimbs. The propulsive force generated by a foot depends on its speed, shape, and surface area (Vogel, 2008). To maximize forces, many foot-propelled birds have webbed or lobed toes, but large feet may make walking on land cumbersome. Due to these conflicting pressures on the hindlimb, foot-based diving birds face a trade-off with walking. As a result, foot-propelled swimming has independently evolved to differing levels of specialization, from many cormorants and seaducks that regularly spend time on land (Abourachid, 2001; White et al., 2008) to grebes and loons that can barely stand on solid ground (Johnsgard, 1987).

The loon family includes five extant, Holarctic species, including the common loon (Gavia immer), which breeds on lakes in northern North America and winters along the North American coasts (Johnsgard, 1987). Loons spend almost their entire life on the water, only venturing on land to build and tend a nest near the shoreline. The common loon has been caught in fishing nets dozens of meters below the surface (Schorger, 1947) with diving durations recorded of over two minutes (Nocera and Burgess, 2002). However, loons prefer large territories (Barr, 1996) and adults do not survive well in captivity. The technical challenges of studying loon swimming have impeded any prior analysis of how loons produce the forces necessary to swim using the feet.

Foot-based swimming has historically been considered drag-based, though recent studies of other specialized diving birds suggest their ability to generate lift forces. Steady fluid forces can be categorized into drag and lift. Drag forces resist motion through a fluid, acting opposite to the direction of movement. Lift forces act perpendicular to movement, for example the wings of a plane produce an upward lift force when the plane moves forward. Previously, swimming using the feet was considered drag-based, with the foot paddling backwards to power forward motion (Baudinette and Gill, 1985; Blake, 1981; Fish, 1996; Vogel, 2008). Yet recent studies of cormorant and grebe swimming show that the feet of specialized diving birds do not move backwards relative to still water, and

therefore likely power swimming more through lift- than drag-based forces (Johansson and Norberg, 2000; Johansson and Norberg, 2001; Johansson and Norberg, 2003; Ribak et al., 2004). However, grebes and cormorants likely use different mechanisms for producing lift due to divergence in the shape of the feet and orientation of the limb while paddling. With feet that resemble those of cormorants but exhibiting a similar level of aquatic specialization to grebes, how does loon swimming compare to that of cormorants and grebes? Do loons also exhibit signs of producing lift forces for underwater propulsion?

To successfully capture prey, specialized foot-propelled diving birds must not only power straight swimming but also be highly maneuverable. All previous studies of foot-propelled diving birds restricted subjects to a straight tunnel, though one study included a single vertical obstacle (Johansson and Norberg, 2001; Ribak et al., 2004; Ribak et al., 2008). While informative, such experiments do not measure natural maneuverability in foot-propelled birds. Other freely swimming aquatic animals, from fish to penguins, demonstrate dramatic variation both in the sharpness and speed of turns, and in the movement strategies to control turning (Fish, 2002; Fish et al., 2003; Hui, 1985). Maneuvering animals similar to loons, with a rigid body and that power swimming with the feet, demonstrate a consistent pivoting strategy. These swimmers generate drag on the turning direction side of the body by extending the feet on the inside of the turn (often called the "inboard feet") while continuing to generate thrust using the outside, □outboard,□ feet (Fish and Nicastro, 2003; Rivera et al., 2006). However, unlike previously studied underwater foot-propelled swimmers, loons rely solely on two limbs for propulsion and therefore likely use novel kinematic strategies to control maneuvers.

This study quantitatively evaluates swimming and turning strategies in loons for the first time. Using high-speed cameras in custom-built underwater camera cases, we film four healthy common loons freely swimming in a pool at the Tufts Wildlife Clinic. Kinematic analysis of the body and hindlimbs during straight swimming reveals that loons power foot movement by ankle flexion and knee rotation. The feet are placed in a lateral position and appear to generate lift forces, similar to grebes. We also find that loons use head-bobbing to augment the acceleration of the eye, likely enhancing visual localization of prey. To induce turns, loons use a combination

of several strategies, modulating the (1) speed of the outboard foot, (2) the relative timing of foot motion, and (3) particular features of each foot's motion. Our findings provide the first evaluation of swimming in loons and reveal new mechanisms for controlling maneuvers using foot-based underwater swimming.

4.3   Materials and Methods

4.3.1   Swimming recordings

Common loons live in large bodies of water, often observed swimming at many distant locations throughout the day. The unpredictability of where loons swim combined with variable water clarity hinders filming loons underwater in the wild. On the other hand, adult common loons do not fare well in captivity, contracting an often-fatal respiratory fungal disease when under acute stress, including during stays in captivity (Miller and Fowler, 2014). Common loons are listed as a species of concern in MA (321 CMR 10:00, 2010) and threatened in NH (Wildlife Action Plan, 2015), preventing the explicit capture of loons for observation in potentially life-threatening conditions. For these reasons, we filmed swimming loons at the Tufts Wildlife Clinic (North Grafton, MA) during rehabilitation stays.

Between 2014 and 2016, four healthy loons were filmed at the Tufts Wildlife Clinic. Many of the loons brought into rehabilitation centers are not healthy enough for filming, quickly succumbing to lead poisoning from fishing tackle or traumatic injuries (Sidor et al., 2003). However, some loons are admitted with minimal injuries and are quickly released back into the wild. The Tufts Wildlife Clinic primarily receives loons during fall migration. Migrating loons are primarily brought into rehabilitation centers under three circumstances. First, loons may become trapped by encroaching ice on a pond or lake, without enough space to take flight. Second, loons accidentally mistake rain- or snow-covered parking lots for bodies of water and make controlled landings without the ability to take off from land. Third, during particularly intense storms, loons may crash land, often breaking bones in the process but unable to take off from land even if uninjured. Although this last circumstance often results in significant injury to the loon, loons brought into rehabilitation centers under the other two circumstances

are usually healthy and ready for release in one or two days. The four loons filmed in this study sustained no major injuries and were filmed on the day of release, usually during the hours just prior to release. At the time of recording, the loons weighed between 2.5 to 3.2 kg, within the normal range for adults (Johnsgard, 1987). Therefore, despite using rehabilitated loons, the data presented here accurately represent swimming by healthy loons.

Loon swimming was filmed using two high-speed cameras (NR5S1, Integrated Design Tools, Tallahassee, FL, USA) in an indoor, 3.05 m diameter pool. The cameras were placed in custom-made underwater cases using adapted scuba dive boxes and 8020 aluminum framing (Figure 4.1). A wide-angle lens was attached to each camera (14mm, f/3.2, Rokinon) and focused at a distance of 1.8 m in air. The effective lens focal length increases when submerged resulting in an approximate in-focus depth of field of 1.3-2.7 m from the camera.

Specific measures were taken to minimize loon stress and loon-human interaction throughout the recording sessions in accordance with animal care protocols (Tufts IACUC G2013-103). Veterinary staff at the Wildlife Clinic removed the loon from the pool to be placed in a net-bottom cage while the camera stands and cameras were placed into the pool. The shared field-of-view of the cameras were calibrated using a custom-built submersible LED wand (30 cm length) filmed at 2 fps during at least 100 frames. As the loon was returned to the pool, length measurements of the beak, tarsometatarsus, and digits were recorded. Body mass was measured during a check-in evaluation from within 24 hours before the recording. Once returned to the pool, each loon was filmed for up to 5 hours, with regular breaks to turn off the extra, overhead halogen lights. An opaque sheet covering the netting above the pool (Figure 4.1) prevented the loon from observing the researchers. Diving was often voluntary, though occasionally elicited by making a noise or moving the sheet. For each loon, 3-5 bait fish were released into the pool to elicit hunting dives. Recordings were collected using Motion Studio Software at 200 frames per second with a resolution of 2336x1728 pixels. The cameras were post-triggered and recorded a maximum of 572 frames, equivalent to 2.86 seconds. Loons were often removed from the pool and directly prepared for transportation to be released. The field of view was calibrated again before the set-up was dismantled. Across four individuals, we recorded 159 swimming trials.
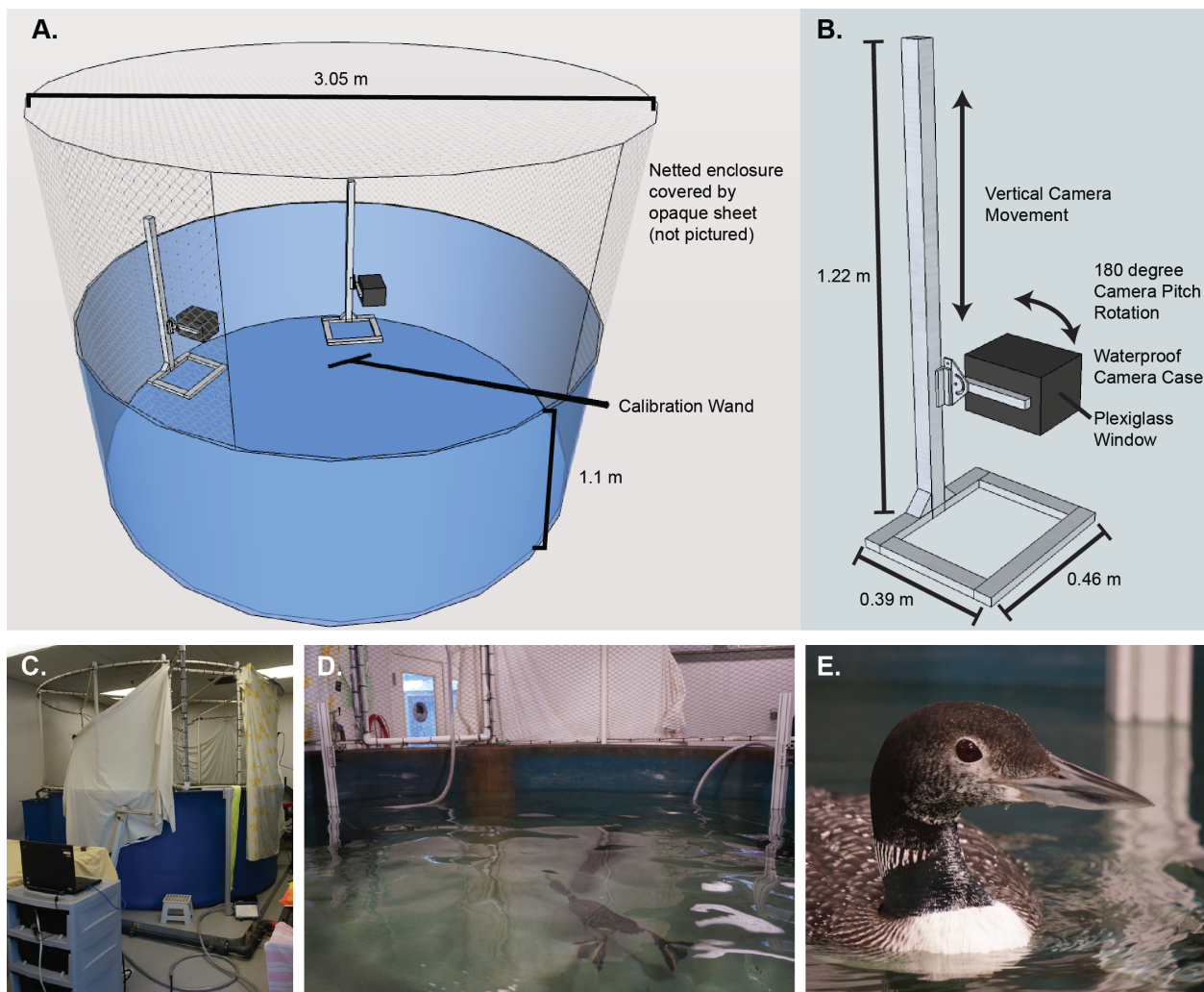
Figure 4.1: Filming set-up at the Tufts Wildlife Clinic. (A) Two cameras were placed in a 3.3 m diameter pool, where rehabilitating loons were housed. A calibration wand was used to calibrate the area for 3D reconstruction. (B) Custom camera cases and stands were built for IDT NR5S1 cameras. Scuba dive boxes were outfitted with a plexiglass window, removable camera mount, and plumbing tube (to waterproof and protect the camera's cable to its power box). The stand was built using 80/20 aluminum framing. (C) While recording, a sheet was placed over the netting to reduce loons stress levels. (D) Loons voluntarily swam underwater in the field of view of both cameras. (E) All four common loons were healthy and released to the wild within 24 hours of recording.

4.3.2 3D motion tracking

Calibration of the cameras for each day of filming was performed to convert two-dimensional data from each camera to three-dimensional (3D) information relative to a local coordinate system. Camera calibration was performed in MATLAB (The Mathworks, Natick, MA, USA) using easyWand5 (Theriault et al., 2014). Each wand calibration included at least 500, and up to 1200, digitized frames and was calculated by estimating the focal length and principle points of the cameras. The calibrations were aligned to vertical using a large, metal calibration object placed into the pool during calibration trials. Of the 159 trials, 19 were analyzed in detail. These trials were chosen to cover a diversity of swimming behaviors (vertical diving, straight swimming, and turns) while ensuring that the bird was in focus and that an identifiable point on the body was visible in both views (more details provided below). Each swimming stride consists of two phases, the power stroke and recovery phase. During the power stroke the foot pushes backwards relative to the body to propel the bird forward. During the recovery stroke, the toes collapse onto each other and the foot is retracted cranially in an arc. The timing of power strokes during each trial was determined by visually identifying toe abduction and adduction for each foot. Although some past studies on straight swimming define the power stroke based on the acceleration of the body (Johansson and Norberg, 2001), this measure does not account for variation between the feet, an important factor for turning. The start of the power stroke was identified as the point when the digits begin to abduct and the metatarsophalangeal (MTP) joint begins to extend. The end of the power stroke was defined as the point when the toes have mostly collapsed upon each other with the MTP joint moving cranially. Each stride was classified as straight swimming or turning to the left or the right.

The body and head of the loon was tracked in 19 trials and the limb was tracked for 10 strides in 6 trials. Like many waterbirds, loons intensively preen and are highly sensitive to any disruption to the waterproofing of their feathers. In order to minimize stress to the birds, we could not attach an object onto the body to facilitate tracking anatomical planes of the loon. Instead, body motion was tracked most often using a feather coloration pat-

tern at the midline of the caudal abdomen near the vent. When the vent was not visible in both cameras, either a point along the midline of the tail or a feather pattern along the back was used. The head was tracked using either the eye or the tip of the beak. In loons, the upper hindlimb is incorporated within the abdominal body skin making the hip and knee joints invisible. However, these joints remain relatively immobile due to skeletal structures stabilizing both joints (Hertel and Campbell Jr, 2007; Wilcox, 1952), with most of the foot's motion stemming from the ankle. The following hindlimb landmarks were tracked for at least one limb during each of the six trials: intertarsal "ankle" joint, metatarsophalangeal joint, and distal phalanx of digits II-IV. In all, over 24,000 points were digitized by hand for this study.

4.3.3 Kinematics Analysis

Power stroke time, stride time, and duty factor were determined for each foot separately throughout the trial. Power stroke time was calculated by converting the number of frames between the beginning and end of the power stroke to duration (1 frame = 5 ms). Stride duration was determined using the start of sequential power strokes since the beginning of toe abduction could be identified more accurately than toe collapse. A swimming duty factor was defined as the fraction of the stride used to power swimming, calculated as the power stride time divided by the stride time. For each of these variables, individual values were categorized as relating to straight swimming, the inboard foot during a turn, or the outboard foot during a turn.

The tracked 3D motions of the body, head, and hindlimb were smoothed and rotated relative to the body of the loon. Custom MATLAB scripts applied a cubic spline (smoothing parameter = 0.01) to the data. The relatively extreme smoothing parameter derives from a high frame rate relative to motion speed. Rotation matrices were defined and applied at each time-step based on trajectory-based and anatomical axes. The x-axis was defined as the travel direction of the body. The y-axis corresponds to the line connecting the left and right ankle joints, representing the mediolateral plane of the bird assuming symmetrical or limited motion of the ankles relative to the body. The z-axis was calculated as the cross product of the x- and y- axes, approximating the dorsoventral

plane of the body. Loons swim with a downward anterior tilt of the body relative to the travel direction resulting in a slight offset between the z-axis and dorsoventral plane of the loon. However, the consistency of the anterior tilt among trials supports the usefulness of x-, y-, and z-axis comparisons across strides and individuals.

Average speed and turning characteristics were quantified for each stride. Previously, strides were defined for each foot. To combine these strides into a full-body measure, each stride was defined as starting with the first foot beginning its power stroke and ending at the first power stroke from the next stride. An average speed throughout each stride was calculated only if the body had been tracked for over 70% of the stride. The horizontal motion of the body was analyzed to quantify the extent of turning throughout each stride while neglecting the impact of buoyant forces. For strides in which at least 30% of the stride was digitized, a 2D circle was best fit to the horizontal trajectory (Taubin, 1991; Figure 4.2). The radius of this circle was considered the average radius of curvature, r. While past studies have used a measure of instantaneous radius of curvature, we found this measure to overestimate the turning ability of the loon due to small deviations in the loon body trajectory. Using the average radius of curvature, stride angular velocity, ω, was calculated as:

$$\omega = \frac{u}{r} \tag{4.1}$$

with u standing for average horizontal velocity throughout the stride and r being the average radius of curvature from the best fit circle. From this, the centripetal acceleration acting on the loon throughout the stride, a_c, in m s^{-2} is:

$$a_c = \frac{u^2}{g * r} \tag{4.2}$$

where g is gravitational acceleration (9.8 m s^{-2}). Together, these parameters give an approximate measure of the extent of turning throughout a stride.
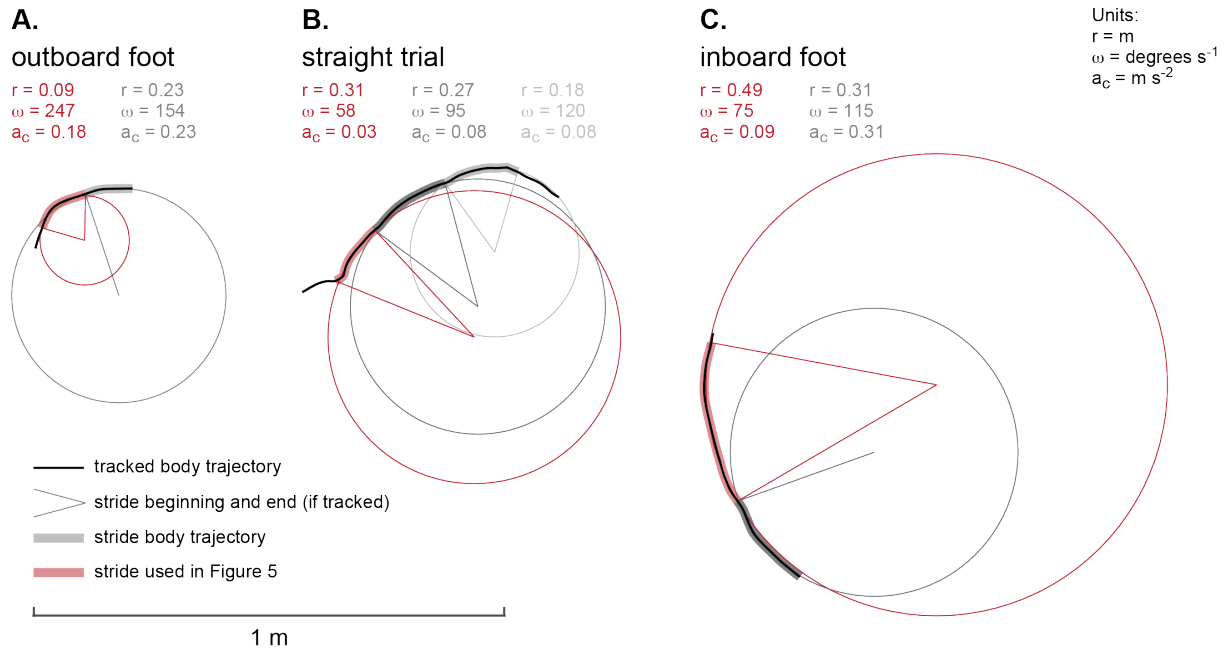
Figure 4.2: Analysis of turns using body trajectory data. Maneuverability and agility were determined by analyzing the trajectory of the loon's body during individual strides. For each stride where over 70% of the stride was tracked, a circle was fit to the horizontal traces of the body. The radius of the curvature (r), angular velocity (?), and centripetal acceleration (ac) were calculated for each stride. The panels in this figure represent the strides displayed in Figure 4.10 (red) for (A) a turn with the outboard foot tracked, (B) straight swimming, and (C) a turn with the inboard foot tracked. All panels are scaled to the 1 m scale bar.

We statistically analyzed whether stride duration, power stroke duration, duty factor, stride speed, and foot speed differ if loons swim straight or turn. We tested the influence of "foot type" (straight, inboard foot, outboard foot) by fitting a linear mixed-effect model (Fit type = REML) to the data and using a Likelihood Ratio Test (MATLAB 2015b). The first model tested the influence of foot type while accounting for random effects from individual identification (Output ~ Foot + (1|Individual)). These models were repeated binning together inboard and outboard foot data to compare straight swimming strides to all turning strides. The Likelihood Ratio Tests were conducted using a model with the □Foot□ fixed effect. We were unable to perform these analyses on foot splay (max distance between digits II and IV) due to a small sample size of tracked foot strides and relatively large anatomical variation among individual loons. To account for the influence of swimming speed on stride duration, power stroke duration, and duty factor, we repeated the linear mixed-effect modeling using an extra fixed
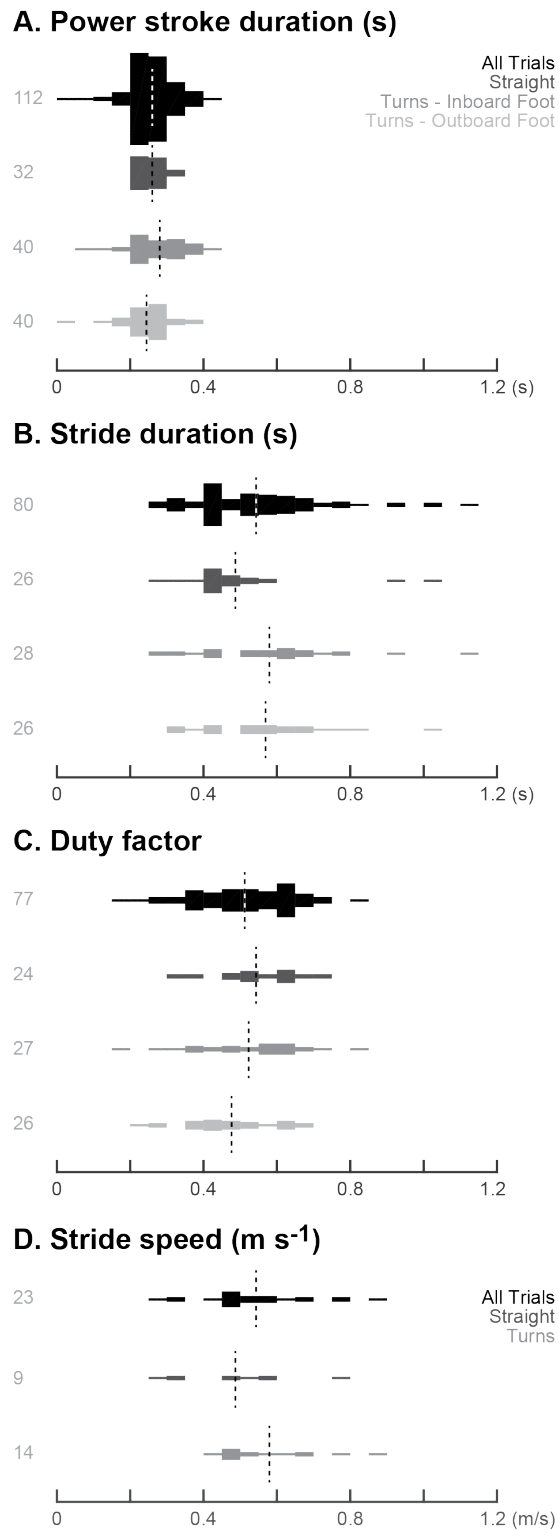
effect (Output ~ Foot + Speed + (1|Individual)). Again, these models were performed with two separate stride groupings: straight vs. inboard vs. outboard and straight vs. all turning. The Likelihood Ratio Tests were conducted by removing the "Foot" and "Speed" effects independently. We determined significance using a cut-off of p = 0.05. Having only 10 strides with the foot tracked, we used a t-test (two-sample, equal variances) to compare the average speed and total distance traveled of digit II throughout the power stroke. All values are listed as the average and standard error.

4.4 Results

Despite swimming in a confined pool, loons exhibited a range of normal and extreme behaviors. All four filmed loons frequently dove underwater voluntarily. When a fish was released into the pool, the loon would often capture the fish within 1-2 seconds before the fish could swim down from the surface. When multiple fish were released at the same time, the loon quickly captured each individual. Most of the loons demonstrated an acute fear of humans, and would dive instantly upon hearing or seeing the researchers. One of the loons showed no fear of humans, following the researchers around the pool and actively investigating the camera cases and stands. Each loon was filmed performing escape dives as well as voluntary relaxed dives.

Within the 19 tracked trials, loons swam at body speeds ranging from 0.16 to 0.86 m s^{-1}, averaging 0.56 m s^{-1}. Stride duration ranged from 0.29 to 1.11 s, with an average of 0.55 ± 0.02 s (s.e.; Figure 4.3 B; Table 4.1). Power stroke duration exhibited less variation, from 0.10 to 0.425 s, averaging 0.265 ± 0.005 s (Figure 4.3A). Duty factor varied from 0.16 to 0.86, with an average of 0.51 ± 0.01. In strides where the body was digitally tracked for more than 70% of the duration, speeds ranged from 0.29 to 0.89 m s^{-1}, and averaged 0.54 ± 0.03 m s^{-1}.

A. Power stroke duration (s)

All Trials
Straight
Turns - Inboard Foot
Turns - Outboard Foot

112

32

40

40

0   0.4   0.8   1.2 (s)

B. Stride duration (s)

80

26

28

26

0   0.4   0.8   1.2 (s)

C. Duty factor

77

24

27

26

0   0.4   0.8   1.2

D. Stride speed (m s^{-1})

23

All Trials
Straight
Turns

9

14

0   0.4   0.8   1.2 (m/s)

Figure 4.3: Descriptive stride parameters of straight and turning swimming. Data from 112 strides in 19 trials across four loons showing values for all strides (black), straight swimming strides (dark grey), inboard foot of turning strides (medium grey), and outboard foot of turning strides (light grey). Violin plots (vertically-mirrored histograms) show (A) power stroke time, (B) stride time, (C) duty factor, and (D) body speed during strides. Data for stride speed is combined for inboard and outboard feet as turn data (medium grey). The width of each bin represents the number of data points, with values consistent across all panels. Dashed lines show the mean of each distribution. Numbers at the left list the total number of strides depicted in each plot.

Table 4.1: Means and standard errors of kinematic parameters of loon swimming. In 19 recorded trials of loons swimming freely underwater the timing of foot paddling and body speed were tracked. The table shows the average and error values for several kinematic parameters for all strides and decomposed into three swim-type categories: strides where the loon was swimming straight, turning strides with the inboard foot tracked, and turning strides with the outboard foot tracked. The n columns show how many strides were analyzed for each kinematic parameter and swim-type category.

	All trials			Straight Strides			Inboard Foot			Outboard Foot		
	n	Mean	Std. Error	n	Mean	Std. Error	n	Mean	Std. Error	n	Mean	Std. Error
Power stroke time (s)	112	0.265	0.005	32	0.258	0.006	40	0.279	0.011	40	0.257	0.008
Stride time (s)	80	0.546	0.020	26	0.487	0.032	28	0.578	0.036	26	0.569	0.032
Duty factor	77	0.513	0.015	24	0.542	0.024	27	0.521	0.029	26	0.478	0.023
Stride speed (m s^{-1})	23	0.542	0.031	9	0.484	0.053	5	0.637	0.076	9	0.546	0.035

The distal hindlimb was digitally tracked for eight complete strides in six trials, including two strides with tracking of both feet resulting in a total of ten tracked strides. Despite some variation in the kinematics among individuals and trials, all strides demonstrate qualitatively similar limb motion during the power and recovery strokes (Figures 4.4, 4.5). The foot (from MTP to tip of digits) begins the power stroke lateral and somewhat ventral to the abdomen. Relative to the body, the foot then arcs caudally, dorsally, and medially, ending the power stroke behind the body with the feet facing medially. This foot motion results primarily from extension of the tarsometatarsus at the intertarsal ankle, with only a small dorsal and lateral arc of the ankle relative to the body (Figure 4.5, green). Note that, as depicted in Figure 4.5, due to concurrent forward movement of the body, the foot experiences an overall forward motion (in the travel direction) relative to still water throughout the power stroke. The foot moves opposite to the travel direction only modestly, with comparatively large excursions in the ventral-to-dorsal and lateral-to-medial directions.

Throughout the power stroke, the digits extend and abduct at their MTP joint (Figure 4.5, thin, lighter blue lines). In most trials, the digits hyperextend, reaching angles greater than 180° relative to the tarsometatarsus. However, in situations where the inboard foot is used as a rudder or executes a small power stroke compared to the outboard foot, the digits only somewhat abduct and never hyperextend. As the foot reaches a position behind the loon's body, the MTP flexes and the toes adduct, eventually collapsing onto each other and signaling the end of the power stroke.

During the recovery stroke the MTP travels in an arc cranial, medial, and slightly lateral relative to the body. The folded digits swing behind the tarsometatarsus. The ankle moves only slightly relative to the body during the recovery stroke. At the transition from recovery to power stroke, the forward-moving MTP slows down and reverses its motion to begin moving backwards relative to the body. At this point, the foot rotates from facing caudally during the recovery stroke to facing dorsally and medially during the power stroke.
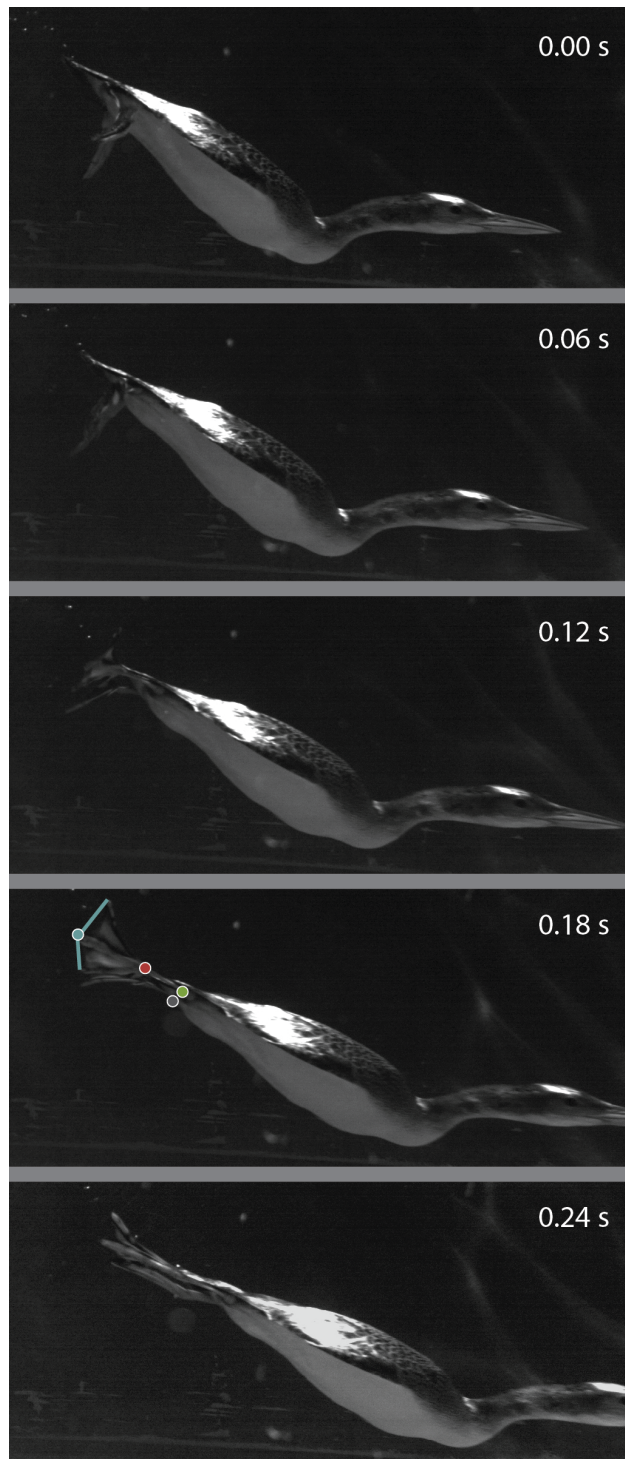
Figure 4.4: Lateral view of loon power stroke during straight swimming. Each image is cropped from one camera's full field of view. The cropped area does not change among panels, representing loon motion relative to still water. Loons propel the body forward by pushing their feet backwards against the water. Each foot travels in a lateral, backwards arc relative to the body due to extension at the intertarsal ankle joint. Throughout the power stroke, the digits abduct and extend at the MTP joints. The power stroke ends as the ankle begins to flex, bringing the MTP joint forward and collapsing the digits onto each other. For this stride, the power stroke lasted 0.24 s. The circles and lines in the 4th panel correspond to the colors used in Figures 4.5 and 4.10.

A. View from above

power stroke

0.17 s   0.27 s   recovery stroke
                                     0.16 s

body

medial

intertarsal ankle

metatarsophalangeal
joint

lateral

digit III

10 cm

B. View from right side

dorsal

ventral

movement
direction

travel direction
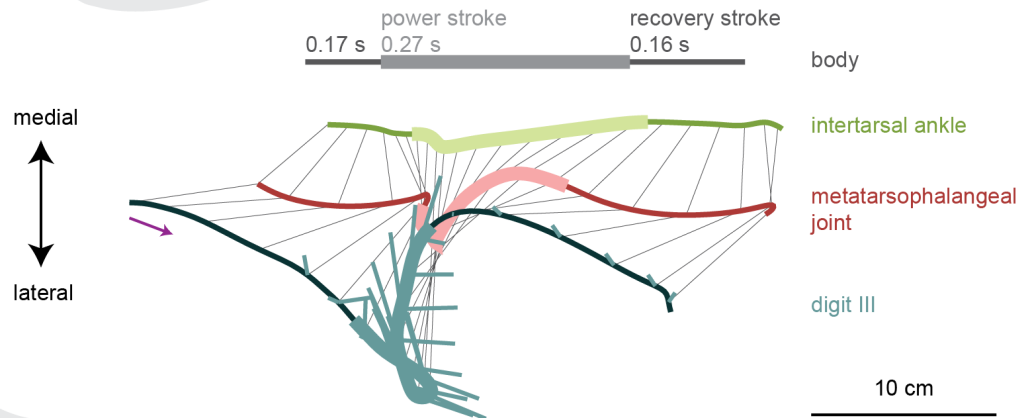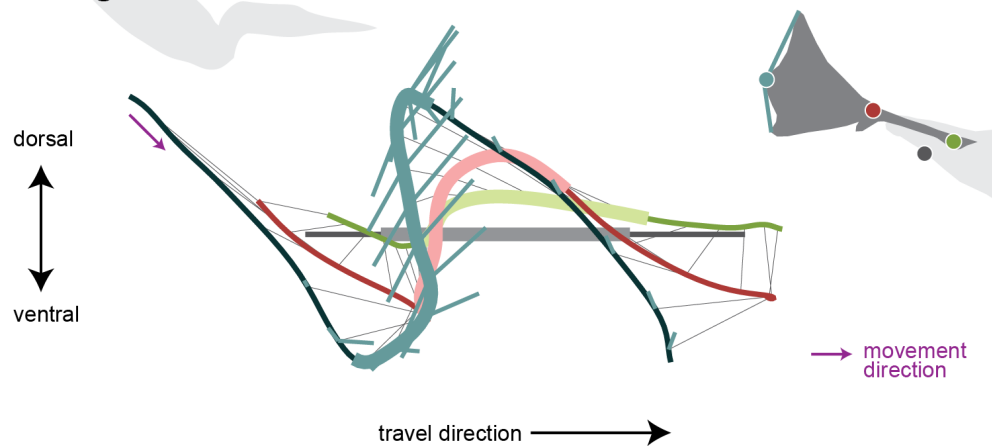
Figure 4.5: Right foot motion during straight swimming relative to still water in terms of loon anatomical axes. The traces show tracked motion relative to still water from a recovery stroke (thin lines), power stroke (thick lines), then another recovery stroke of a loon swimming in a straight trajectory. The 3D data were rotated to be in reference to the travel direction (x-axis), mediolateral plane (A y-axis), and dorsoventral plane (B y-axis). (A) View of the right limb from above the loon showing the body (gray), intertarsal ankle (green), metatarsophalangeal joint (MTP, red), and tip of digit III (blue). (B) View of the right limb from the right side of the loon. The bold and lighter shade traces represent the power stroke. The thin gray lines represent the two skeletal elements. Proximally, the tarsometarsus connects the ankle to the MTP joint. Distally, digit III connects the MTP joint to the tip of digit III. Thin, lighter blue lines connect the tip of digit III to the tips of digit II and IV. Lines represent every 3rd frame (0.015 s). Both panels scaled to 10 cm scale bar.

4.4.2 HEAD-BOBBING

In approximately one-third of the 19 tracked trials, loons exhibited head-bobbing. As their body glides forward during the recovery stroke, loons retract their neck to slow the velocity of the head relative to still water, sometimes achieving a stationary head position (Figure 4.6). During the power stroke, the loons extend their neck, resulting in a faster acceleration of the head compared to the body. Within the 11 tracked head-bobbing strides, the head reached a maximum speed of 1.13 m s^{-1} and acceleration of 7.96 m s^{-2}, three times faster than the body (Figure 4.6). Loons did not head-bob during quick escape dives or sharp turns, but only during relatively horizontal swimming.
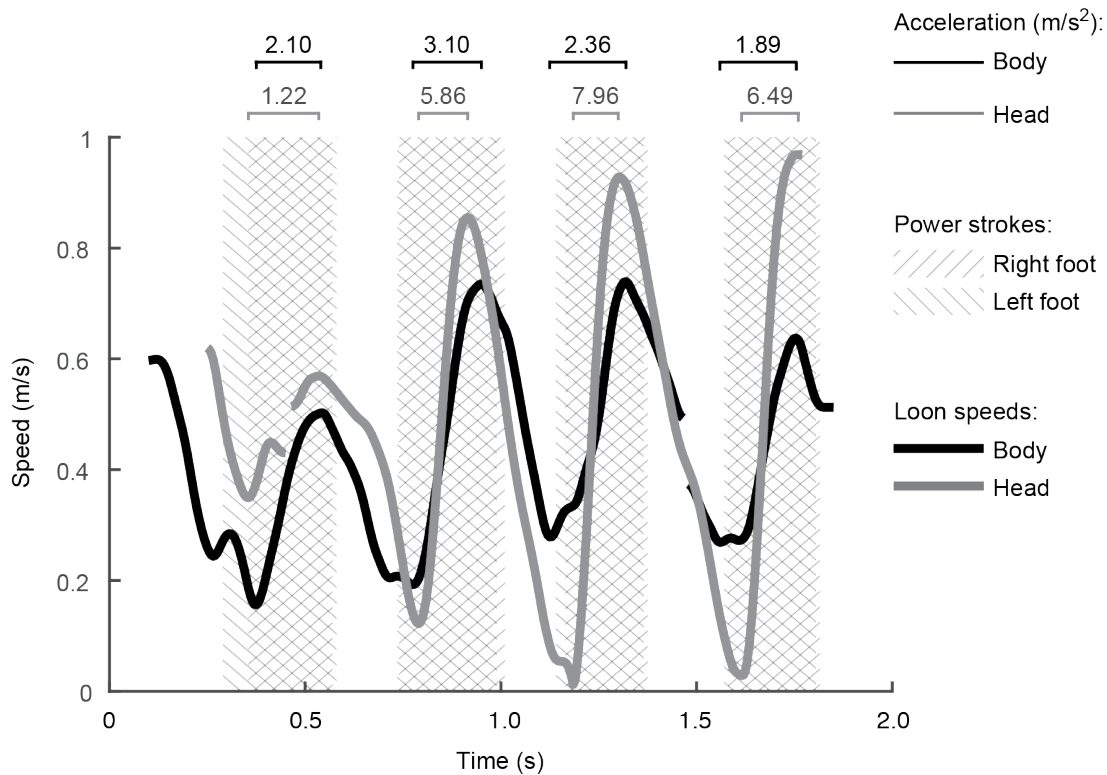
Figure 4.6: Body and head speed of a head-bobbing loon. Bold traces show the body (black) and head (gray) speed of a common loon swimming underwater throughout time (x-axis). Gaps in the traces represent regions where the view of the tracked feature was obstructed. Crosshatched panels depict the timing of the right and left power strokes, as determined by observing foot motion. Average acceleration was calculated as the change in speed over change in time from the lower speed to the highest speed within a stride. Head-bobbing allows loons to stabilize the head, and likely their gaze, during late recovery stroke. During early power stroke as the body accelerates, loons extend the head reaching accelerations over three times faster than the body.

4.4.3 Turning strategies

Since filming occurred in a relatively small circular tank, most of the tracked trials recorded loons turning. Across all 36 strides with the body tracked for at least 30% of the stride, the average stride radius of curvature, r, was 0.42 ± 0.07 m with an extreme value of 0.06 m, or approximately 0.07 body lengths (conservatively, calculated based on a maximum body length of 0.91 m). The average stride angular velocity (ω) was 92.4 ± 10.9 degrees s^{-1}, with an extreme of 287 degrees s^{-1}. The average stride centripetal acceleration (a_c) was 0.08 ± 0.01 m s^{-2}, with an extreme of 0.20 m s^{-2} or 0.02 g.

Loons use several strategies to execute turns, including changing their body and wing positions, moving their feet at different timings, and varying factors that influence the force produced by each foot. In every observed turn, the body of the loon rolled out of the turn resulting in the ventral belly facing into the turn (Figure 4.7). For many turns, loons slightly extended their wings, particularly the outer wing during tight turns (Figure 4.7). During one almost 180° turn, the loon also depressed its tail throughout the maneuver.
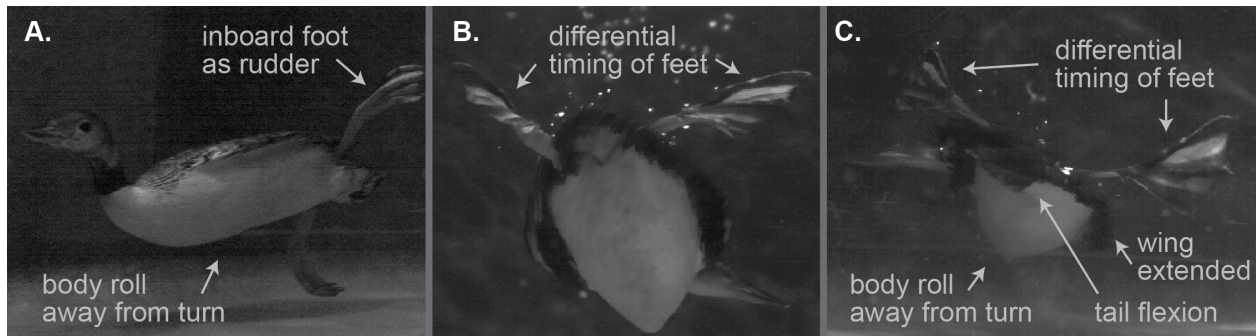
Figure 4.7: Observed turning strategies of loons. Still shot frames from three trials depict strategies that loons use to turn. (A) A loon makes a left turn using its inner, left foot as a rudder and rolling its body away from the turn. (B) Turning to the right, a loon varies the timing of its feet. The outboard, left foot began its power stroke earlier and has reached a point behind the loon while the inboard, right foot has only traveled halfway through its power stroke. Though difficult to view from this camera angle, the loon body rolls away from the turn. (C) A loon makes a sharp turn to the left by varying the timing of its feet, extending its outboard wing, and depressing its tail. The body of the loon rolls away from the turn.

While turning, loons paddle the inboard and out-board feet at different times. In contrast, when swimming straight loons synchronously paddle their feet, starting and stopping each foot's power stroke at approximately the same time (Figure 4.8). However, during turns, loons almost always paddled the outboard foot 0.05-0.10 s before the inboard foot (Figure 4.8), representing a temporal difference of 20-40% of power stroke duration. In some cases, loons extended the toes of the inboard foot when it was held lateral to the body, allowing the inboard foot to act as a rudder. In two trials, the use of the inboard foot as a rudder was extended over repeated paddling cycles of the outboard foot (Figure 4.8, bottom row).

Figure 4.8: Power stroke timing of feet during straight swimming and turns. The timing of power strokes was tracked in several trials. Lines represent power strokes with gaps indicating recovery strokes of each foot throughout time (x-axis). Loons generally swim with both feet paddling synchronously as seen in the straight swimming trials (black). However, during turns, the outboard foot (light grey) consistently begins its power stroke slightly before the inboard foot (dark grey). The trials displayed here show data from both left and right turns, normalized for inboard and outboard feet. In some cases (shown in bottom trial), the inboard foot was held laterally in a mid-power stroke position, serving as a rudder, while the outboard foot was paddled several times.

Although loons alter the relative timing of the feet when turning, only a few stride parameters varied between straight and turning strides. Without accounting for an influence of speed, no stride parameters showed kinematic variation. However, when accounting for both average swim speed and random effects from individual variation, a few variables demonstrated significant variation (Table 4.2). The inboard foot used a longer power stroke compared to straight swimming strides ($p = 0.007$, Table 4.2, Figure 4.9). Power stroke duration significantly decreased with increased stride speed for every model (Table 4.2). Stride duration also decreased significantly with increasing speed in all models except for when only considering straight and outboard foot strides ($p=0.134$). Lastly, the tip of digit III on the outboard foot traveled a slightly longer, though not significantly, distance throughout the power stroke compared to the inboard foot (23 cm vs. 19 cm, $p > 0.05$),

Figure 4.9: Kinematic parameters for straight swimming and turning strides versus swimming speed. The timing of paddling was calculated for over 100 strides from 19 trials. Body speed was tracked during 23 full strides, corresponding to 46 potential foot paddles. Based on the visibility in the video recordings for each foot paddle, the following kinematic parameters were calculated: (A) power stroke duration, (B) stride duration, and (C) duty factor, or the fraction of the full stride used for the power stroke. Linear mixed effects models were fit to the data incorporating errors from individual variation as well as the impact of speed and foot type category. Statistical analyses were repeated comparing straight (black circles) versus inboard foot (red "x") versus outboard foot (blue "+") data and while binning together inboard and outboard strides as all turning data.

traveling at a higher average speed (1.05 vs. 0.63 m s^{-1}, p = 0.036). To summarize, (1) the stride of the inboard foot lasted longer than for straight swimming strides, (2) faster swimming loons used shorter stride times and particularly power strokes, and (3) turning loons paddled the outboard foot at a faster average velocity.

Across seven turning strides with the hindlimb digitally tracked, loons vary foot motion considerably. Variation among inboard and outboard strides does not permit a precise description of turning kinematics, but our data reveal some consistent kinematic patterns. During straight swimming, the foot arcs caudally, dorsally, and somewhat medially relative to the body through the power stroke (Figure 4.10, center). In contrast, for all turning power strokes the inboard and outboard feet reduced the dorsal component to keep the foot ventral or in line with the ankle (Figure 4.10B). Further, the inboard foot remained caudal to the ankle compared to straight or outboard strides where the foot reaches a lateral or even cranial position relative to the ankle (Figure 4.10A). Two turning strides, one inboard foot (Figure 4.10, right) and one outboard foot (not depicted), included a larger mediolateral excursion than used during straight swimming. Even though several of the turning strides resembled straight swimming motions, variability among turning strides demonstrates the ability of loons to modulate paddling kinematics and reveals a few consistent turning kinematic patterns.

4.5   Discussion

The large territories of loons and their conservation status pose significant challenges for quantifying their underwater swimming kinematics. Working within a rehabilitation center, we collected detailed 3D data from 19 trials across four healthy individuals, representing both straight swimming and turns. By collecting data over three winter seasons, we were able to demonstrate consistent qualitative, as well as quantitative, findings of these exceptional underwater foot-propelled swimming birds. While observing loons in captivity may underestimate their top swimming speeds, it is unlikely that loons adjust their swimming motions and strategies for turning under confined circumstances. Therefore, we believe that our results report the first detailed analysis of natural loon swimming.

Table 4.2: Likelihood ratio tests for linear mixed effects models of loon swimming kinematic parameters. To account for swim-type category, stride body speed, and individual loon variation, linear mixed-error models were applied to kinematic parameters. Swim-type category (straight swimming strides, turning strides tracking the inboard foot, and turning strides tracking the outboard foot) and stride body speed were fixed effects, with loon identity as a random effect. Likelihood ratio tests compared full models to a model with either the swim-type or speed effect removed, calculating a p-value representing the influence of that effect on the kinematic parameter. These values are listed in the table (all non-"n" columns). Bold p-values denote significance using a 0.05 cut-off.

	straight vs. inboard vs. outboard			straight vs. inboard			straight vs. outboard			inboard vs. outboard			straight vs. turning (in- + outboard)		
	n	swim type	speed	n	swim type	speed	n	swim type	speed	n	swim type	speed	n	swim type	speed
Power stroke time (s)	40	1	3.5e-5	28	0.007	2.5e-5	26	1	0.018	26	0.156	6.1e-7	40	1	1.4e-5
Stride time (s)	42	1	0.004	30	1	0.005	28	1	0.134	26	1	0.028	42	1	0.003
Duty factor	40	1	1	28	0.148	0.890	26	1	0.330	26	1	1	40	1	1

124

A. View from above

outboard foot straight trial inboard foot

medial

lateral

intertarsal ankle

metatarsophalangeal joint

digit III

15 cm

B. View from right side

dorsal

ventral

movement direction

travel direction
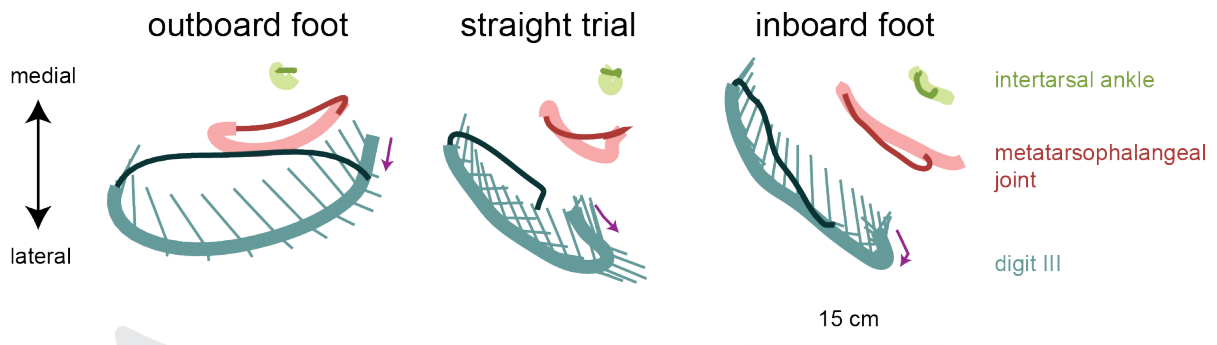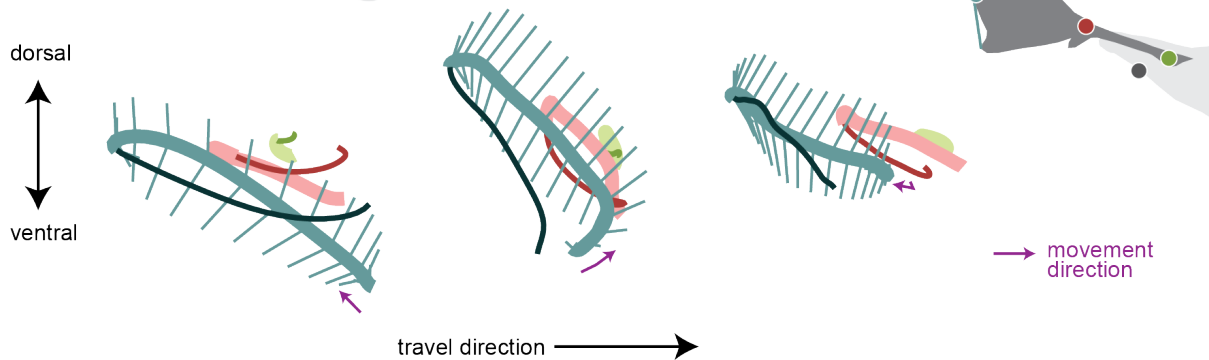
Figure 4.10: Right foot motion with respect to the body during straight swimming and turning. The traces show tracked motion relative to the body from a full stride, including power stroke (bold) and recovery stroke (thin). Strides from three trials show the foot on the outside of the turn (left, "outboard"), the foot while swimming in a straight trajectory (center), and the foot on the inside of the turn (right, "inboard"). The 3D data were rotated to be in reference to the travel direction (x-axis), mediolateral plane (A, y-axis), and dorsoventral plane (B, y-axis) and translated to account for body motion (Note this is a different kinematics representation than Fig. 3, in which the foot kinematics are in relation to the water and not the body's motion). (A) View of the right limb from above the loon showing the intertarsal ankle joint (green), metatarsophalangeal joint (MTP, red), and tip of digit III (blue). Thin, lighter blue lines connect the tip of digit III to the tips of digit II and IV every 3rd frame (0.015 s). (B) View of the right limb from the right side of the loon. All panels scaled to 15 cm scale bar. During the stride for the outboard foot, the loon turned with a radius of curvature (r) of 0.09 m and angular velocity (ω) of 247° s^{-1}. The turn depicted for the inboard foot stride had an r of 0.49 m and ω =75° s^{-1}.

125

4.5.1 Straight swimming

During straight swimming, we record loons reaching speeds up to 0.86 m s^{-1}. Studies analyzing other top foot-propelled swimming birds record faster speeds for straight swimming, 1.2 m s^{-1} in grebes (Johansson and Norberg, 2001) and 1.5-1.7 m s^{-1} in cormorants (Ribak et al., 2004; Watanabe et al., 2011). However, these birds were tracked swimming in the wild or through long straight corridors, unlike the comparatively small pool used in this study. We expect that the pool restricted the loons, and that loons likely reach faster swimming speeds in the wild.

Under the conditions of our study, loons swim using stride frequencies within the range of other foot-propelled swimming birds, but with relatively high values for their body size. When swimming straight, loons use an average stride frequency of 2.04 Hz, similar to values found for grebes (2.50 Hz; Johansson and Norberg, 2001) and cormorants (1.10-3.25 Hz; Ribak et al., 2004; Ribak et al., 2005; Sato et al., 2007; Watanuki et al., 2005). When only comparing values for birds swimming horizontally in captivity, loons swim with faster stride frequencies than cormorants despite having a larger body mass (2.9 kg vs. 2.2 kg). Scaling patterns observed within and among aquatic swimmers (Sato et al., 2007; Sato et al., 2010) predict that larger animals should use lower stride frequencies. Therefore, despite swimming with stride frequencies within the range of other foot-propelled birds, loons use comparatively fast strides when accounting for body size.

Despite their relatively high stride frequencies, loons swim with longer power strokes compared to other foot-propelled swimming birds. The use of sequential power and recovery strokes in loons is similar to grebes but differ from cormorants, which include a gliding phase with their feet held behind the body before each recovery stroke (Ribak et al., 2005). The power stroke of loons approximates 54% of the stride, lasting on averages 0.26 s during straight swimming. In comparison, the power strokes of both grebes and cormorants constitute 25% of the stride, lasting 0.01 s and 0.16 s respectively (Johansson and Norberg, 2001; Ribak et al., 2004; Ribak et al., 2005). Since we find that power stroke duration significantly decreases with swim speed, the difference between loons and other swimming birds observed to date could result from the comparatively slow swimming speeds of

the loons in the rehabilitation pool used for this study. Finally, loons modulate swim speed primarily by varying their power stroke duration and not stride frequency.

Loons swim by synchronously pushing their feet backward, medially and dorsally during the power stroke, and then drawing the foot forward with collapsed toes during the recovery stroke. However, this paddling is not a simple pivoting motion. The feet begin the power stroke ventral to the body with the plantar surfaces of the feet facing caudally but end with the plantar surfaces facing medially towards each other (Figure 4.4). The ankle and metatarsophalangeal joints primarily function as a hinge (Stolpe, 1935), suggesting that this rotation of the foot must occur more proximally. Loons have a relatively abducted hip joint with a large antitrochanter that restricts rotation of the femur (Hertel and Campbell Jr, 2007; Wilcox, 1952), likely preventing a contribution of the hip joint to foot rotation. Instead, foot rotation likely results from rotation at the knee, as has been demonstrated in running birds (Kambic et al., 2014; Kambic et al., 2015). Loons possess an enlarged cnemial crest at the proximal end of the tibiotarsus, which almost completely encloses the anterior and posterior articular surfaces of the distal femur (Wilcox, 1952). While the cnemial crest limits flexion and extension of the knee, it permits long- axis rotation of the tibiotarsus. Grebes demonstrate a similar anatomical pattern, and also swim using long-axis foot rotation while swimming (Johansson and Norberg, 2001). Therefore, loons probably swim by coupling flexion and extension at the ankle joint with rotation at the knee to achieve the net 3D kinematic propulsive and recovery movements of the foot.

The motion of the foot in swimming loons resembles that of grebes, suggesting that loons may also use lift forces for propulsion. Loons (Figures 4.4, 4.5) and grebes (Johansson and Norberg, 2001) paddle their feet lateral to the body, whereas cormorants paddle their feet ventrally underneath the body (Ribak et al., 2004). Nevertheless, all three underwater swimming species demonstrate almost no motion of the feet opposite to the travel direction, indicating that the feet move very little relative to the surrounding water (Figure 4.5). Because the feet do not substantially push water backward, propulsion cannot depend on drag forces. Instead, loons direct their feet dorsally and medially relative to still water throughout the power stroke. Consequently, this perpendicular

motion relative to their travel direction likely produces drag to resist buoyancy and lift for forward propulsion. Although the foot kinematics of loons resembles that of grebes, grebes possess lobate toes that likely act as individual hydrofoils to increase lift production (Johansson and Norberg, 2000). Instead, the webbed feet of loons may enhance lift by functioning more like "delta wings", as has been suggested for cormorants (Johansson and Norberg, 2003). By relying on lift instead of drag forces for propulsion, loons can produce propulsive forces at any swim speed, whereas drag-based propulsion is limited to slower speed swimming (Vogel, 2008). Thus, despite variation in whether the feet are moved ventral (cormorants) or lateral (grebes and loons) to the body, three independent lineages of foot-propelled swimming birds indicate the probable use of lift-based propulsion.

Contrary to previous findings (Jimenéz Ortega, 2005), we observed that swimming loons bob their head, likely to enhance their vision. Dozens of bird species across the avian phylogeny exhibit head-bobbing while walking, flying, or swimming (Jimenéz Ortega, 2005; Wallman and Letelier, 1993). Head-bobbing consists of thrust and hold phases, allowing head (and eye) motion to be dissociated from motion of the body (Necker, 2007). The thrust phase accelerates the head (and eyes) forward relative to the body's motion. The hold phase then allows the head (and eyes) to be held briefly in place, stabilizing the bird's gaze. Head-bobbing has been argued to improve vision by increasing depth perception through parallax during the thrust phase, followed by pattern and motion identification during the hold phase (Necker, 2007; Wallman and Letelier, 1993). Prior to our findings, loons were reported not to use head-bobbing (Jimenéz Ortega, 2005). Yet, we find clear evidence of head-bobbing when loons swim underwater, accelerating their head (and eyes) more than three times faster than their body (Figure 4). The use of head-bobbing while voluntarily diving but not during escape dives suggests its possible use for localizing and pursuing prey. Two other foot-propelled diving birds, grebes (Gunji et al., 2013) and mergansers (Lindroth and Bergstöm, 1959), have also been observed to head-bob. Our observation of head-bobbing in loons suggests that this behavior may be broadly representative of foot-propelled diving birds, including groups previously considered not to head-bob, such as cormorants. Because head-bobbing likely enhances vision for hunting prey, it may represent an important function of the comparatively long necks of foot-propelled diving birds.

4.5.2 TURNING STRATEGIES

Previous studies of foot-propelled swimming birds have focused on swimming through a tunnel or navigating a single vertical obstacle (Johansson and Norberg, 2001; Ribak et al., 2004; Ribak et al., 2008). Our study is the first to analyze turning maneuverability of a freely diving foot-propelled bird. Although our findings may not represent the extreme abilities of loons to turn when swimming in the wild due to the confined nature of the swimming pool, we were able to observe maneuvers that likely approach high-level loon turning performance.

Compared to other underwater swimmers, loons execute tight turns but at slow speeds. The minimum radius of curvature observed (0.06 m or 0.07 body lengths (L); Figure 4.2), was significantly smaller than other diving animals, including sea lions (0.16 m or 0.09 L), penguins (0.14 m or 0.24 L), and cetaceans (0.19 m or 0.15 L) (Fish, 2002; Fish et al., 2003; Hui, 1985). Even so, as a measure of maneuverability, turning curvature does not alone characterize turning performance. The angular rate of change in heading direction serves as a measure of agility, and also influences the ability to capture prey. Loons execute turns at up to 287 degrees s^{-1}, more slowly than the maximum rates in sea lions (690 degrees s^{-1}) and penguins (576 degrees s^{-1}), but comparable to dolphins (Fish, 2002), turtles (Rivera et al., 2006) and some teleost fish (average 140-180 degrees s^{-1}; Webb and Fairchild, 2001). However, due to the relatively slow swimming speeds that we observed, loons turn with a centripetal acceleration (0.02 g) much lower than sea lions (5.13 g) or cetaceans (3.56 g). The ability of loons to perform sharp but slow turns compared with other underwater hunters may highlight differences in hunting strategy. Sea lions, penguins, and cetaceans typically hunt in open water requiring them to out-chase their prey. Loons primarily search for prey on the ocean or lake floor, often probing along rocks then quickly snatching any flushed animals (Johnsgard, 1987). This strategy relies on maneuvering in relatively tight spaces, but at slow speeds until quickly accelerating to capture a fish at close range. Additionally, a potentially important difference between loons and all previously studied turning animals is their long and flexible neck. Limitation to their body's turning ability may not adequately reflect the effective capacity for loons to rotate their head for prey capture. Hunting strategies

of loons or other long-necked diving birds has not been quantitatively studied, suggesting an important future direction of this work.

To turn underwater, loons must create a force differential between the sides of their body or redirect the force produced by the feet to produce a swimming torque that rotates the body. There are three main ways that this can be achieved. First, loons could produce stronger propulsive forces on the outboard side relative to the inboard side of the turn. Second, loons can vary the relative timing of force production by each foot. Third, loons could control a turn by redirecting the propulsive forces by altering individual motion of the feet. The following section examines evidence for these turning strategies.

To alter the force produced on each side of the body, loons increase the speed of the outboard relative to the inboard foot. The force each foot produces during the power stroke depends on foot area (abduction of the digits) and speed (influenced by both duration of the power stroke and distance traveled by the foot). Due to individual variation and the limited number of turning trials with the foot tracked, no significant evidence was found for more abducted digits on the outboard versus inboard foot. However, loons appear to alter the speed of the outboard foot during the power stroke, modifying both duration and distance relative to still water. Accounting for variation due to swim speed, the power stroke of the outboard foot is significantly shorter than that for the inboard foot during turns (Table B.2). The tip of digit III of the outboard foot travels a slightly longer distance throughout the power stroke (not significant), but moves at a significantly faster speed. In more extreme cases of turning, loons dramatically alter inboard versus outboard forces by only paddling the outboard foot or by inducing a backwards drag-based force using the inboard foot as a rudder. These strategies result in a net force acting to rotationally accelerate the loon's body into the turn.

Loons were also observed to paddle the outboard foot before the inboard foot to help initiate and maintain turning. Paddling the outboard foot first amplifies the temporal difference in force between outboard and inboard sides during the early part of the turn. Any force produced by the outboard foot is transmitted to the body at a point lateral to the bird's center of mass. Without an equal but counteracting force from the inboard foot,

the thrust from the outboard foot produces a yaw torque (a rotation around the dorsoventral axis of the bird) into the turn. As the body rotates, the center of mass moves towards the inboard foot, reducing and potentially inverting the yaw moment arm of the inboard foot. The force from the delayed inboard power stroke would then act behind or even outside of the center of mass to sustain the turn.

Our observation that the loon's body rolls outward from the turn is a likely consequence of the temporal offset and differential forces produced by the outboard relative to inboard foot. Loons experience upward buoyant forces at shallow depths, as evidenced by their tendency to ascend passively. In order to resist buoyancy, each foot must produce a downward force component. Because loons swim with a slight head-down tilt of the body, their center of mass lies below their feet. When the outboard foot paddles earlier and with a greater force than the inboard foot, the downward vertical component of its force acts on the body above and lateral to the center of mass, producing an upward pitch moment and an outward roll moment. As a result, the ventral belly of the loon rotates in toward the turn. Any downward force from the inboard foot will oppose this roll and stabilize the body. In some cases, loons were observed to slightly extend the outboard wing, which would also help to stabilize the body about its roll axis. Many underwater swimmers, including most cetaceans and sea lions, roll into turns to exploit back flexion to increase maneuverability (Fish, 2002; Fish et al., 2003). However, beluga whales and penguins roll out of turns like loons (Fish, 2002; Hui, 1985). The difference in this behavior has not been previously explained. Our results indicate that differences in body roll during a turn likely relates to turning forces being produced behind (as in loons) versus in front of the body's center of mass.

Turning loons also adjust the 3D motion of their feet to minimize body roll and reduce forces that oppose the turn. While turning, both feet demonstrate a decreased ventral to dorsal component of motion compared to straight swimming (Figure 4.10). With the body rolled away from the turn, any ventrally-directed force will point into the turn. Because the forces produced by the feet act on the body behind the center of mass, these ventral forces would induce adverse yaw moments that resist the turn. Reducing ventrally-directed forces therefore serves to both minimize body roll and limit forces that resist turning. Loons also shift the inboard foot caudally and

increase its lateral to medial motion. This backward and medial motion of the inboard foot likely generates a drag reaction force pointing forward and into the turn, but may also produce a lift force directed forward and away from the turn, as shown for canoeing with a "wing" blade (Jackson and Locke, 1992). Further, if the mediolateral component of lift exceeds that of drag, the net force from the inboard foot will point away from the turn and produce a yaw moment enhancing turn acceleration.

4.6 Conclusions

Loons rely on swimming for hunting, mating, and predator evasion. As one of several independent lineages of adept foot-propelled swimming birds, loons provide critical insight into the physical demands, control strategies, and evolutionary drivers of swimming. We find that loon swimming resembles that of grebes and likely depends on lift generation for propulsion. Loons modulate the duration of the power stroke when varying swim speed and use head-bobbing to enhance underwater vision. Our findings suggest that loons produce propulsive swimming forces convergently to grebe strategies, but diverge from cormorants, which retain the ability to walk on land. As the first study to analyze turning in freely swimming foot-propelled birds, we find that loons use a combination of mechanisms to execute turns. Loons increase the speed of the outboard foot, shift the timing of the outboard power stroke to before that of the inboard foot, and vary the individual motions of the inboard versus outboard feet to turn while swimming underwater. These results may provide inspiration for the design and control of swimming robots, with further application to paddling sports.

Table 4.3: List of abbreviations

a_c	average horizontal centripetal acceleration acting throughout a stride
g	gravitational acceleration, 9.80655 m s^{-2}
MTP	metatarsophalangeal joint
r	average horizontal radius of curvature throughout a stride
TMT	tarsometatarsus
u	average horizontal velocity throughout a stride
ω	average angular velocity throughout a stride

4.7 REFERENCES

Abourachid, A. (2001). Kinematic parameters of terrestrial locomotion in cursorial (ratites), swimming (ducks), and striding birds (quail and guinea fowl). Comp. Biochem. Physiol. A. Mol. Integr. Physiol. 131, 113-119.

Barr, J. F. (1996). Aspects of Common Loon (Gavia immer) feeding biology on its breeding ground. Hydrobiologia 321, 119-144.

Baudinette, R. V. and Gill, P. (1985). The energetics of "flying" and "paddling" in water: locomotion in penguins and ducks. J. Comp. Physiol. B 155, 373-380.

Blake, R. W. (1981). Mechanics of drag-based mechanisms of propulsion in aquatic vertebrates. Symp. Zool. Soc. London 48, 29-52.

Chinsamy, A., Martin, L. D. and Dobson, P. (1998). Bone microstructure of the diving Hesperornis and the voltant Ichthyornis from the Niobrara Chalk of western Kansas. Cretac. Res. 19, 225-235.

Fish, F. (1996). Transitions from Drag-based to Lift-based Propulsion in Mammalian Swimming. Am. Zool. 36, 628-641.

Fish, F. E. (2002). Balancing Requirements for Stability and Maneuverability in Cetaceans. 42, 85-93.

Fish, F. E. and Nicastro, A. J. (2003). Aquatic turning performance by the whirligig beetle: constraints on maneuverability by a rigid biological system. J. Exp. Biol. 206, 1649-1656.

Fish, F. E., Hurley, J. and Costa, D. P. (2003). Maneuverability by the sea lion Zalophus californianus: turning performance of an unstable body design. J. Exp. Biol. 206,.

Grémillet, D., Chauvin, C., Wilson, R. P., Le Maho, Y. and Wanless, S. (2005). Unusual feather structure allows partial plumage wettability in diving great cormorants Phalacrocorax carbo. J. Avian Biol. 36, 57-63.

Gunji, M., Fujita, M. and Higuchi, H. (2013). Function of head-bobbing behavior in diving little grebes. J. Comp. Physiol. A. Neuroethol. Sens. Neural. Behav. Physiol. 199, 703-709.

Hertel, F. and Campbell Jr, K. E. (2007). The antitrochanter of birds: form and function in balance. Auk 124, 789-805.

Hui, C. A. (1985). Maneuverability of the Humboldt penguin (Spheniscus humboldti) during swimming. Can. J. Zool. 63, 2165-2167.

Jackson, P. and Locke, N. (1992). The hydrodynamics of paddle propulsion. Proc. 11th Australasion Fluid Mech. Conf.

Jimenéz Ortega, L. (2005). Avian visual perception: interocular and intraocular transfer and head-bobbing behaviour in birds.

Johansson, L. C. and Norberg, U. M. (2000). Asymmetric toes aid underwater swimming. Nature 407, 582-3.

Johansson, L. and Norberg, U. M. (2001). Lift-based paddling in diving grebe. J. Exp. Biol. 204, 1687-96.

Johansson, L. and Norberg, R. (2003). Delta-wing function of webbed feet gives hydrodynamic lift for swimming propulsion in birds. Nature 424, 65-68.

Johnsgard, P. A. (1987). Diving Birds of North America. Lincoln, Nebraska: University of Nebraska Press.

Kambic, R. E., Roberts, T. J. and Gatesy, S. M. (2014). Long-axis rotation: a missing degree of freedom in avian bipedal locomotion. J. Exp. Biol. 217, 2770-2782.

Kambic, R. E., Roberts, T. J. and Gatesy, S. M. (2015). Guineafowl with a twist: asymmetric limb control in steady bipedal locomotion. J. Exp. Biol. 218, 3836-3844.

Lindroth, A. and Bergstöm, E. (1959). Notes on the feeding technique of the Goosander in streams. Inst. Freshw. Res. 40, 165-175.

Miller, R. E. and Fowler, M. E. (2014). Fowler's Zoo and Wild Animal Medicine. Volume 8. St. Louis, Missouri: Elsevier Health Sciences.

Necker, R. (2007). Head-bobbing of walking birds. J. Comp. Physiol. A. Neuroethol. Sens. Neural. Behav. Physiol. 193, 1177-1183.

Nocera, J. J. and Burgess, N. M. (2002). Diving schedules of Common Loons in varying environments. Can. J. Zool. 80, 1643-1648.

Ribak, G., Weihs, D. and Arad, Z. (2004). How do cormorants counter buoyancy during submerged swimming?

J. Exp. Biol. 207, 2101-2114.

Ribak, G., Weihs, D. and Arad, Z. (2005). Submerged swimming of the great cormorant Phalacrocorax carbo sinensis is a variant of the burst-and-glide gait. J. Exp. Biol. 208, 3835-3849.

Ribak, G., Weihs, D. and Arad, Z. (2008). Consequences of buoyancy to the maneuvering capabilities of a foot-propelled aquatic predator, the great cormorant (Phalcrocorax carbo sinensis). J. Exp. Biol. 211, 3009-3019.

Rivera, G., Rivera, A. R. V., Dougherty, E. E. and Blob, R. W. (2006). Aquatic turning performance of painted turtles (Chrysemys picta) and functional consequences of a rigid body design. J. Exp. Biol. 209, 4203-4213.

Sato, K., Watanuki, Y., Takahashi, a., Miller, P. J. ., Tanaka, H., Kawabe, R., Ponganis, P. J., Handrich, Y., Akamatsu, T., Watanabe, Y., et al. (2007). Stroke frequency, but not swimming speed, is related to body size in free-ranging seabirds, pinnipeds and cetaceans. Proc. R. Soc. B Biol. Sci. 274, 471-477.

Sato, K., Shiomi, K., Watanabe, Y., Watanuki, Y., Takahashi, A. and Ponganis, P. J. (2010). Scaling of swim speed and stroke frequency in geometrically similar penguins: they swim optimally to minimize cost of transport. Proc. Biol. Sci. 277, 707-714.

Schorger, A. (1947). The Deep Diving of the Loon and Old-Squaw and Its Mechanism. Wilson Bull. 59, 151-159.

Sidor, I. F., Pokras, M. A., Major, A. R., Poppenga, R. H., Taylor, K. M. and Miconi, R. M. (2003). Mortality of common loons in New England, 1987 to 2000. J. Wildl. Dis. 39, 306-315.

Stolpe, M. (1935). Colymbus, Hesperornis, Podiceps: ein Vergleich ihrer hinteren Extremitát. J. fur Ornithol. 83, 115-128.

Taubin, G. (1991). Estimation of planar curves, surfaces, and nonplanar space curves defined by implicit equations

with applications to edge and range image segmentation. IEEE Trans. Pattern Anal. Mach. Intell. 13, 1115-1138.

Theriault, D. H., Fuller, N. W., Jackson, B. E., Bluhm, E., Evangelista, D., Wu, Z., Betke, M. and Hedrick, T. L. (2014). A protocol and calibration method for accurate multi-camera field videography. J. Exp. Biol. 217, 1843-1848.

Vogel, S. (2008). Modes and scaling in aquatic locomotion. Integr. Comp. Biol. 48, 702-12.

Wallman, J. and Letelier, J.-C. (1993). Eye movements, head movements, and gaze stabilization in birds. In Vision, brain, and behavior in birds (ed. Zeigler, H. P.) and Bischof, H.-J.), pp. 245-263. Cambridge, MA: The MIT Press.

Watanabe, Y. Y., Takahashi, A., Sato, K., Viviant, M. and Bost, C.-A. (2011). Poor flight performance in deep-diving cormorants. J. Exp. Biol. 214, 412-421.

Watanuki, Y., Takahashi, A., Daunt, F., Wanless, S., Harris, M., Sato, K. and Naito, Y. (2005). Regulation of stroke and glide in a foot-propelled avian diver. J. Exp. Biol. 208, 2207-2216.

Webb, P. W. and Fairchild, A. G. (2001). Performance and maneuverability of three species of teleostean fishes. 1877, 1866-1877.

White, C. R., Martin, G. R. and Butler, P. J. (2008). Pedestrian locomotion energetics and gait characteristics of a diving bird, the great cormorant, Phalacrocorax carbo. J. Comp. Physiol. B. 178, 745-754.

Wilcox, H. H. (1952). The Pelvic Musculature of the loon, gavia immer. Am. Midl. Nat. 48, 513-573.

Wildlife Action Plan (2015).

Zinoviev, A. V. (2011). Notes on the hindlimb myology and syndesmology of the Mesozoic toothed bird Hesperornis regalis (Aves: Hesperornithiformes). J. Syst. Palaeontol. 9, 65-84.

5

Robotic loon demonstrates that foot-based swimming birds produce lift

5.1 ABSTRACT

Loons traditionally have been considered to power swimming through less efficient drag forces rather than lift forces despite their ability to dive to great depths and reach fast swimming speeds. Aquatic force production in foot-propelled swimming birds has never been definitively measured, with past methods ignoring unsteady components of fluid forces or simplifying foot motion. Here we take a novel approach, robotically actuating real loon feet to accurately replicate the 3D kinematics of freely swimming loons, allowing the first direct measurement of

swimming forces. We find that loons generate significantly greater lift than drag, and direct a large component of force dorsally towards the loon's back to counter buoyancy. Our findings challenge historical perceptions of animal swimming performance and identify a previously overlooked group of animals to serve as inspiration for aquatic robotic design.

5.2 Main Text

Despite having evolved from flying ancestors, several independent lineages of birds excel at swimming. Since many adaptations for flight impede efficient swimming (Lovvorn and Jones, 1994), aquatic birds exhibit particularly effective mechanisms for producing force underwater. Birds that flap their wings to propel swimming (such as penguins) produce "lift" forces (Baudinette and Gill, 1985), which act perpendicular to the flapping motion to power forward swimming. Conversely, birds that paddle their feet (such as ducks and cormorants) are traditionally considered drag-based (Vogel, 2008), producing "drag" forces that act opposite to foot backward motion to power forward swimming. But to produce drag the foot must move backwards relative to still water, limiting swimming speed based on the foot's backward speed relative to the body. In addition to restricting swim speed (Walker and Westneat, 2000), drag-based swimming is less energetically efficient (Alexander, 2003). Yet, many foot-propelled swimming birds reach high swimming speeds (up to 1.7m/s in cormorants; (Ribak et al., 2004; Watanabe et al., 2011)) and dive to deep depths (Quintana et al., 2007; Schorger, 1947). The exceptional swimming abilities of these foot-propelled diving birds challenge a traditional drag-based paradigm, suggesting that foot-based swimmers may generate lift or use novel unsteady fluid dynamics mechanisms.

Some past studies suggest that foot-propelled diving birds may generate lift. This assertion arises from qualitative analysis of paddling movements (Johansson and Norberg, 2000; Johansson and Norberg, 2001), theoretical fluid force calculations assuming two-dimensional foot motion (Ribak et al., 2004), and flow visualization around a simple physical model (Johansson and Norberg, 2003). While insightful, these methods by necessity oversimplify foot motion or overlook unsteady hydrodynamics like foot acceleration. Furthermore, current

methodologies for experimentally measuring fluid forces of live swimming animals, such as Digital Particle Image Velocimetry, are often two-dimensional and require the use of small animals that exhibit consistent, repetitive behaviors in the lab (Westerweel et al., 2013). Consequently, it remains unclear if and how foot-propelled diving birds generate lift forces.

Given these limitations, we developed a robotic approach to directly measure fluid forces produced by known 3D foot motions of a diving bird swimming underwater, focusing on the Common loon (*Gavia immer*). Loons are highly specialized swimmers capable of diving hundreds of feet (Schorger, 1947) and remaining underwater for minutes at a time (Nocera and Burgess, 2002), therefore serving as an ideal subject for understanding swimming in diving birds. Here we program an industrial robot to replicate the 3D foot motion recorded from wild loons swimming in a pool (see Materials and Methods). A force sensor attached to the robot measured time-varying forces acting on the left foot of seven common loons during the power stroke. The robotic method presented here demonstrates a clear advantage to past methodologies and enables direct measurement of time-resolved lift and drag forces generated by swimming loons, representing the most accurate assessment of swimming forces in naturally behaving birds.

We replicated the foot motion of freely-swimming loons relative to still water with an average offset of 4 mm throughout the programmed motion. Accounting for the influence of gravity, buoyancy, and inertia, we record and isolate the fluid forces generated due to the foot's movement, including both steady and unsteady components. We decomposed the forces acting on the loon foot relative to (1) the anatomical axes of the swimming loon and (2) the foot's motion, representing drag and lift.

The foot motion of swimming loons can be separated into two phases. During the power stroke phase, both feet push backwards in a lateral arc with the digits extended and abducted. During the recovery phase, the toes collapse behind the tarsometatarsus and the whole foot returns to its forward position. Propulsive force is produced during the power stroke. We find that loon feet generate the highest forces during the middle of the power stroke with the feet slightly behind the body traveling medially and dorsally (Figure 5.1A). Most of this force

A. Force relative to body

B. Force relative to foot motion
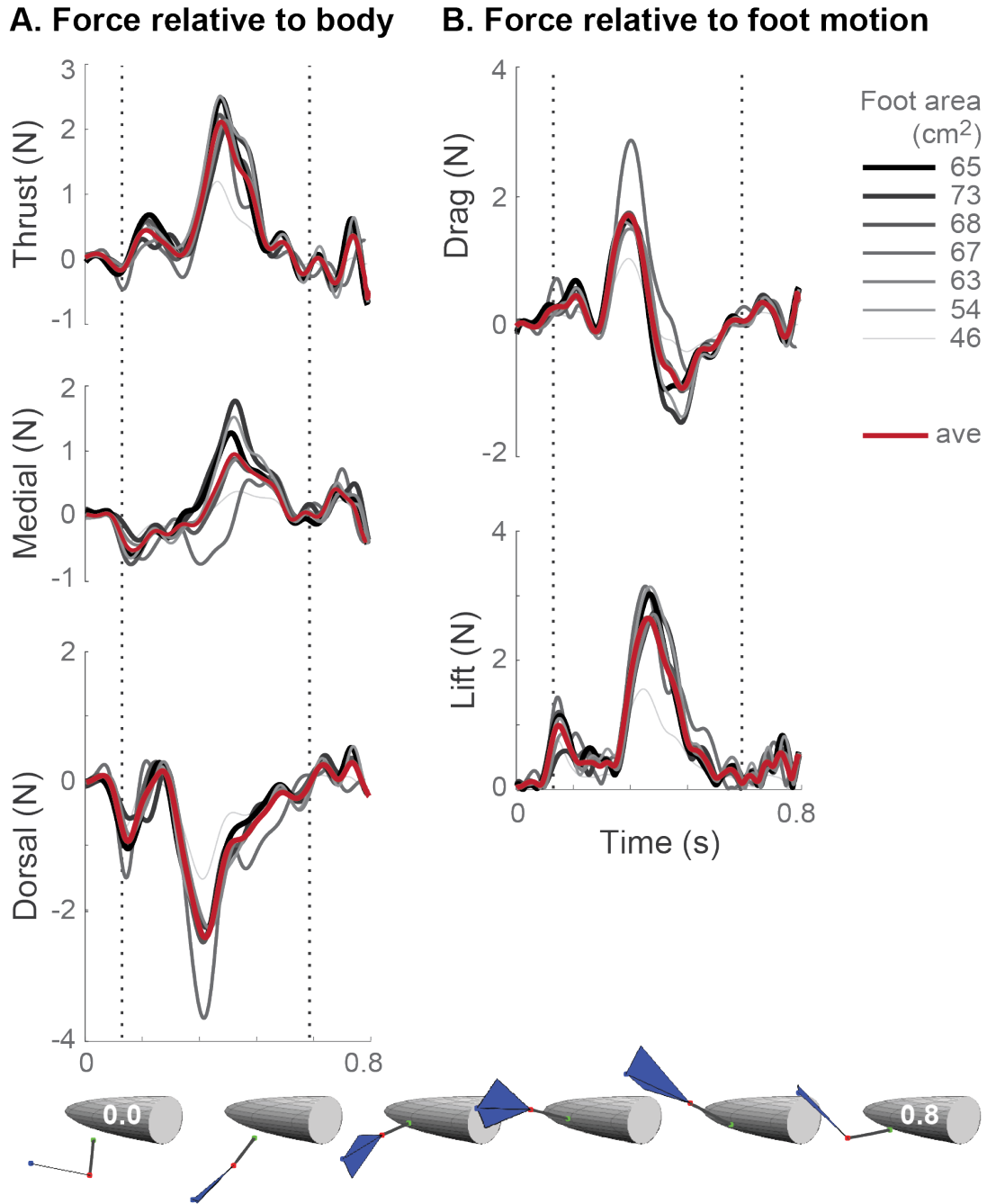
Figure 5.1: Swimming forces exerted on all loon feet at the fastest robot speed, 2.2 times slower than the loon. Forces recorded by a force sensor throughout the motion were decomposed (A) relative to the body of the loon and (B) relative to the motion of the foot. Thrust acts in line with the body swimming direction, Medial forces act towards the body midline, and Dorsal forces act towards the loon's back opposing gravity. Drag (not body drag) is all force in the direction opposite of foot motion and Lift is defined as all remaining force, in the plane perpendicular to foot motion. The programmed robotic motion lasted approximately 0.8 s, on the x-axis. The swimming schematic shows the foot position (using a R foot for visual clarity) throughout the actuated movement. Vertical dashed lines demark the beginning and end of the power stroke. Each gray line represents an average over 15 trials for one foot, with line thickness and color corresponding to loon body mass. The red line shows the average for all feet.

contributes to thrust, with a slightly smaller component directly ventrally. When swimming horizontally, this ventral component opposes upward buoyancy to likely control the loon's depth. Early in the power stroke, loons generate a small lateral force as the toes abduct. During the middle and late power stroke, the foot produces a medially directed force. These mediolateral forces would be counteracted by the opposing foot during straight swimming, but would also be effective for turning.

We find that loons swim by producing more lift than drag (Figure 5.1B). Drag peaks during the first half of the power stroke as the foot pushes backwards and the toes extend. Lift peaks during mid-power stroke as the foot arcs medially and dorsally. Without flow visualization, the mechanisms for lift production remain unknown. However, the triangular-shaped webbed foot may function as a delta-wing to produce lift, as has been observed when actuating a triangular plate similar to cormorant swimming (Johansson and Norberg, 2003). Delta-wings induce leading edge vortices along two edges, generating lift even at slow speeds if at a high angle of attack (Gursul, 2004).

During the second half of the power stroke, loon feet experience force acting in the direction of foot motion, represented in Figure 5.1 as negative drag values. By definition drag cannot be negative, but this behavior could result from two potential causes. First, these negative drag forces coincide with foot deceleration, suggesting that unsteady fluid forces, such as acceleration reaction, may be occurring. Second, the peak in lift production just precedes the negative drag values, suggesting that the associated circulation around the foot may contribute to this unusual behavior.

We robotically replicated loon feet at eight speeds slower than normal loon swimming allowing for extrapolation to real swimming speeds. We find that loons may generate peak lift forces of ~22 N and peak drag forces of ~6 N (Figure 5.2). These values resemble those calculated using a 2D hydrodynamics model for similarly-sized great cormorants (1.5-5 kg): 17 N lift, 3 N drag, and 9 N inertia (Ribak et al., 2004). However, the cormorant model was based on experimental kinematic data of a cormorant swimming at 1.5 m/s, whereas the robot in this study replicated a loon swimming in a pool at an average 0.5 m/s. Since a confined pool space restricts swimming

speed, common loons in the wild likely produce stronger swimming forces than the values reported here or previ-

ous estimates for other foot-propelled diving birds.
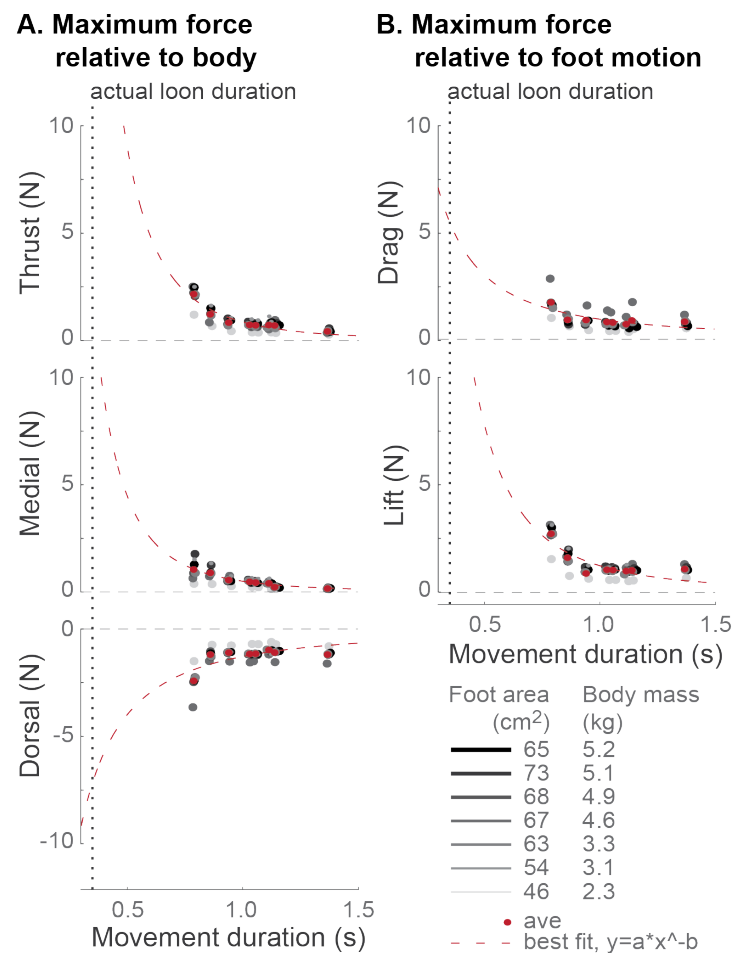
Figure 5.2: Maximum swimming force versus movement duration for all loon feet. Forces recorded by a force sensor throughout the actuated, robotic motion were decomposed (A) relative to the body of the loon and (B) relative to the motion of the foot (see Figure 5.1 caption for more detail). Each gray data point represents the peak force experienced throughout the actuated swimming movement averaged over 15 trials. Data point color is determined by loon body mass. Red dots depict the average across all loon feet for each actuated movement program. A best-fit line (dashed, red) extrapolates the recorded robotic data to the movement duration observed in live loons (0.35 s, vertical dashed line).

Patterns in force production were consistent across loon feet, but foot size and webbing stiffness influence the

magnitude of propulsive forces. We recorded the forces acting on feet from seven loons, ranging in body mass

from 2.3 to 5.2 kg and in foot surface area from 46 to 73 cm2. While force production generally increased with in-

creasing foot area (Figure 5.1), neither the foot from the largest loon or the foot with the largest surface area generated the largest forces. These forces were instead produced by a foot with qualitatively stiff webbing. Two of the seven loon feet possessed stiffened webbing. One, as discussed previously, produced the largest forces recorded. The other foot, from a loon with a body mass of 3.1 kg, generated forces comparable to the feet from the two largest loons (both at over 5 kg). The determinants of webbing skin stiffness remain unknown, with potential factors including age (Diridollou et al., 2001), seasonality (Nam et al., 2015), and injury (Corr and Hart, 2013). However, since webbing stiffness influences force production, understanding its physiological and environmental basis in waterbirds may inform conservation efforts.

Discrepancies between real loons swimming and our robotic methodology likely do not influence the results presented here. Although the robotic measurements do not account for fluid interactions from the body or other foot, the body of loons is streamlined and the foot remains lateral to the body throughout most of the power stroke. A second potential disparity relates to a loon's ability to muscularly control toe abduction, not represented in our passive actuation. However, toe abduction in freely swimming loons is primarily passive since the muscles that power digit extension are much reduced compared to the many, large toe flexors (Wilcox, 1952). Instead, loons rely on skeletal flanges at the base of each digit that couple the extension of adjacent toes (Stolpe, 1935). Despite these factors, our force measurements represent the most accurate estimation to date of swimming forces in foot-propelled diving birds.

We reveal that loons primarily power swimming through lift forces, overturning a long-standing classification of foot-propelled swimmers as drag-based. Although previously considered less efficient or adept than traditional lift-based swimmers, foot-propelled animals may exhibit novel mechanisms for effectively producing underwater forces. These mechanisms may inspire designs for amphibious robots (Dudek et al., 2007; Kato, 2011) and unveil new principles of underwater locomotion.

5.3   Materials and Methods

5.3.1   Loon kinematics

Between 2014 and 2016, four healthy common loons (*Gavia immer*) were filmed at the Tufts Wildlife Clinic. Loon swimming was filmed using two high-speed cameras (NR5S1, Integrated Design Tools, Tallahassee, FL, USA) in an indoor, 3.05 m diameter pool. The cameras were placed in custom-made underwater cases using adapted scuba dive boxes and 80/20 aluminum framing. A wide-angle lens was attached to each camera (14mm, f/3.2, Rokinon) and focused at a distance of 1.8 m in air. The effective lens focal length increases when submerged resulting in an approximate in-focus depth of field of 1.3-2.7 m from the camera.

Of the 159 trials recorded of the four loons, six were suitable for analyzing hindlimb motion in detail. These six trials contained 10 tracked strides, three representing straight swimming. The kinematic patterns were generally consistent among strides, though the stride depicting an intermediate between the other two was chosen as the representative swimming stride. Body motion was tracked using a feather coloration pattern at the midline of the caudal abdomen near the vent. Loons tuck the proximal hindlimb within the skin overlying the abdomen, therefore preventing observation of the hip and knee joints. The right distal hindlimb was tracked using five landmarks: intertarsal "ankle" joint, metatarsophalangeal joint (MTP), and distal phalanx of digits II-IV. The left ankle was also tracked (Figure 5.3). The tracked three-dimensional (3D) motions of the body and hindlimb were smoothed and rotated relative to the body of the loon. Custom MATLAB scripts applied a cubic spline (smoothing parameter = 0.01) to the data. The relatively extreme smoothing parameter derives from a high frame rate relative to motion speed. Rotation matrices were defined and applied at each time-step based on trajectory-based and anatomical axes. The x-axis was defined as the travel direction of the body. The y-axis corresponds to the line connecting the left and right ankle joints, representing the mediolateral plane of the bird assuming symmetrical or limited motion of the ankles relative to the body. The z-axis was calculated as the cross product of the x- and y- axes, approximating the dorsoventral plane of the body. The resulting data represents how the foot moves

relative to still water described by the anatomical axes of the loon.
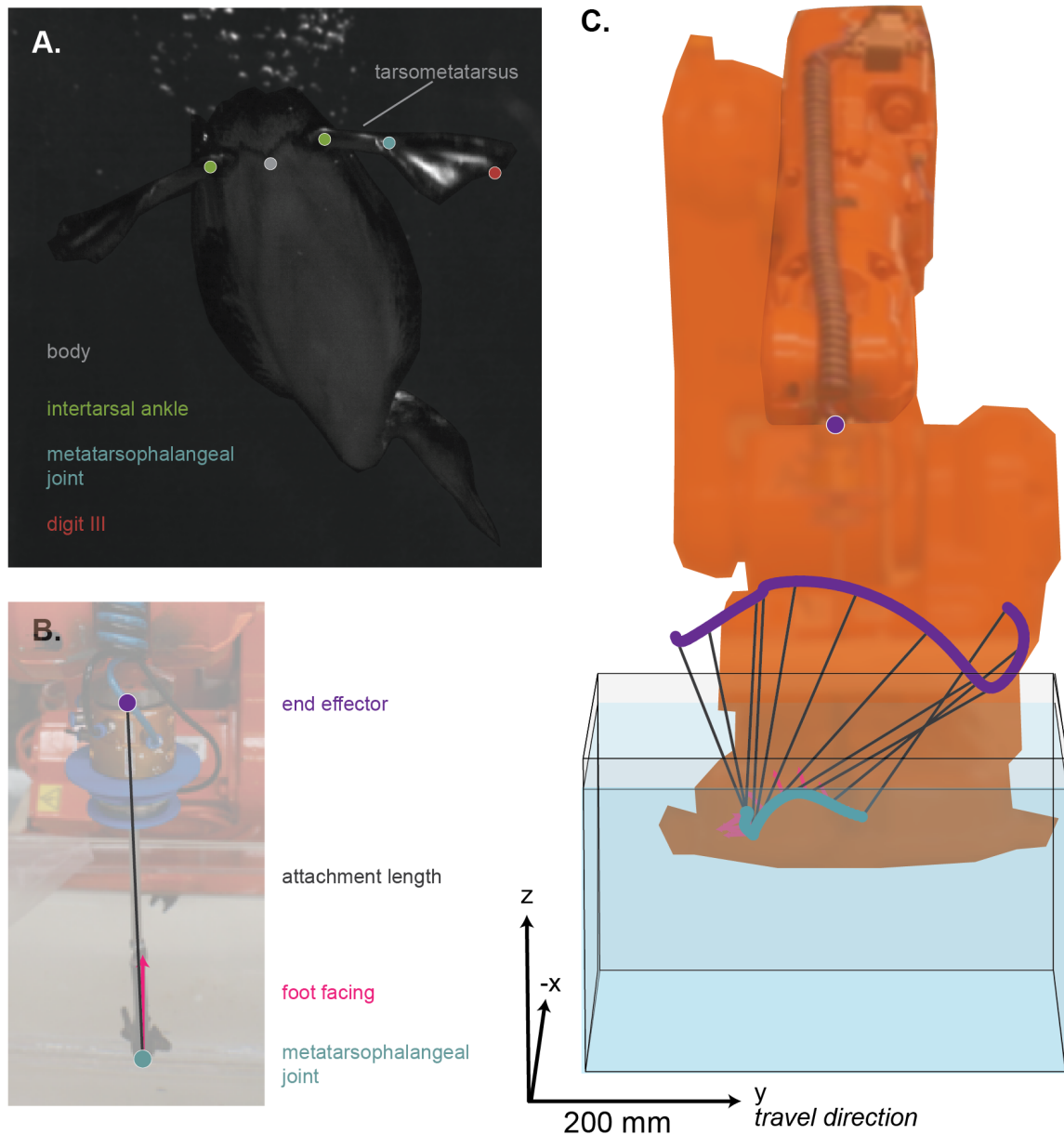
Figure 5.3: Loon tracking and robot set-up. (A) A common loon was filmed at 200 fps, and several landmarks on the body and limb tracked. These data were used to describe how the foot of the loon moves relative to still water while swimming horizontally. (B) Seven cadaveric feet were attached to the robot at an attachment length of 25 cm from the end effector. The attachment length includes a tool changer, force sensor (ATI mini45), custom 3D-printed attachment plates (blue), and a stainless steel standoff. (C) The ABB IRB 140 robot was programmed to actuate the cadaveric foot in the motion of the swimming loon by positioning the end effector (purple) at several points along a kinematic trace. The blue trace represents the position of the metatarsophalangeal joint (MTP) throughout the movement, with pink arrow depicting the facing of the foot (defined using the vectors from the ankle to the MTP and from the MTP to the tip of digit III). A custom acrylic aquarium was built for the experiment to enable robot movement while reducing water volume and therefore tank weight.

5.3.2 ROBOT PROGRAMMING IN MATLAB

The three dimensional (3D) kinematics of one power stroke was used to program the robot. The foot motion of swimming loons can be separated into two phases. During the power stroke phase, both feet push backwards with the digits expanded. During the recovery phase, the toes collapse behind the tarsometatarsus and the whole foot returns to its forward position. Propulsive force is produced during the power stroke, which is therefore the primary focus for robot actuation. A 0.35 s section of loon swimming kinematics was used to program the robot. This section included a straight swimming power stroke, with a buffer both before and after of 0.04 s. A longer section was not favored in order to reduce the excursion of the foot and robot.

We selected the ABB IRB 140 industrial robot due to its reach envelope, high-speed capacity, and relatively small size. This model was available for use in the Harvard Graduate School of Design Fabrication Lab (Cambridge, MA).

The tracked motion of the loon's right foot was modified for compatibility with the robot in five steps: (1) converting the right foot data to represent the left foot, (3) rotating the data to work within an aquarium, (3) finding the facing of the foot at each time point, (4) defining the rotated facings using quaternions, and (5) calculating the necessary motion of the robot hand to replicate the motion of the foot using a spacer.

Only left feet were available for use with the robot. Mediolateral values were therefore multiplied by -1 in order to invert the tracked kinematic loon data to represent the motion of the left foot.

Loon kinematics data were rotated for actuation within an aquarium. Loons swim with their feet directed laterally. In order to actuate this motion within an aquarium without submerging the robot, the data must be rotated for actuation from above. All potential rotation angles around the travel direction of the loon (x-axis of the robot workspace) were tested and the maximum vertical position of the MTP and the minimum vertical position of the robot hand measured. To prevent water damage to the robot, rotation angles were judged to maximize the distance between the robot and the MTP (and therefore water). The selected rotation was 98 degrees counter-

clockwise around the travel direction.

The loon foot's facing was determined at each tracked time point. While swimming, loons do not solely rotate the foot at the ankle, but also incorporate a rotation at the knee joint. The resulting 3D orientation of the foot throughout the power stroke likely plays an important role in producing force. To accurately replicate foot swimming motion, the facing of the foot was calculated over the course of the full programmed foot movement. The facing was defined as the vector directed away from the plantar surface of the foot perpendicular to the tarsometatarsus. Determining the facing of the foot occurred in two stages. First, a vector, p, was defined as the cross product of (m) the vector from the MTP to the ankle joint and (n) the vector from the MTP to the tip of digit III. Second, the facing vector was calculated by crossing vector p with vector m. This method assumes that digit III remains straight throughout the power stroke and rotates around a pure hinge joint at the MTP. Both observations were qualitatively confirmed by manually articulating the joint. However, mobility at the joint permits the digit to hyperextend beyond the long axis of the tarsometatarsus. When hyperextension was detected, the facing vector was inverted to ensure that it points away from the plantar surface. Alignment of digit III with the long axis of the tarsometatarsus results in a very small facing vector, and therefore high uncertainty in its direction. Instead, any facing vector <0.000032 m was recalculated by interpolating from neighboring facings of larger magnitude. The final facings were normalized to 0.3 m. The time varying facing of the foot was defined using quaternions. In the proprietary RobotStudio program (ABB Ltd., Zurich, CH), the long-axis of the robot hand is defined as its +z-axis. In order to orient the robotic-foot as observed in the loon, the +z-axis must align with the long axis of the tarsometatarsus. We chose to align the +x-axis with the facing vector of the foot. We first calculated the quaternion to rotate the robot's +z axis to the vector from the ankle joint to the MTP (inverse of vector m above). We then calculated a second quaternion rotation, from the new +x-axis to the desired facing vector of the foot. The total rotation is the multiplication of both quaternions. All quaternions were solved using a halfway angle approach and normalized to a unit length of 1.

We calculated the trajectory of the robot required to replicate rotated foot motion with the robot at several

attachment distances from the foot. To prevent submersion of the robot, the foot attaches to the robot through a spacer. A longer spacer distances the robot from the water, but requires the robot to move a greater distance. The positioning of the robot at any time is defined by the location of the end effector (EE), the distal aspect of the hand. To calculate the placement of the EE for a given attachment length (from MTP to EE), the vector from the MTP to the ankle joint was scaled. EE trajectories were calculated for attachment distances of 0.10, 0.12, 0.13, 0.14, 0.15, 0.20, and 0.25 m.
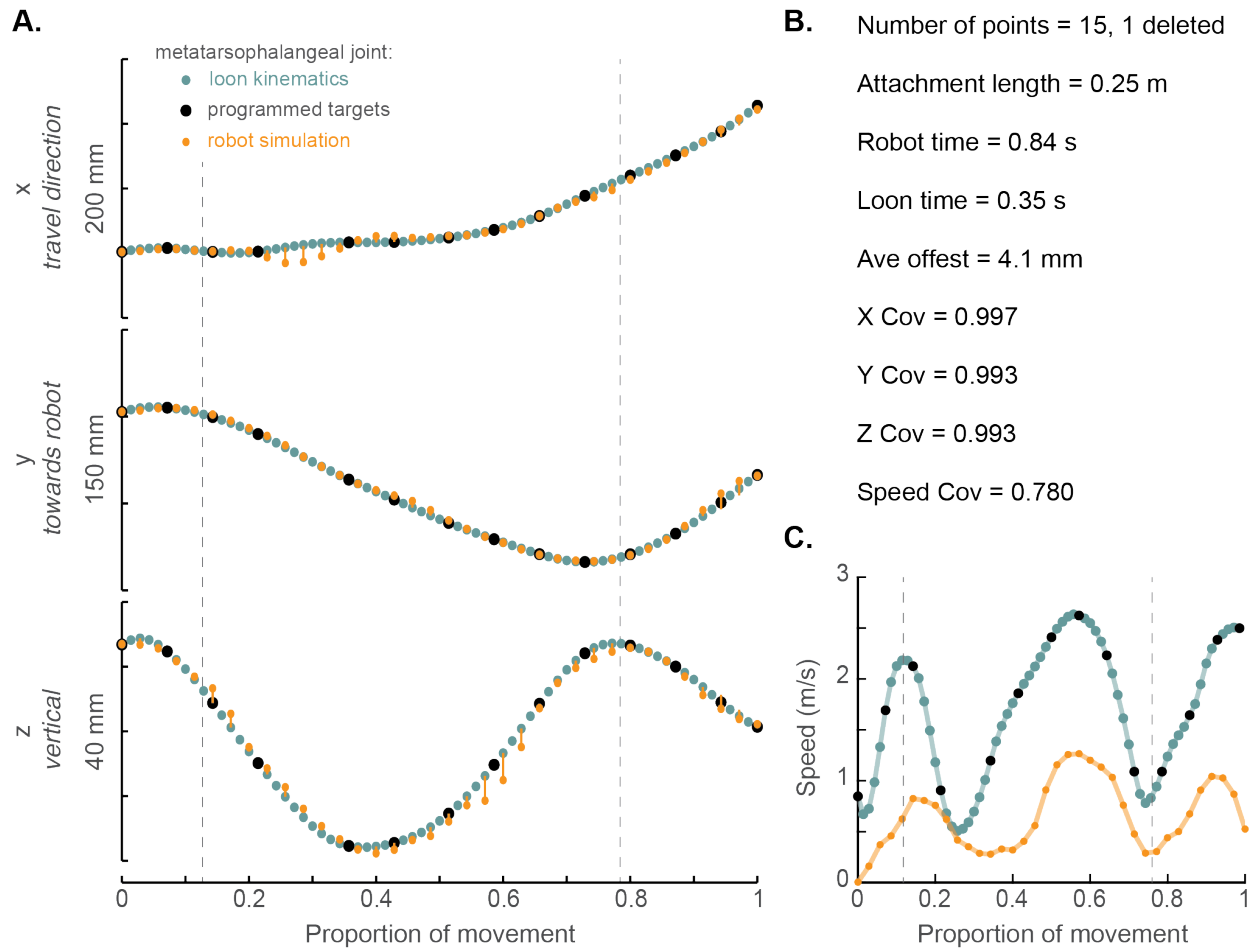
5.3.3 Robot programming in RobotStudio

ABB robots are controlled through proprietary RobotStudio software with many parameters to fine-tune robot motion. Programming the robot consists of two stages. First, positional locations, or "targets," of the end effector are defined. Then, movement commands are listed to identify a goal target and specify qualities of the motion to reach that target. There are three key components to define a target. (1) Coordinates in the 3D workspace set the desired location of the end effector. (2) The orientation, defined using quaternions, prescribes how the coordinate system of the EE should relate to the workspace coordinate system. (3) The configuration restricts the rotational range of several robot joints in order to favor one of several possible solutions for how the robot could reach a given target. Designating robot motion includes global commands and specific commands, one for each distinct movement to a target. A global command to set acceleration specifies the target value (as percent of maximum rate) as well as the rate of building to that acceleration. Each specific command consists of two main components. (1) The accuracy zone determines how close the robot needs to get to the target, ranging from 1 to 100 mm, before moving on to the next command. (2) The speed parameter defines the maximum speed of the end effector, and is either unrestricted or from 50 mm/s to 1000 mm/s at specified levels. Together, these parameters form the basis of programming robotic motion.

Specifying these parameters can occur through several workflows, varying in the level of control over robot behavior. Some methods require the program to find the best movement solutions by automatically setting val-

ues for many parameters, as is the case when defining the 3D coordinates of targets through a GUI or importing a CAD drawing for the robot to outline. Manually writing the "RAPID" code that powers the robot offers the most flexibility and customization. In this study, we programmed the robot through RAPID code to allow for detailed control and iterative tests of parameters.

The aim of our robot programming was to accurately replicate the motion of a swimming loon foot relative to still water, accounting for both position and timing. To gauge how well a robotic program reflects the experimental kinematic data, we ran repeated simulations (at least 20) within RobotStudio using the Signal Analyzer to record the end effector 3D position, orientation, and total velocity through time. Exporting this data as a .csv and importing into MATLAB, allowed us to manipulate the data and directly compare to loon swimming. Using the position and orientation values at each time point, we would extrapolate to incorporate the attachment length and find the location of the MTP (of the simulated foot). However, due to the attachment length, the robot was unable to match the speed of a swimming loon. Instead we aimed to replicate loon-swimming motions at several speeds slower than actual loon swimming. As a result, we needed to normalize the time data to a proportion of the movement. To determine if the robot accurately replicated slowed-down loon motion, we used three measures (Figure 5.4). (1) We performed cross-covariances for the x-, y-, and z- components of the extrapolated robot MTP data and the experimentally measured loon MTP data (MATLB, xcov function). (2) We determined the cross-covariance coefficient for the simulated robot MTP speed versus loon MTP speed. (3) We measured the average 3D residual of the robot MTP trajectory from the experimental MTP trajectory. Because the Signal Analyzer records data every 0.024 s (compared to experimental data at every 0.005 s), the simulated robot and experimental loon data do not align. We interpolated between neighboring experimental data values to calculate the corresponding value for every simulated data point. By combining these three measures, we can gauge how well the robot programming replicates loon swimming.

A.

metatarsophalangeal joint:
- loon kinematics
- programmed targets
- robot simulation

x *travel direction* — 200 mm

y *towards robot* — 150 mm

z *vertical* — 40 mm

Proportion of movement

B.

Number of points = 15, 1 deleted

Attachment length = 0.25 m

Robot time = 0.84 s

Loon time = 0.35 s

Ave offest = 4.1 mm

X Cov = 0.997

Y Cov = 0.993

Z Cov = 0.993

Speed Cov = 0.780

C.

Speed (m/s)

Proportion of movement

Figure 5.4: Example robot program accuracy compared to experimentally measured loon kinematics. (A) The motion of the metatarsophalangeal (MTP) joint was tracked for a freely swimming loon (turquoise) and rotated to work with the robot and aquarium. Black data points represent the targets used to program the robot. Over 20 simulations were run within RobotStudio, with the average resulting trajectory of the MTP shown in orange. (B) Several parameters were used to determine the accuracy of the robot program, including cross-covariance coefficients and average offset (or residuals). (C) Accuracy was determined not only for positional data but also for speed traces of the MTP. The program represented in this figure corresponds is Program 2, specifying robot movement at 2.4 times slower than the actual loon movement.

We manually ran simulations to systematically vary parameters to find the combination that maximized accuracy and speed. First, we determined the target positional parameters for a given attachment length, translation factor, and target number. Attachment lengths included 0.10, 0.12, 0.13, 0.14, 0.15, 0.20, and 0.25 m. The translation factors shifted the 3D coordinates of the targets within the robot reach envelope in 10 cm increments in the y and z (vertical) axes. We tested simulations using 7, 8, 10, 15, and 20 targets at equal time points throughout the movement. We also programmed the robot removing one target at a time to see if performance improves. Second, we determined the configuration sequence for each parameter combination. After manually programming the targets using the RAPID editor, the software determines potential robot configurations at each target. For 10 targets with 4-5 configurations available at each target, there are ~10 million potential configuration sequences. We first reduced the number of potential configurations by observing the simulation and identifying sequences that required extraneous robot motion. Next, we recorded simulations of the remaining configuration sequences using a standardized accuracy zone of 100 mm and no restriction on max speed. We selected the configuration sequence that resulted in the shortest duration of movement. Comparing the accuracy measures (discussed in above paragraph) of the simulation for each parameter combination (attachment length, translation factor, and target number) identified the best parameters for maximizing positional accuracy and speed.

The final robot programming used an attachment length of 0.25 m and translated the targets by 500 mm and 200 mm in the y and z directions, respectively. The fastest trial (2 times slower than the loon) used 10 targets with the 4th removed. Seven slower programs used 15 targets with the 5th removed. The robot moved linearly ("MoveL") between targets and allowed for minor alterations of the wrist position to pass a singularity ("SingArea \Wrist"). The specific global and specific movement parameters are listed in Table 5.1. The accuracy measures of each program are presented in Table 5.2.

Table 5.1: Movement parameters for each robot program. The ABB IRB 140 robot was programmed manually through the RAPID editor in the RobotStudio program. The fastest program (P1) included 10 targets with Target 4 deleted. All other programs (P2-P8) included 15 targets with Target 5 deleted. Robot movement to each target is defined by the accuracy zone in mm (Z), maximum speed in mm/s (S), and acceleration (A). Acceleration is represented as the percent of maximum values for final acceleration and ramp to that acceleration. Empty acceleration values represent 100%.

Target:		1	2	3	4	5	6	7	8	9	10	11	12	13	14	15
P1	Z	1	100	1		100	100	10	100	100	10	100				100
	S	200	max	max		max	max	max	max	max	max	max				max
	A					80,80										
P2	Z	100	200	200	200		200	200	100	100	100	100	100	100	100	100
	S	200	max	max	max		max	max	max	max	max	max	max	max	max	max
	A															
P3	Z	10	200	200	200		200	200	200	200	200	10	100	100	100	100
	S	200	max	800	800		max	max	800	1000	800	600	max	600	800	1000
	A															
P4	Z	10	200	200	200		200	200	200	200	200	10	100	100	100	100
	S	200	max	600	600		max	max	800	1000	800	600	max	600	800	800
	A				60,60		60,60	60,60	60,60	50,50	60,60	60,60	60,60	60,60	60,60	
P5	Z	10	200	200	200		200	200	200	200	200	10	100	100	100	100
	S	200	max	600	600		max	max	800	1000	800	600	max	600	800	800
	A				50,50		50,50	50,50	50,50	50,50	50,50	50,50	50,50	50,50	50,50	
P6	Z	10	200	200	200		200	200	200	200	200	10	100	100	100	100
	S	200	600	600	400		400	500	800	1000	600	400	300	400	800	800
	A			50,50	50,50		50,50	50,50	50,50	50,50					50,50	
P7	Z	10	200	200	200		200	200	200	200	200	10	100	100	100	100
	S	200	500	600	400		400	500	800	1000	600	400	300	400	800	800
	A		50,50	50,50	50,50		50,50	50,50	50,50	50,50					100,50	
P8	Z	10	200	200	200		200	200	200	200	200	10	100	100	100	100
	S	200	400	500	400		300	400	500	600	500	300	300	400	500	600
	A		50,50													

Table 5.2: Accuracy measures for robot programs. How accurately the robot replicated normal loon movement was determined using five measures, including the average offset (or residual) at each time point and cross-covariances of the resulting MTP position in each axis and the total speed.

Program Number	Robot Time (s)	Times slower than loon	Ave offset (mm)	x Cov	y Cov	z Cov	Speed Cov
P1	0.72	2.06	7.5	0.98	0.99	0.97	0.86
P2	0.84	2.40	4.1	1.00	0.99	0.99	0.78
P3	0.94	2.67	3.9	1.00	0.99	1.00	0.93
P4	1.056	3.04	5.0	1.00	0.99	0.99	0.90
P5	1.128	3.22	6.0	0.99	0.99	0.98	0.84
P6	1.176	3.34	5.0	1.00	0.99	1.00	0.91
P7	1.224	3.50	3.7	1.00	0.99	0.99	0.84
P8	1.368	3.87	4.6	0.99	0.99	1.00	0.92

5.3.4 Robotic set-up

To record the forces produced by a swimming loon foot, left feet were removed from carcasses and attached to the end effector through a force sensor then manipulated in an aquarium. We built a custom aquarium out of acrylic (1/4" thickness) with dimensions of 20x 16x12 inches. Seven common loon carcasses were obtained from the Tufts Wildlife Clinic (North Grafton, MA, USA) under federal (MB005348-1) and state (Massachusetts 050.13SAL) scientific collecting permits. Carcasses ranged in body mass from 3.0-5.2 kg. The left foot of each bird cut just distally to the head of the tarsometatarsus. A 0.75" 10-32 stainless-steel threaded rod was partially inserted into the medullary cavity of the tarsometatarsus, aligned with the long axis of the bone, and secured using cyanoacrylate glue. The feet were attached to the force sensor through a stainless steel threaded standoff allowing for fine-tuned manipulation of the attachment length to ensure a distance of 0.25 m from the end effector.

Two tri-axial force sensors measured the time-varying force experienced by each loon foot. One sensor (nano43, ATI Industrial Automation, North Carolina, USA) measures small forces at high resolution, but faster trials often produced forces outside its accuracy range. A second sensor (mini45, ATI Industrial Automation, North Carolina, USA) accurately measures up to 290 N or 10 Nm, but does so at a reduced resolution. Forces were recorded using an adapted script in the LabView Max software at 1,000 Hz (National Instruments Co., Texas, USA). The force sensors were attached to the robot using a tool changer (QC-11, ATI Industrial Automation, North Carolina, USA). Custom attachment plates were designed and 3D printed to attach the sensor to the tool changer and to the threaded standoff attached to the foot.

5.3.5 Robot recordings

Recording the direction of gravity relative to the foot in two positions relates the forces recorded by the sensor to the anatomical axes of the foot. Loon feet were attached to align with the robot (as described above), however the force sensor was attached at a rotational offset so that the cable would not be submerged. In order to relate the X- and Y- axes of the force sensor to those of the foot, the robot was actuated to place the foot horizontally

facing downward (testing the +A-axis of the foot) and towards the robot (testing the -B-axis of the foot). The sensor was zeroed in each position with the X-, Y-, and Z- force measured when hanging a weight from around the standoff.

The influence of inertia, buoyancy, and gravity were measured to subtract these forces from swimming force recordings. Inertia, the force experienced from moving any object with mass, confounds our force measurements. To account for inertia, forces were recorded for the foot moving through air at all programmed speeds (zeroing the sensor at a home target out of the water). Any object underwater experiences both downward gravitational acceleration and upward buoyancy, which vary based on the submerged volume and the depth. These static forces were measured by filling the aquarium with water and recording the force exerted against the foot placed at each programmed target. Force values measure the change in force relative to zeroing at the home target. The inertia, gravity, and buoyancy values were recorded for each foot.

Total force experienced by the left foot of a swimming loon during the power stroke was recorded for 8 movement speeds and seven loon feet. As above, force was zeroed as the home position then moved to the first target. After waiting for 3 seconds to reduce any influence of waves, the robot actuated the swimming motion. The robot waited for 5 seconds at the last target before returning to home. 15 repetitions were recorded for each movement speed using each foot (a total of 840 trials).

The RobotStudio program does not report the trajectory of the robot during actuation. In order to confirm that the movement of the foot accurately replicates the programmed motion, we recorded a representative trial at 120 fps of each foot at the fastest speed using two GoPro Hero 3+ cameras (Black Edition, GoPro, California). Before each recording a submersible LED wand was filmed (60 fps) moving within the tank throughout the shared field-of-view of the cameras.

5.3.6 Force data analysis

The force trace from each trial records the robot during several phases: zeroed at the home target, moving to target 1, held at target 1, actuated through remaining targets, and held at the last target (Figure 5.5A). The beginning of the actuated motion was determined by comparing the force trace to the measured gravity/buoyancy forces at target 1. The force X-component had the largest gravity/buoyancy component at target 1 so was used for identifying the start of motion. We identified when the x-force trace diverged more than 0.25 N from the target 1 gravity/buoyancy force after remaining within that cutoff for at least 350 frames (Figure 5.5B).

A. Raw force vs. time
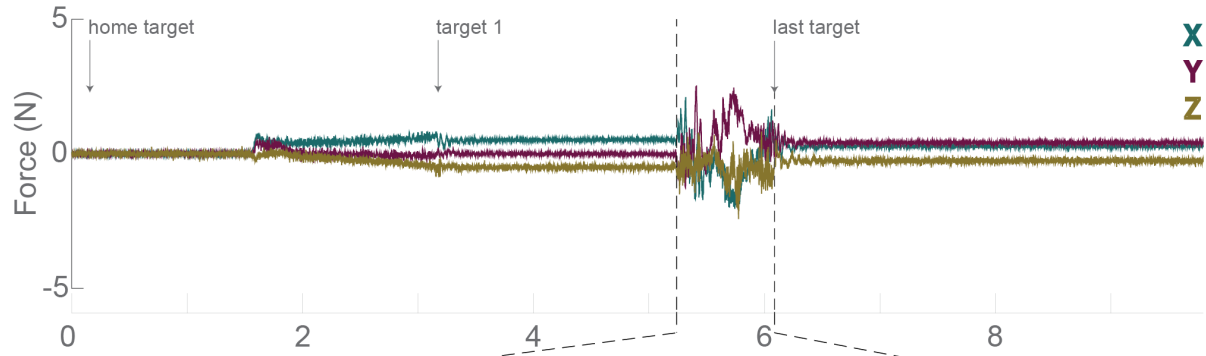
B. Lowpass butterworth filter and zeroed
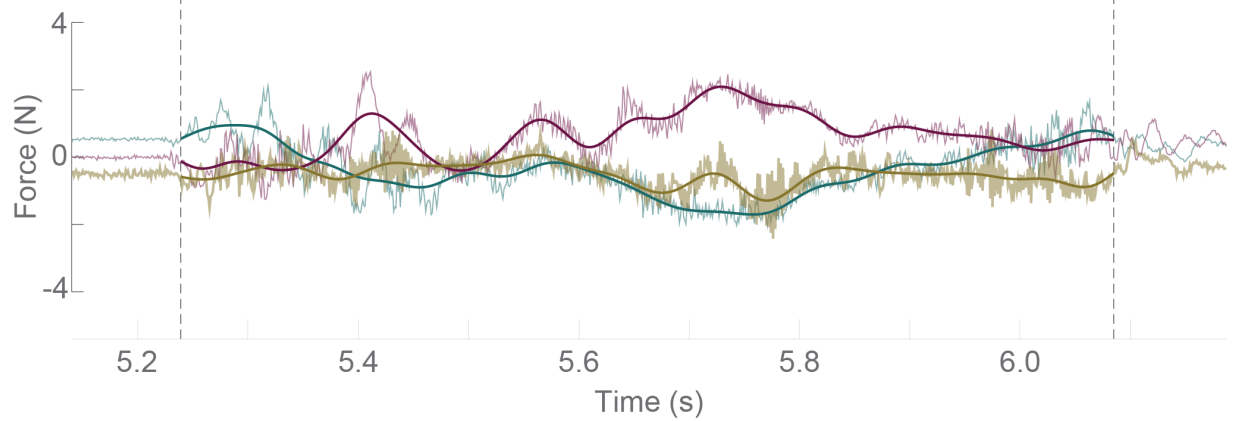
Figure 5.5: Raw force recording with identified start and end of motion and low-pass filtering. (A) Each force recording trace (ATI mini45) represents many stages of programmed robot motion. Force was zeroed with the robot at the home target and recorded as the robot traveled to the first target, paused at the first target, actuated the programmed foot motion, and paused at the last target. (B) The beginning and end of actuated movement were determined by comparing the force recording trace to the gravity/buoyancy forces measured at the first and last targets. The movement force traced was filtered to reduce noise (low-pass Butterworth, order=4, cutoff frequency = 13 Hz).

After trimming the force traces at the start of motion, all force components were filtered and zeroed to remove noise. Butterworth filters were applied to all force traces reflected around the start of motion (order = 4, frequency cutoff = 13). Filter parameters were selected by visually comparing incremental adjustments in order number and cutoff frequency with respect to the filtered profile and spectral density. Although the force sensors were zeroed at the home target, noise in the signal produced minor offsets. To account for these offsets, the average force values at the home target (using the first 0.4 s of each recording) were found and subtracted from the rest of the trial.

The end of the actuated motion was determined by comparing the force Y-component to the gravity/buoyancy measured at the last target. The exact end of motion was identified as the first crossing of the gravity/buoyancy value of the last target before beginning a sinusoidal pattern around that value. The traces from each of the 15 trials were aligned to the first peak in the Y-force and averaged (Figure 5.6A).

Inertia, gravity, and buoyancy were subtracted from the filtered force data. We measured inertial forces by actuating the robot in air. We identified the start and end of motion as described above. To isolate inertia from the influence of gravity, we recorded the force acting with the robot positioned statically in air at each target (relative to zeroing at the home target). We fit a cubic spline to interpolate between these values for each time point and subtracted the gravity recordings from the inertia recordings. We then scaled the inertia-minus-gravity traces by aligning the peak Y-forces with those from the underwater recording and subtracted the inertia-minus-gravity from the underwater force recording (Figure 5.6B). We performed a similar method to subtract the influence of gravity/buoyancy while underwater. We fit a spine to the gravity/buoyancy forces measured with the robot positioned underwater at each target (Figure 5.6C). We then subtracted this trace from the underwater force minus inertia values.
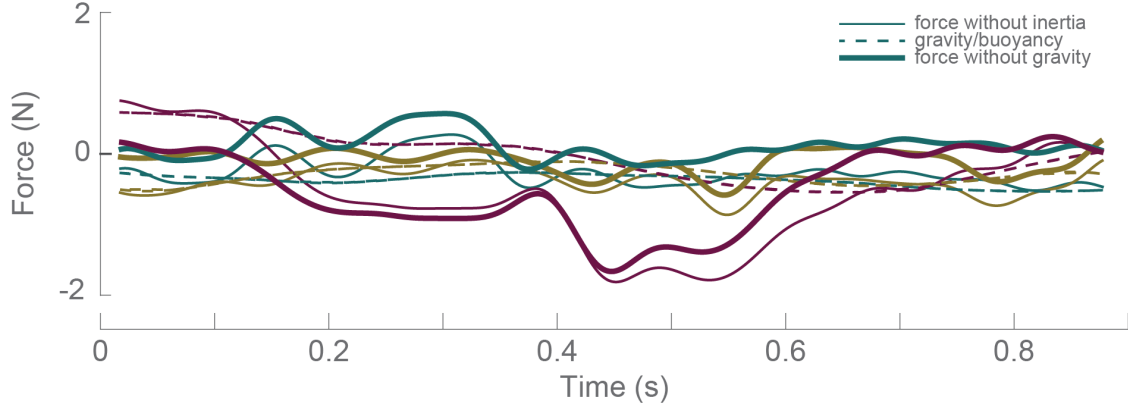
**A. Aligned and averaged trials**
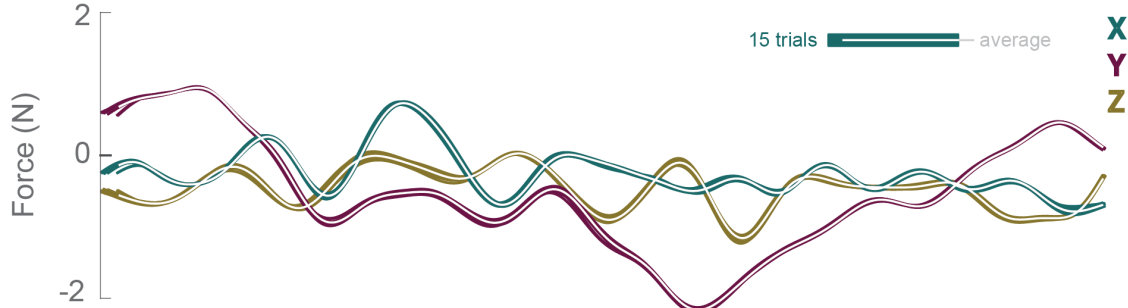
**B. Inertia subtraction**
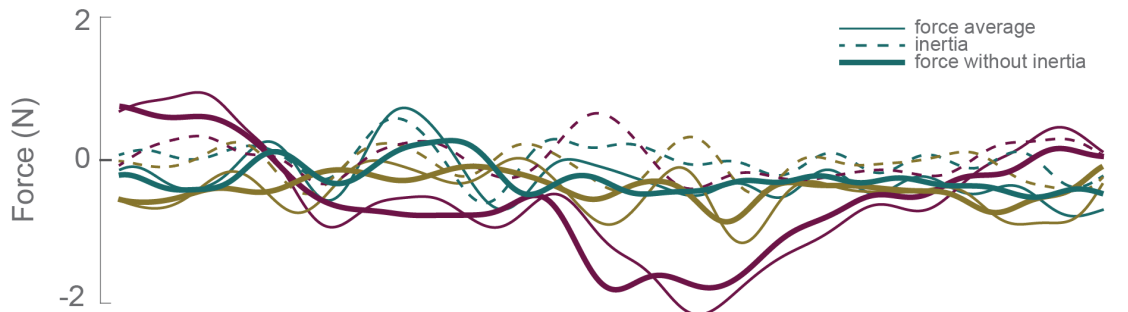
C. Gravity and buoyancy subtracted

Figure 5.6: Force recording analysis for each robot program. (A) The filtered force traces for 15 trials at each speed were aligned and averaged. (B) Inertia was measured while actuating each foot in air and subtracting the influence of gravity. This inertia trace (dashed line) was subtracted from the average force recording for each underwater program (thin lines), resulting in the recording of forces experienced throughout the movement without inertia (thick lines). (C) The influence of gravity and buoyancy throughout the underwater trials was measured by recording the force with the robot held at each target and interpolated using a cubic spine (dashed lines). This trace was subtracted from the force without inertia (thin lines) to isolate only hydrodynamic forces (thick lines).
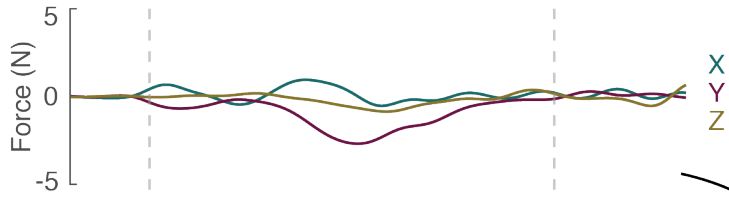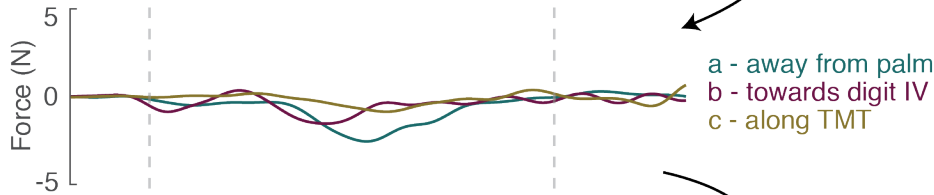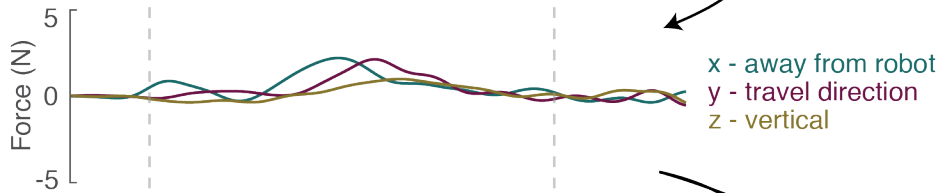
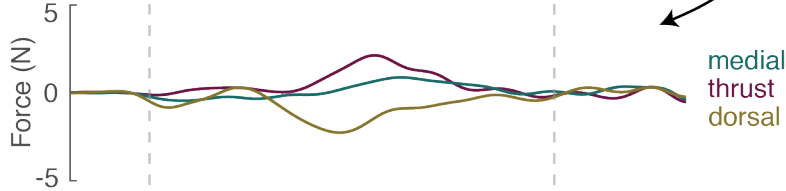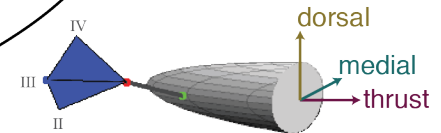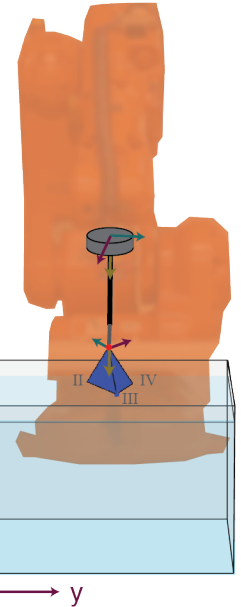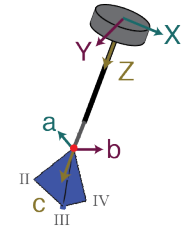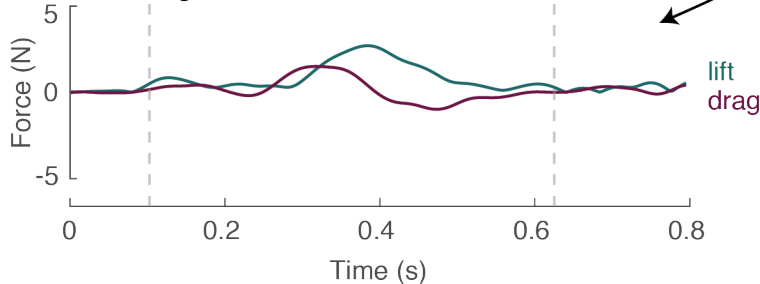**Figure 5.7:** Rotation of force sensor recordings to other axes for the fastest speed program of one loon (body mass = 3.3kg). (A) Filtered, subtracted, and averaged force recordings from the ATI tri-axial sensor. Each line represents the average from 15 trials. (B) Force sensor recordings have been rotated based on a separate recording in order to align with anatomical axes of the foot: away from the palmar surface of the foot, towards digit IV, and along the long axis of the tarsometatarsus (TMT). (C) Forces relative to the foot rotated based on time varying orientation of the foot in order to represent forces relative to the axes of the workspace: away from the robot, to the right when looking at the robot coinciding with the travel direction of the loon, and vertical. (D) Forces relative to the workspace rotated by -98 degrees to represent force relative to the anatomical axes of the loon: directed medially towards the midline, along the travel direction as thrust, and from ventral to dorsal that aligns with vertical for a loon swimming horizontally. (E) Forces relative to the workspace compared to time varying motion of the foot relative to the workspace, in order to find drag and lift components. The metatarsophalangeal joint (MTP) defined foot motion. Drag opposed MTP motion. Lift is all force acting in the plane perpendicular to MTP motion. (Right) Diagrams show axes definitions. Even though experiments were performed on left feet, the bottom diagram (medial, thrust, dorsal) shows axes relative to a right foot for consistency with Figure 1.

At this point in the analysis, the force values represent the hydrodynamic forces experienced by the loon foot in relation to the axes of the force sensor (X, Y, and Z). To relate these forces to lift and drag or the anatomical axes of the loon, we first calculated the force relative to the foot (A, B, C) then rotated these forces to be relative to the workspace (x, y, z) and the loon (T, L, and D) (Figure 5.7). Measurement of XYZ forces when applying a force along the A- and B-axes (see "Robot recordings" section above) define the rotation between the XY and ab axes. The +A-axis was defined as extending away from the palmar side of the foot. The +B axis points towards digit IV and +C points distally along the long-axis of the tarsometatarsus.

We next rotated the ABC-forces to represent the force experienced in the xyz-axes of the workspace. First, we imported the quaternions experienced by the robot hand from the simulation of the relevant trial. Because the quaternion values were represented as piece-wise functions, we could not directly interpolate the simulation data to correspond to the recorded robot trial data. Instead, we used the simulation quaternions to calculate the A- and C-axis vectors in terms of the workspace xyz-axes throughout the trial, then used these vectors to calculate the robot's quaternions at each time point. These quaternions were then applied as inverse quaternions to the robotic force recording data. The inverse quaternion was applied to the ABC force vectors to find the xyz force vectors, representing the force recorded by the sensor throughout time relative to the workspace axes.

In order to allow the robot to actuate the loon foot motion from above, the foot motion was rotated around the travel direction. While the workspace y-axis corresponds to the loon swimming direction (thrust, T), the other forces (x- and z-) do not correspond to the mediolateral and dorsoventral axes of the loon. We originally rotated the foot motion by 98 degrees counterclockwise around the y-axis. To reverse this motion, we rotated the x- and z-force vectors by 98 degrees clockwise, solving for the lateral-to-medial force on the left side, M, and ventral-to-dorsal (D) force.

Lastly, we determined the component of the total force measured that was in line with the direction of foot motion. We imported the simulated motion of the MTP (relative to the workspace, xyz-, coordinate system) and found the unit speed vector at every simulated time point. We interpolated between these vectors by applying

a spline, resulting in the unit speed vector for every force recording data point. We took the dot product of the recorded xyz-forces with the unit speed of the MTP and multiplied by -1 to find the drag force (that in the opposite direction of MTP motion). We subtracted drag from the total force recorded to determine the magnitude of lift force (any force in the plane perpendicular to MTP motion).
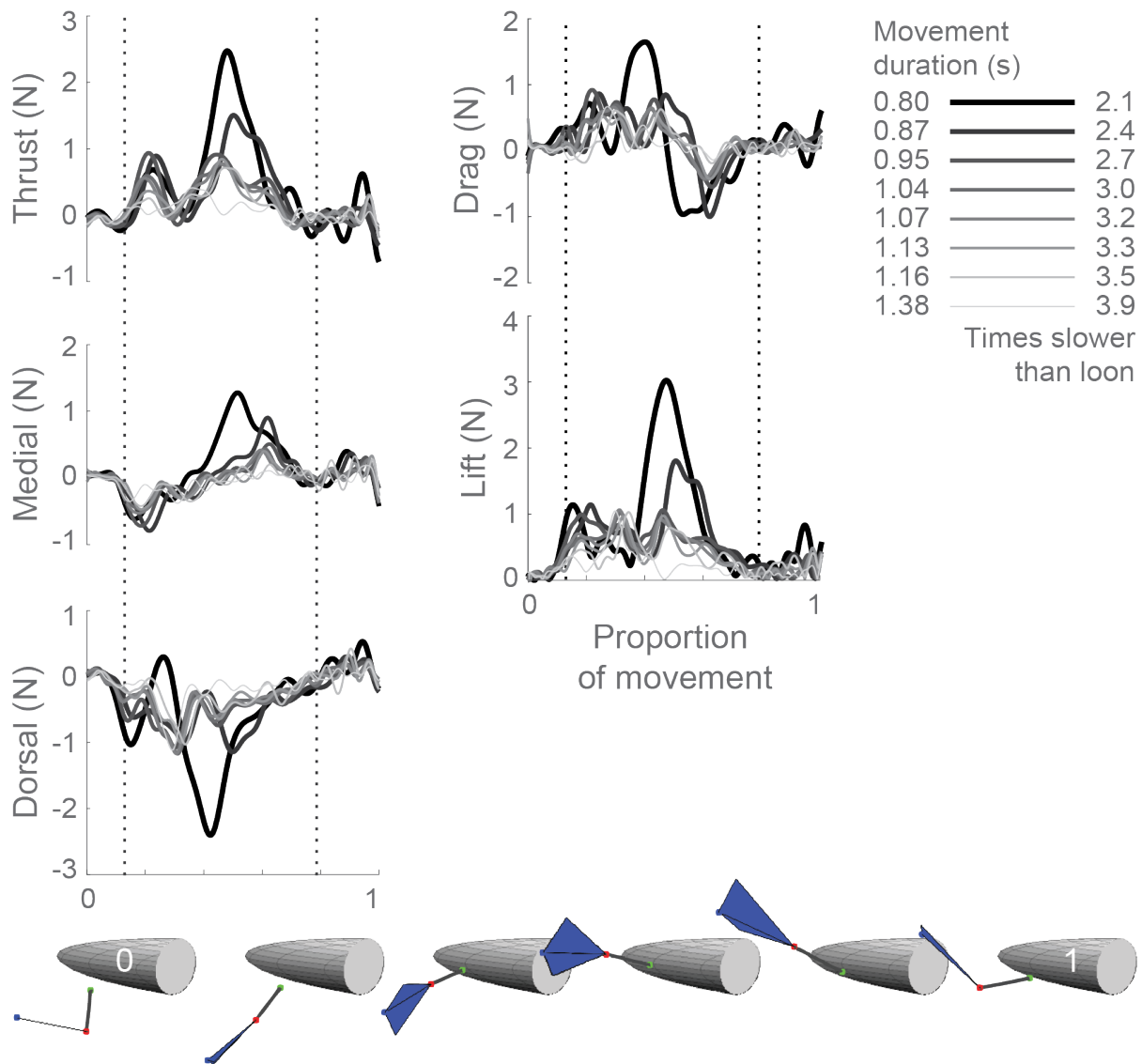
This process was repeated all 8 programs, representing various paddling speeds, and for each of seven feet (Figure 5.8).

5.3.7   Loon foot area analysis

The surface area of one or two feet from each loon carcass was calculated using ImageJ (Schneider et al., 2012). Each foot was manually extended with the toes adducted and pinned to a white background. A picture was taken perpendicular to the foot including a scale bar. The image was scaled, an outline of the foot was automatically generated using a threshold, and the area of the foot up to the metatarsophalangeal joint was calculated.

A. Force relative to body

B. Force relative to foot motion

Movement
duration (s)

0.80	2.1
0.87	2.4
0.95	2.7
1.04	3.0
1.07	3.2
1.13	3.3
1.16	3.5
1.38	3.9

Times slower
than loon

Proportion
of movement

Figure 5.8: Swimming forces exerted on a swimming loon foot at various speeds. A 6 degree of freedom force sensor recorded force as the loon foot was actuated in a swimming motion. These forces were decomposed relative to the body (A) and relative to foot motion (B). Swimming forces relative to the loon body show (top) thrust in line with the body swimming direction, (middle) medially directed forces towards the body midline, and (bottom) dorsally directed forces opposing gravity. Swimming forces relative to the motion of the foot depict (top) drag, or the force that acts opposite to foot motion, and (bottom) lift, all remaining force that acts in the plane perpendicular to foot motion. All speeds were normalized to the duration of movement on the x-axis. The swimming schematic shows the foot position during the actuated movement. Vertical dashed lines demark the beginning and end of the power stroke. Each line represents an average over 15 trials for the same foot (that of the loon weighing 3.3 kg), with line thickness corresponding to movement duration. Relatively large forces at the end of the actuated movement likely result from foot deceleration not present in normal swimming.

5.4   REFERENCES

Alexander, R. M. (2003). Principles of animal locomotion. Princeton University Press.

Baudinette, R. V. and Gill, P. (1985). The energetics of "flying" and "paddling" in water: locomotion in penguins and ducks. J. Comp. Physiol. B 155, 373-380.

Corr, D. T. and Hart, D. A. (2013). Biomechanics of Scar Tissue and Uninjured Skin. Adv. Wound Care 2, 37-43.

Diridollou, S., Vabre, V., Berson, M., Vaillant, L., Black, D., Lagarde, J. M., Gregoire, J. M., Gall, Y. and Patat, F. (2001). Skin ageing: changes of physical properties of human skin in vivo. Int. J. Cosmet. Sci. 23, 353-362.

Dudek, G., Giguere, P., Prahacs, C., Saunderson, S., Sattar, J., Torres-Mendez, L., Jenkin, M., German, A., Hogue, A., Ripsman, A., et al. (2007). AQUA: An Amphibious Autonomous Robot. Computer (Long. Beach. Calif). 40, 46-53.

Gursul, I. (2004). Recent developments in delta wing aerodynamics. Aeronaut. J. 108, 437-452.

Johansson, L. C. and Norberg, U. M. (2000). Asymmetric toes aid underwater swimming. Nature 407, 582-3.

Johansson, L. and Norberg, U. M. (2001). Lift-based paddling in diving grebe. J. Exp. Biol. 204, 1687-96.

Johansson, L. and Norberg, R. (2003). Delta-wing function of webbed feet gives hydrodynamic lift for swimming propulsion in birds. Nature 424, 65-68.

Kato, N. (2011). Swimming and Walking of an Amphibious Robot With Fin Actuators. Mar. Technol. Soc. J. 45, 181-197.

Lovvorn, J. and Jones, D. (1994). Biomechanical conflicts between adaptations for diving and aerial flight in estu-

arine birds. Estuaries and Coasts 17, 62-75.

Nam, G. W., Baek, J. H., Koh, J. S. and Hwang, J.-K. (2015). The seasonal variation in skin hydration, sebum, scaliness, brightness and elasticity in Korean females. Ski. Res. Technol. 21, 1-8.

Nocera, J. J. and Burgess, N. M. (2002). Diving schedules of Common Loons in varying environments. Can. J. Zool. 80, 1643-1648.

Quintana, F., Wilson, R. P. and Yorio, P. (2007). Dive depth and plumage air in wettable birds?: the extraordinary case of the imperial cormorant. Mar. Ecol. Prog. Ser. 334, 299-310.

Ribak, G., Weihs, D. and Arad, Z. (2004). How do cormorants counter buoyancy during submerged swimming? J. Exp. Biol. 207, 2101-2114.

Schneider, C. A., Rasband, W. S. and Eliceiri, K. W. (2012). NIH Image to ImageJ: 25 years of image analysis. Nat. Methods 9, 671-675.

Schorger, A. (1947). The Deep Diving of the Loon and Old-Squaw and Its Mechanism. Wilson Bull. 59, 151-159.

Stolpe, M. (1935). Colymbus, Hesperornis, Podiceps: ein Vergleich ihrer hinteren Extremität. J. fur Ornithol. 83, 115-128.

Vogel, S. (2008). Modes and scaling in aquatic locomotion. Integr. Comp. Biol. 48, 702-12.

Walker, J. a and Westneat, M. W. (2000). Mechanical performance of aquatic rowing and flying. Proc. Biol. Sci. 267, 1875-81.

Watanabe, Y. Y., Sato, K., Watanuki, Y., Takahashi, A., Mitani, Y., Amano, M., Aoki, K., Narazaki, T., Iwata, T., Minamikawa, S., et al. (2011). Scaling of swim speed in breath-hold divers. J. Anim. Ecol. 80, 57-68.

Westerweel, J., Elsinga, G. E. and Adrian, R. J. (2013). Particle Image Velocimetry for Complex and Turbulent

Flows. Annu. Rev. Fluid Mech. 45, 409-436.

Wilcox, H. H. (1952). The Pelvic Musculature of the loon, gavia immer. Am. Midl. Nat. 48, 513-573.

6

Discussion

6.1 Summary of major findings

Birds that swim using their feet face a distinct challenge to move through an aquatic world with a body ancestrally specialized for flight and limbs originally adapted for walking. But, foot-propelled swimming in birds has evolved independently numerous times and to varying degrees of specialization. This specialization comes at a cost. Some birds have evolved to dive dozens of meters underwater to capture fish or aquatic prey. These divers spend most of their life swimming and struggle to stand on land, demonstrating a functional tradeoff for the limbs between walking and swimming. The goals of this thesis were to understand the anatomical, behavioral, and mechanistic

patterns of specialization in foot-propelled swimming birds. Specifically, this work aimed to:

1. examine how hindlimb muscle anatomy varies with swimming specialization across phylogenetically independent groups of foot-propelled swimming birds;

2. investigate movement kinematics used by foot-propelled swimming birds during normal behaviors in natural settings: Western grebes running on water ("rushing") during a breeding display and common loons swimming freely in a large rehabilitation pool; and

3. directly measure fluid forces generated by the feet during loon swimming.

The work presented here identifies patterns in muscle anatomy conserved across independent lineages of foot-propelled swimming bird. But, grebes and loons demonstrate some variation, which is surprising given their similar lifestyles. In grebes, most of the distal ankle plantarflexor tendons are calcified, a feature found in many group of birds but lost in almost all swimmers. Loons possess especially massive gastrocnemius and digital flexor muscles, comprising most of the leg. These findings provide a new basis for understanding how musculoskeletal anatomy relates to swimming, motivating further comparative work both within birds and among other swimming animals.

High-speed recordings of rushing grebes in the wild reveal a new mechanism for running on water. Unlike basilisk lizards, grebes do not retract their feet through an air bubble. Instead, grebes take up to 20 steps per second, the highest known step frequency in birds to date. Laboratory studies on physical models of feet show that grebes support a large portion of their weight just by slapping the water surface, with impact forces reaching up to 50 N. These rushing forces approach values for terrestrial running in birds of a similar size, which also have calcified digital flexor tendons. Therefore, the extreme physical demands of rushing may partially explain discrepancies in grebe and loon hindlimb muscle anatomy.

We find that swimming in common loons qualitatively resembles grebe swimming with a lateral position of the feet and including long-axis rotation of each foot (Johansson and Norberg, 2001). This is surprising given that the webbed feet of loons do not resemble lobate grebe feet, and since the way that grebes paddle their feet is associated with using the lobate toes as individual hydrofoils to generate lift (Johansson and Norberg, 2000).

In contrast, even though the feet of loons resemble those of cormorants, cormorants swim by paddling the legs underneath the body (Ribak et al., 2004). Swimming kinematics in specialized diving birds is not associated with foot shape, but instead may relate to the extent of terrestrially.

Large ankle plantarflexors in loons may correspond with a need to overpower strong body drag forces using a limited stride frequency. The relatively large body size of loons compared to grebes produces higher resistive body drag (Lovvorn et al., 2001), suggesting that loons must produce stronger propulsive swimming forces than grebes to swim at similar speeds. Higher average swimming forces can either be accomplished by paddling the feet more often or by producing more force during each stride. Based on the shortest power and recovery strokes observed in loons swimming in a straight trajectory (0.21 and 0.15 s respectively), loons can paddle at a maximum stride frequency of 2.8 Hz. Grebes use a similar stride frequency, 2.5 Hz (Johansson and Norberg, 2001), suggesting that loons must produce stronger forces with each power stroke. Producing stronger swimming forces during a power stroke requires stronger, and therefore larger, ankle plantarflexors. A loon's need to produce more force during each paddling cycle may help explain the comparatively large distal limb muscles observed in loons versus grebes.

Previous work, including that in this thesis, has identified anatomical features and movement strategies associated with specialization for swimming in foot-propelled birds. However, the functional importance of these traits cannot be understood without a direct association to swimming performance. Here, we design a new method to directly measure swimming forces generated by a paddling foot. We find that loons produce more lift than drag to power swimming, contradicting previous categorizations of foot-propelled birds as drag-based. These results challenge historical perceptions of aquatic locomotion, which associate foot-propelled swimmers with less efficient drag forces. Instead, foot-propelled swimmers may use novel lift-producing mechanisms and serve as important inspiration for aquatic designs. Furthermore, our robotic method provides a new, accurate system to test how variation in foot anatomy or paddling motion influences swimming force production.

The research presented in this thesis helps clarify the extent of convergence among foot-propelled swimming birds. Specialized diving birds generally demonstrate similar patterns in muscle anatomy with grebes and loons

possessing a few distinguishing features associated with rushing or swimming behavior. The swimming motions of grebes and loons exhibit convergence, but differ from those of cormorants, potentially relating to the retained ability of cormorants to stand and walk on land. Diving loons, like grebes, demonstrate head-bobbing even through cormorants do not. Therefore, the story of convergence within foot-propelled swimming birds is not simple. Specialized diving birds have not evolved a single, conserved strategy for swimming and hunting underwater. Instead behavioral and anatomical variations among these groups have shaped the evolution of several mechanisms for generating fluid forces using the feet. These findings motivate future studies on other foot-based swimming animals, including frogs, turtles, and the platypus. Moreover, this thesis establishes foot-propelled swimmers as an important group for understanding efficient underwater force production and inspiring robotic or underwater designs.

6.2 Individual chapter summaries

6.2.1 Chapter 1

Although previous studies have identified shared avian skeletal features within foot-propelled swimming, patterns in muscle anatomy have never before been analyzed. Through detailed dissection of 35 specimens representing eight species, we find some consistent myological patterns associated with swimming specialization. Specialized diving birds position the femur and proximal tibiotarsus under the skin covering the abdomen to streamline the body. This integration of the proximal limb facilitates dramatic shifts in muscle attachment. In specialized diving birds, the *flexor cruris lateralis* (FCL) and i*liofibularis* (IF) reduce in size and the insertions shift distally along the tibiotarsus. The *femorotibialis medius* (FTM) extends along an expanded cnemial crest and/or patella. The resulting increased moment arms of these muscles likely help stabilize the knee and hip while paddling, reducing drag acting on the body that resists forward motion. All diving birds possess exceptionally large distal ankle plantarflexors, including the gastrocnemius and digital flexors. With the hip and knee stabilized, these muscles almost wholly power foot propulsion. However, we identify a few differences between grebes and loons. The

gastrocnemius lateralis and digital flexors in loons are especially large, whereas grebes possess calcified digital flexor tendons.

6.2.2 CHAPTER 2

In addition to using the hindlimbs for swimming, two species of grebes pursue potential mates by running on water without any assistance from wing flapping, called rushing. These grebes are the largest animals capable of running on water, weighing 10 times more than the next largest water runners, basilisk lizards. To analyze how grebes generate the forces necessary to overcome gravity and sustain rushing, we (1) filmed wild grebes rushing on a lake in Southern Oregon and (2) measured how the slap of the water surface contributes to weight support by replicating water slap in the laboratory using physical models. Grebes rush by slapping the water surface then retracting the foot in a lateral arc. This represents a qualitatively different strategy than basilisk lizards, which retract each foot forwards through a bubble formed behind the foot. We also find that rushing grebes take up to 20 steps per second, a higher stride rate (10 Hz) than any previous observation in birds. The high impact speed of each water slap generates up to 30-55% of the required weight support, corresponding to an average force of 50 N.

6.2.3 CHAPTER 3

Although loons are arguably one of the most successful groups of swimming birds, their strong preference for expansive bodies of water has prevented quantitative analysis of swimming to date. To compare the swimming kinematics of loons to other convergent groups of specialized swimming birds, we filmed four common loons swimming freely in a pool at a rehabilitation clinic. Loons swim by synchronously paddling their feet lateral to the body, combining flexion-extension of the ankle with long-axis rotation at the knee. Loons use head-bobbing to enhance underwater vision and execute tight but slow turns compared to other aquatic swimmers. To control turning, loons increase the speed of the outside foot, begin the power stroke of the outside foot before that of the inside foot, and bank the body away from the turn.

6.2.4 CHAPTER 4

Cormorants, grebes, and now loons demonstrate swimming strategies that involve paddling the feet backwards relative to the body but not relative to still water. These movements suggest that foot-propelled diving birds may generate lift forces, but foot-based swimmers are often considered drag-based (Vogel, 2008). Experimental and technological challenges have previously prevented measurement of swimming forces in foot-propelled birds. By developing a new method, we experimentally measure swimming forces of a paddling foot for the first time. We attached cadaveric loon feet to an industrial robot programmed to replicate swimming motion and measure resulting forces. We confirm that loons power swimming through more lift than drag. This finding overturns a historical perception of animal swimming and motivates further investigation of the mechanisms that previously-overlooked foot-propelled swimmers use to efficiently produce fluid forces.

6.3 REFERENCES

Johansson, L. C. and Norberg, U. M. (2000). Asymmetric toes aid underwater swimming. Nature 407, 582-3.

Johansson, L. and Norberg, U. M. (2001). Lift-based paddling in diving grebe. J. Exp. Biol. 204, 1687-96.

Lovvorn, J., Liggins, G. a, Borstad, M. H., Calisal, S. M. and Mikkelsen, J. (2001). Hydrodynamic drag of diving birds: effects of body size, body shape and feathers at steady speeds. J. Exp. Biol. 204, 1547-57.

Ribak, G., Weihs, D. and Arad, Z. (2004). How do cormorants counter buoyancy during submerged swimming? J. Exp. Biol. 207, 2101-2114.

Vogel, S. (2008). Modes and scaling in aquatic locomotion. Integr. Comp. Biol. 48, 702-12.